AD-A063 305 GENERAL DYNAMICS SAN DIEGO CALIF ELECTRONICS DIV F/G 20/14
WAVE PROPAGATION THROUGH HOLLOW DIELECTRIC SHELLS.(U)
NOV 78 G TRICOLES, E L ROPE, R A HAYWARD N00019-77-C-0303
NL

UNCLASSIFIED

1 OF 1
AD
AD83305

END
DATE FILMED
3--79
DDC

LEVEL II

R-77-002-5
November 1978

WAVE PROPAGATION THROUGH HOLLOW DIELECTRIC SHELLS

FINAL REPORT

G. Tricoles, E. L. Rope, R. A. Hayward

Prepared for
U.S. Naval Air Systems Command
under
Contract N00019-77-C-0303

GENERAL DYNAMICS
Electronics Division

(7) (14) R-77-092-5
November 1978

(6) WAVE PROPAGATION THROUGH HOLLOW DIELECTRIC SHELLS.

(9) FINAL REPORT

(10) G. Tricoles, E. L. Rope R. A. Hayward

(11) Nov 78

(12) 88 p.

Prepared for
U.S. Naval Air Systems Command
under
Contract (15) N00019-77-C-0303

GENERAL DYNAMICS
Electronics Division
P.O. Box 81127, San Diego, California 92138 · 714-279-7301

147 750

CONTENTS

CONTENTS (Continued)

ILLUSTRATIONS

ILLUSTRATIONS (Continued)

ILLUSTRATIONS (Continued)

ILLUSTRATIONS (Continued)

TABLES

1. INTRODUCTION AND SUMMARY

1.1 INTRODUCTION

Radomes affect the performance of airborne radar and guidance systems by reducing guidance accuracy and radar range. These system effects limit existing missiles, and they restrict the development of newer missiles that have increased speeds, higher altitudes, greater frequency bandwidths, or smaller dimensions. The need for improved accuracy requires accurate methods for radome analysis. Although adequate methods exist for designing radomes that enclose antennas with diameters greater than several wavelengths, these methods fail for smaller antennas and radomes. The development of small or broadband radomes is largely empirical so that data are available only after a radome is fabricated and tested. This approach is tedious and expensive, and it delays the synthesis of systems. A more general, analytical design method is desirable.

The development of a general design method requires a model that relates radome composition and configuration to system effects. The link is the physical effects of a radome; namely, boresight error, attenuation, and sidelobe level increases. These three effects can be qualitatively and quantitatively derived from farfield patterns of the antenna in the radome.* Consider sum mode patterns with and without radome as in Figure 1-1. Attenuation or loss is the reduction in intensity at the peak of the main beam, and boresight error is the angular shift of the beam peak. For monopulse or conical scan antennas, boresight error is the angular shift of the tracking minimum instead of the peak. Sidelobe levels changes are the changes in the intensity of subsidiary maxima in the antenna pattern.

Antenna patterns are computed by evaluating diffraction integrals. We assume receiving operation in order to consider plane waves incident on the radome. The complex-valued amplitude of a rectangular component in the radome-bounded region is

$$E^R = \iint FTE^I \, dA \ ,$$

where E^I is the incident field amplitude, F is the receiving aperture distribution, and T is the radome transmittance, which is a complex-valued function of position for fixed frequency, wave polarization, and incidence direction. The integration extends over the region in which F has nontrivial magnitude. The receiving power is assumed proportional to $|E^R|^2$.

*The pattern depends on the orientation of the antenna in the radome as well as frequency and wave polarization direction.

The transmittance T in Equation (1) describes the electromagnetic effects of the radome. If we write $T = T e^{i\Delta\Phi}$, $\Delta\Phi$ is the phase delay produced by the radome. The quantity $\Delta\Phi$ is significant because it determines equiphase surfaces, and the tilt of these surfaces from the plane, incident wave is, to first order, proportional to boresight error.[*1] Figure 1-2 suggests a distorted wavefront. Because T strongly influences boresight error, its accurate computation is necessary for accurate performance predictions.

The transmittance depends on several electromagnetic wave processes. The known mechanisms are suggested in Figure 1-3 for externally incident plane waves. The direct wave usually has the largest magnitude. For large radomes and antennas the direct wave can be accurately computed over most of the aperture area by approximating the radome as locally plane. However, this approximation fails in the shadow of the tip because the radius of curvature of the radome tip approximates the wavelength. Some evidence exists for a scattered wave centered at the tip or the edge of a wedge.[3]

Data for other radomes suggests that if a wave is scattered by the tip, the wave is very directional; a simple cylindrical or spherical wave may be an overly approximate assumption. Any tip scattered wave becomes more significant as the diameter of the receiving antenna is reduced because the projection of the tip region becomes a larger fraction of the aperture area. Tip diffraction may be more important for direction-finding antennas that sense the difference between fields for halves of the aperture; for larger angles of arrival, the direct waves encounter large radii of curvature and produce balanced fields that cancel, but a tip wave would have distinct phase values.

The reflected wave, which comes from the shadowed side of the radome, occurs for incidence directions sufficiently far from axial incidence. The angle is approximately that of a cone tangent to the radome because the incident wave must first propagate through the directly illuminated side. The reflected wave increases sidelobe levels, and it causes boresight error for larger gimbal angles.

Guided waves exist in radomes. The modes are hardly cataloged for any special case. In general, evidence exists for slab guided modes in wedges and cones. Near the tip, the radome may be a hollow circular waveguide. Guided modes are negligible in many applications if the aperture is large, but they are growing in importance for newer smaller seekers that have antennas with small clearance from the radome. In addition, a guided wave can excite a tip diffracted wave and scattering at the base.

[*1] References are designated by a numerical superscript. They are collected in Section 6.

Until recently the direct wave was the main concern. However the other wave processes, which had produced rather subtle effects on systems, have become more significant as radome boresight error slope requirements become more stringent. In addition low sidelobe antennas require accurate design methods especially for reasonable bandwidths.

This report describes analyses and experiments on wave propagation through hollow dielectric shells. The purpose was to better describe the wave processes shown in Figure 1-3. Our aim was to analyze wavefront structure and the excitation of the various wave processes to estimate magnitude of the constituent fields. The results have helped develop anisotropic structures to reduce boresight error and its variation with wave polarization. Although completely polarization independent radomes seem unlikely, some reduction of this problem seems possible with dielectric gratings or periodically perforated metallic structures. Finally the results of the research are expected to help the analysis of high temperatures on radome boresight error.

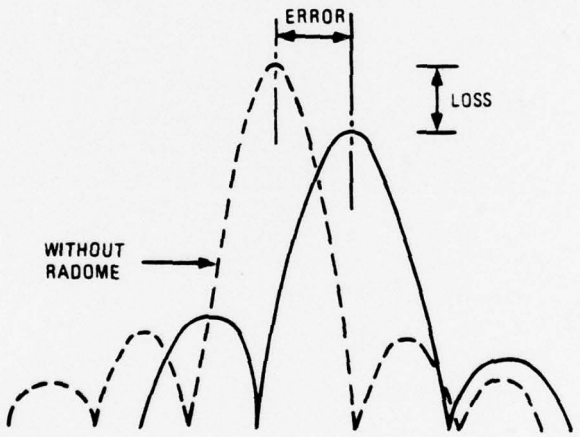

Figure 1-1. Radome Effects from Antenna Patterns

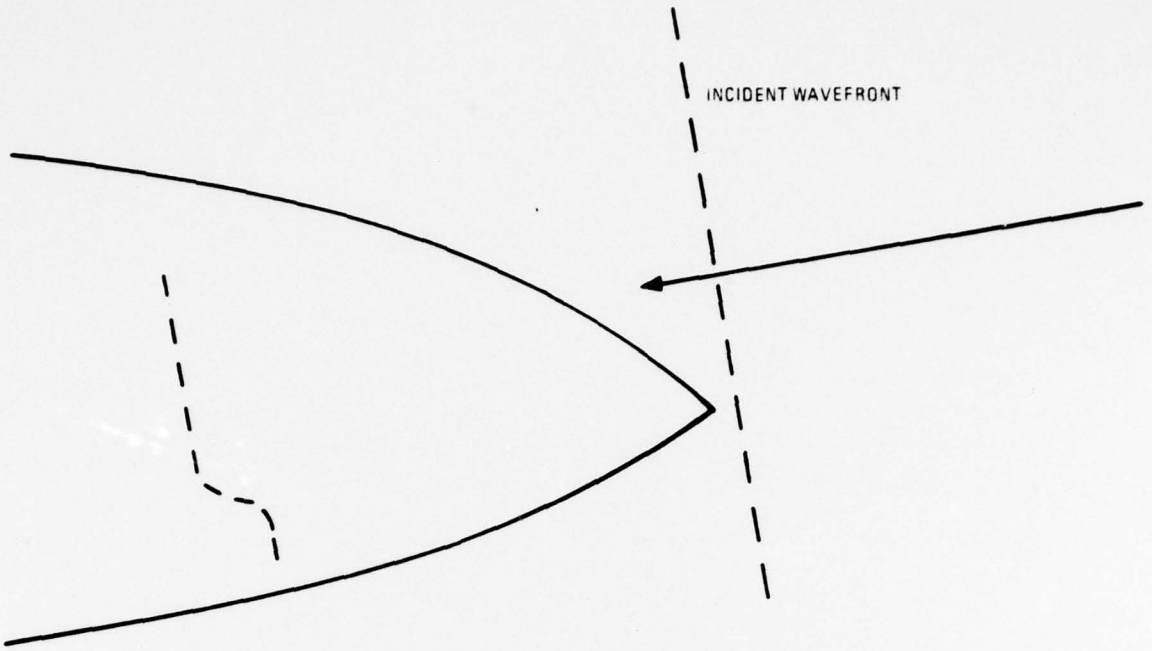

FL026

Figure 1-2. Distorted Wavefront

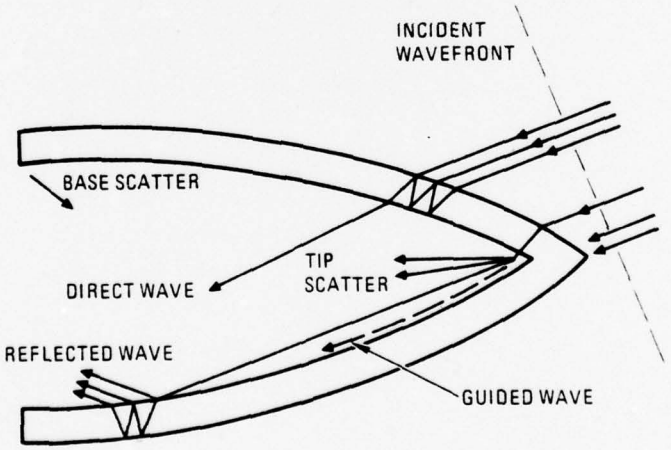

FL027

Figure 1-3. Wave Mechanisms in Hollow Dielectric

1.2 SUMMARY

This report describes analyses and experiments on wave propagation through hollow dielectric shells. The purpose was to describe quantitatively the wave process in radomes; see Figure 1-3. Specifically we sought to analyze wavefront structure and to estimate the magnitudes of the elementary waves that combine to form the wavefront. The research applies to the design of new missile radomes, to the analysis of aerodynamic heating on radome performance, and to the development of anisotropic radomes that reduce the polarization dependence of radome performance.

Section 2 summarizes the theory, which is the moment method. It is restricted to two-dimensional problems in its present form. Section 3 describes calculated results for plane waves incident on flat slabs and on hollow wedges for a range of incidence directions. Emphasis is on perpendicular polarization, but data for parallel also are given. Results are given for several slab and wedge dimensions. Section 4 describes near-field experiments. The results are compared with computed; and an accuracy criterion is given. Section 5 interprets the results. The measured and computed results show guided waves are strongly excited on slabs and wedges. The moment method correctly gives the magnitude of excitation. An independent model predicts spacings of fringes formed by interfering guided and refracted waves. Scattering by edges also occurs. These processes plus propagation through and reflection from the flat sides of a wedge produce complicated fields. A connection was made between observed boresight error properties of axially symmetric radomes and guided waves.

2. ANALYSIS

2.1 INTRODUCTION

Radome analysis requires approximations because few radomes are bounded by surfaces that are complete co-ordinate surfaces in separable systems. Cylinders, spheres, and large flat sheets can be analyzed by boundary value methods; however, ogival radomes usually are analyzed with diffraction integrals, and the radome is described as locally flat. Although approximate methods are often adequate, their accuracy is unknown in many cases. Discrepancies between measured and computed quantities are largest for small antennas and small radomes.

The causes of the discrepancies are only partially known. The approximation of local planeness in computing transmittance is mentioned by several authors. Our experience suggests additional causes, namely undersampling in computing transmittance. To appreciate undersampling consider Figure 2-1A. A single incident wave normal, a direct ray, passes through a point in the radome-bounded region. Transmittance is computed by approximating the radome as locally flat. This method gave good accuracy when the antenna in the radome had diameter 10 wavelength, but it failed for an antenna, diameter wavelength in a smaller radome. In contrast, the method suggested by Figure 2-1C gave excellent accuracy for the smaller radome. We interpret these results to suggest that the radome surface must be adequately sampled. Sufficiently dense sampling introduces the variation of the surface normal into a sum of terms that describe transmittance at a point. The lack of this variation in the direct ray method seems a cause of discrepancies.

Another cause of discrepancies seems to be the omission of some wave processes from most analytical methods. As mentioned in Section 1, guided waves, scattering by the tip, and by the base of the radome exist, but these waves are usually omitted from numerical analyses. A main objective of this project was to determine the magnitude of the distinct wave types in radome-bounded regions.

Because accurate radome analysis is involved, we considered simpler problems, the hollow dielectric wedge and the flat slab, both with finite width, as shown in Figure 2-2. In addition, we considered the half cylinder. These problems are preliminaries to axially-symmetric radomes. We considered two directions of wave polarization. One is TM or perpendicular polarization. The other is TE or parallel polarization. The approach is to utilize the moment method for the numerical solution of integral equations.

The theoretical basis for the analysis of slabs, hollow wedges, and hollow cylinders is the moment method; in particular, a form developed by J. H. Richmond.[3,4] The next two subsections summarize the theory.

2.2 TM CASE, OR PERPENDICULAR POLARIZATION

The starting point is an integral equation for the scattered electric field. This equation is derived from Maxwell's equations with the definition that E^T, the total field, which is the field in the presence of a scatterer is the sum of E^I, the incident field, which is the field without the scatterer, and the E^S the scattered field. That is

$$E^T = E^I + E^S. \tag{1}$$

Maxwell's equations are then rewritten in the form of the free space equations with a polarization current that describes the effect of the dielectric scatterer. For perpendicular polarization the integral equation gives the scattered field as

$$E^S(x,y) = (ik^2/4) \iint (\kappa - 1) E^T(x',y') H_o^{(1)}(k\rho)\,dx'dy', \tag{2}$$

where $\rho = \left[(x-x')^2 + (y-y')^2\right]^{1/2}$, with (x, y) the co-ordinates of the observation point and (x', y') those of the integration point. $H_o^{(1)}(k\rho)$ is a zero order Handel function of the first kind, it represents an outward going wave with our assumed time convention $\exp(-i\omega t)$, with t time and frequency ω. By adding E^S in Equation (2) to E^I, we obtain an integral equation for E^T.

$$E^T - (ik^2/4) \iint (\kappa - 1) E^T(x',y') H_o^{(1)}(k\rho)\,dx'dy' = E^I. \tag{3}$$

To solve Equation (3), divide the two dimensional dielectric scatterer into cells like those in Figure 2-3. The cells must be small enough to justify assuming E^T constant in any one cell. We assume the relative dielectric constant κ is constant in any one cell. From Equation (3) we get

$$E_m^T - (ik^2/4) \iint (\kappa_m - 1) E(x_m, y_m) H^{(1)}(k\rho)\,dx'dy' = E^I. \tag{4}$$

In Equation (4) m is an index that labels the cells, and N is the total number of cells. In fact Equation (4) is a system of N equations. The next step is to evaluate the double integrals in Equation (4). This integration is straightforward for cells that are right circular cylinders of radius a and with infinite length (in the z' direction, which is perpendicular to the x',y' plane). There are two cases to consider. In one, the observation point is outside the cell. If n denotes the integration cell and m the observation cell, then for $m \neq n$

$$(-ik^2/4)I = (-i\pi ka/2)J_1(ka)H_o^{(1)}(k\rho_{mn}), \tag{5}$$

where ρ_{mn} denotes the distance between (x_m, y_m) and $x_n, y_n)$, I is the double integral in Equation (4), and J_1 denotes the first order Bessel function. In the second case, $m = n$

$$(-ik^2/4)I = (-1/2)\left[\pi k\ a\ H_1^{(1)}(ka) + 2i\right]. \tag{6}$$

With Equations (5) and (6), we obtain

$$\sum_{n=1}^{N} C_{mn}E_n^T = E_m^I, \tag{7}$$

for $1 \leq m \leq N$. The C_{mn} are matrix elements.

To find E_n^T it is necessary to solve the system of Equation (7). This solution may be found by inverting the matrix (C_{mn}). The matrix inversion is restricted by storage capacity of computers because the assumption that E^T is constant in any one cell requires small cells. The small dimensions require large N for structures comparable in size to practical radomes.

Direction solution of equation 7 is being studied. The next section gives calculations for four special cases that were chosen to reveal some aspects of wave propagation in and around radomes.

2.3 TE CASE OR PARALLEL POLARIZATION

This case is more complicated than the preceding because another term arises in the integral equation since the gradient of the scalar potential contributes to the electric field,

$$E = -\nabla\phi - \frac{\partial A}{\partial t}. \tag{8}$$

With the co-ordinate system of Figure 2-2, the incident field is

$$E^I = \hat{x}\, E^I_x(x,y) + \hat{y}\, E^I_y(x,y); \tag{9}$$

The total field E has a similar representation. Two sets of coupled equations result, we obtain

$$\begin{aligned} \sum_{n=1}^{N} (A_{mn}E_{xn} + B_{mn}E_{yn}) &= E^I_{xm} \\ \sum_{n=1}^{N} (C_{mn}E_{xn} + D_{mn}E_{yn}) &= E^I_{ym} \end{aligned} \tag{10}$$

where A_{mn}, B_{mn}, C_{mn}, D_{mn} are matrix elements; their definitions are given in Reference 4.

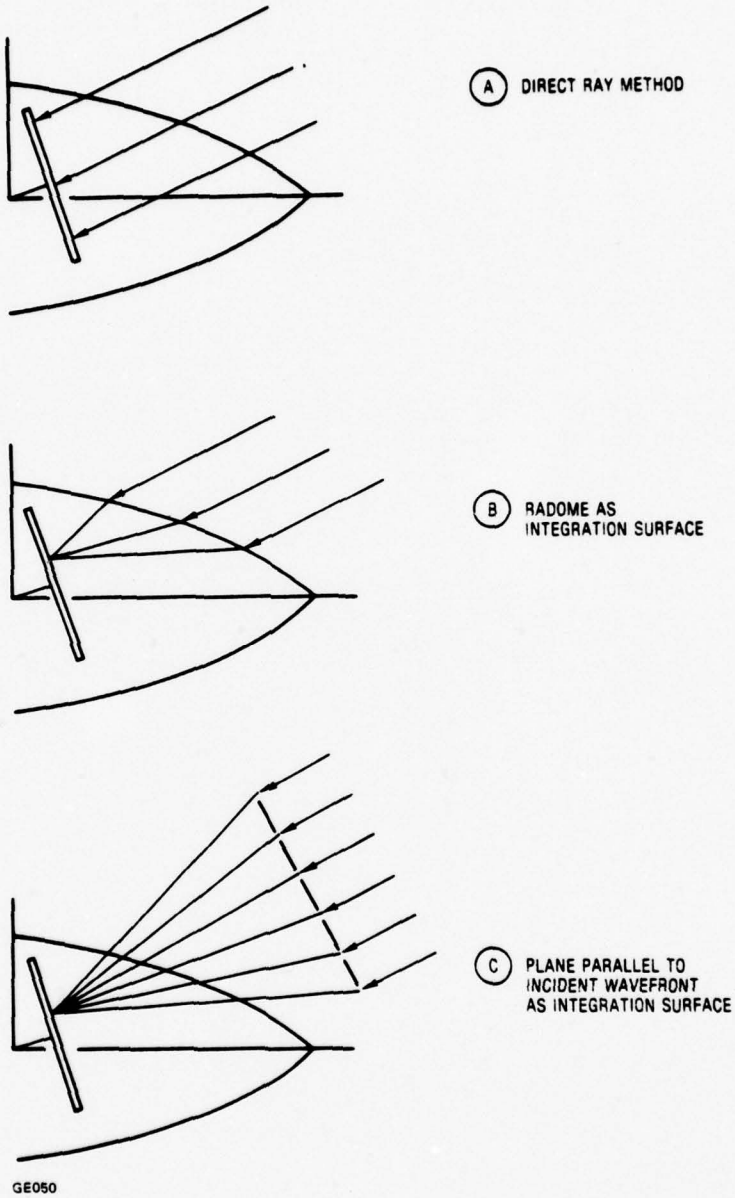

Figure 2-1. Three Methods for Computing Radome Boresight Error

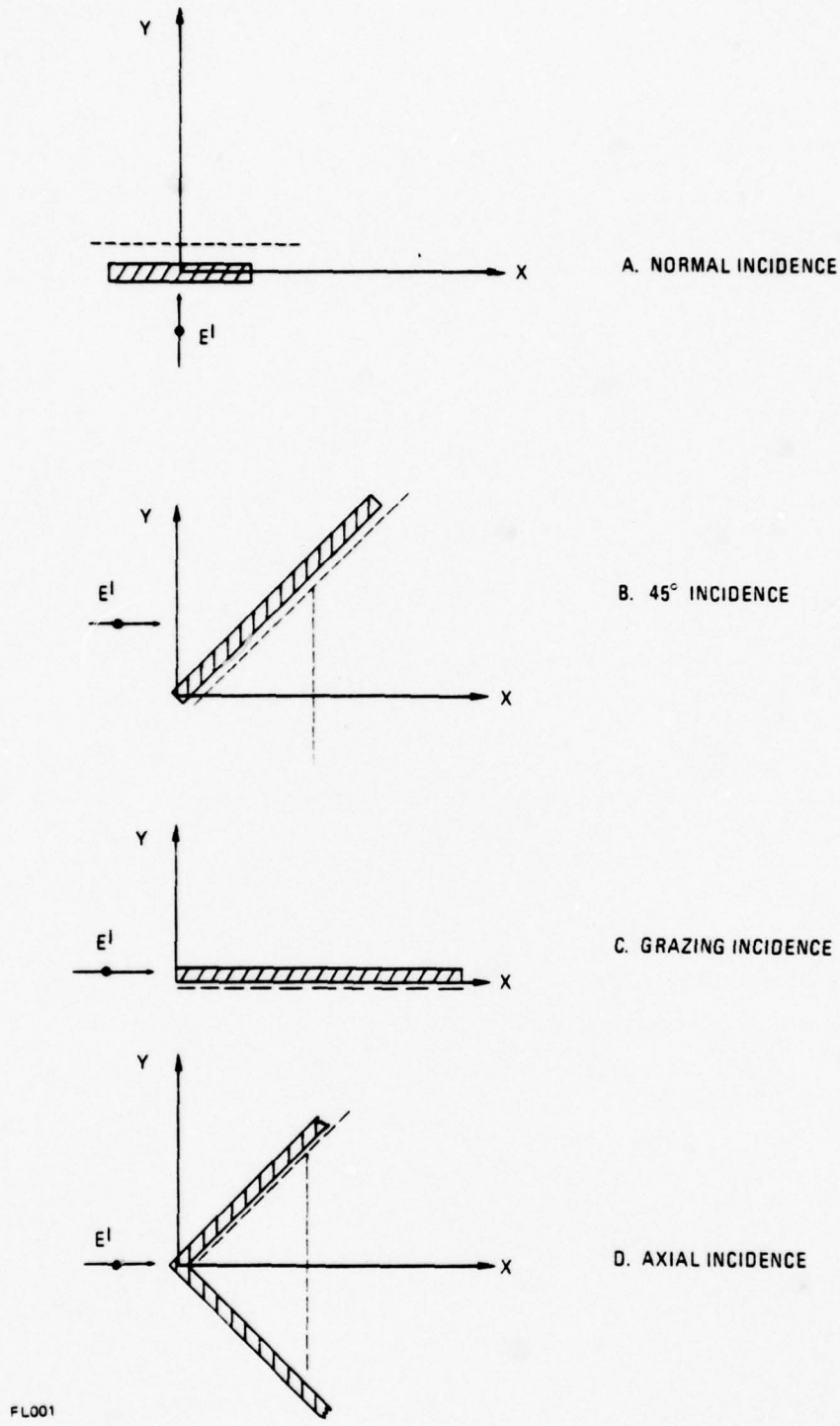

Figure 2-2. Orientations of Slabs and Hollow Wedge. The dashed lines show where the field was evaluated. For the wedge, a range of incidence directions was considered.

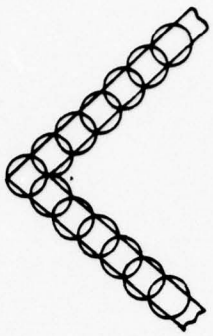

GE001

Figure 2-3. Approximating a Hollow Wedge with a Set of Right Circular Cylinders.

3. COMPUTATION

This section gives the results of moment calculations for slabs, hollow wedges, and hollow hemi-cylinders. The co-ordinate systems of Figures 3-1, 3-2, and 3-3 were utilized. Cell radius a was chosen to make the sum of the areas of the approximating cylinders equal that of the scattering object. Frequency was 9.375 GHz. Dielectric constant κ was 2.6; to simulate acrylic plastics which we utilized in experiments. Loss tangent was zero; this approximation is good because the value for acrylic plastics is 0.006.

3.1 PERPENDICULAR POLARIZATION

3.1.1 SLAB: 4 IN. WIDTH, NORMAL INCIDENCE

The fields inside the slabs were computed at the center of the approximating cylinders to study numerical convergence and to compare the results with those for infinitely broad sheets. Incidence was normal as in Figure 2-2a. Figure 3-4 shows $|E^T|$ inside a slab, width 4 in. and thickness 0.25 in. Cell radius a was 0.143 in.; spacing was 0.25 in. The number of cells N was 17. Note the values fluctuate about that for infinite flat sheets. For comparison, Figure 3-5 shows $|E^T|$ inside the same slab, but for N = 120 and for smaller cells. For the slab midplane the results are similar for both values of N, but the oscillations have greater amplitude in Figure 3-5. The field also depends on Y within the slab.

The power transmittance (the normalized intensity $|E^T/E^I|^2$ outside the slab) of the 0.25 in. thick slab is shown in Figure 3-6 for N = 17 and in Figure 3-7 for N = 120. These figures illustrate how transmittance computations depend on N.

Figure 3-8 shows $|E^T/E^I|^2$ for a slab with thickness 0.125 in. In this case the slab was approximated with a single row of 33 cylinders.

3.1.2 SLAB: 10 IN. WIDTH, NORMAL INCIDENCE

As the width of a slab increases we expect the field to approach that computed for an infinitely broad slab. Therefore we considered a second, broader slab, width 10 in. The internal field magnitude is shown in Figure 3-9 for two thicknesses, 0.125 and 0.250 in. Figure 3-10 shows transmittance at several distances behind the 0.25 in. slab; all are in the nearfield of the slab. Figure 3-11 shows transmittance for the 0.125 in. slab. Note in Figure 3-11 the transmittance differs slightly from that for a flat slab in the central half of the slab, but nearer the edges the moment method result oscillates about the flat sheet value.

3.1.3 SLAB WITH DIELECTRIC STRIPS

Figure 3-12 shows an array of dielectric cylinders that represents thin strips on a dielectric slab. Slab thickness was 0.125 in., and width was 4.38 in. Each strip was 0.30 in. high and 0.060 in. thick. The slab was represented by 36 cylinders each with diameter 0.071 in., and each strip had 5 cylinders, diameter 0.034 in. Computed values of $|E^T/E^I|^2$ are shown in Figure 3-13 for normal incidence on the slab with strips.

The effects of the strips on power transmittance is illustrated in Figure 3-14, which shows the computed data for the slab with and without the 15 strips. The strips increase transmittance averaged over the slab by approximately 1/3 dB.

3.1.4 SLAB, 45° INCIDENCE

For 45° incidence, as in Figure 2-2b, the internal field, at the centers of the cylinders approximating a slab, is shown in Figure 3-15 for six values of N(10, 11, 21, 41 and 42) corresponding to six distinct slab lengths. The intensity outside the slab is shown in Figure 3-16 for N = 41; in this case intensity was evaluated on the line 0.225 in from the slab midplane and on the shadowed side. This line is 0.1 in. from the slab. The intensity on a transverse line parallel to the incident wavefront is shown in Figure 3-17 for two values of N(41 and 42).

The internal fields, Figure 3-15 depend on N, but this dependence has a physical rather than numerical cause. The deep minima result from guided waves interfering with internal plane wave fields; we justify this interpretation in Section 5. The small rapid oscillations result from interference of guided waves travelling in opposite directions; see Section 5. Addition of another cylinder increased the path length of one of the waves by approximately π, causing maxima and minima of the small oscillations to alternate in locations.

Another physical cause exists for fluctuations on transverse paths as in Figure 3-17. The increase of N extends the slab. For small N the end of the slab is closer to the source than the observation points. The larger N the end is farther from the source. Figure 3-18 illustrates this point through calculations of the scattered field.

3.1.5 SLAB, GRAZING INCIDENCE

For grazing incidence as in Figure 2-2c, Figure 3-19 shows the intensity of the total field in a 0.25 in. thick 10 in. long slab. The field was evaluated at the centers of the cells for two values of N(40 and 41). We see from the 4 dB value of $|E^T|^2$ that $|E^T|$ exceeds the unit magnitude of the incident field.

The external intensity is in Figure 3-20 for two lines parallel to the slab plane, and Figure 3-21 shows $|E^T|^2$ at a larger distance.

3.1.6 WEDGE, 0.25 IN. THICK, AXIAL INCIDENCE

For a hollow wedge, as in Figure 3-22 shows $|E^T|$ inside the walls for several values of N, where (N-1)/2 cells are in each wall and one cell is at the tip. The field on transverse paths (fixed y values) is shown in Figure 3-23 for the wedge represented by two slabs of equal thickness, and in Figure 3-24 for two slabs of slightly different thickness. Note the additional variation in the second case. The field variation on the symmetry plane is shown in Figure 3-25.

To obtain a comprehensive view of the field we drew contour plots of the scattered field; see Figure 3-26 for magnitude and 3-27 for phase. The biggest value of $|E^S|$ was 1.65 compared to the unit value $|E^I|$.

3.1.7 WEDGE, 0.125 IN. THICK WALLS

Figure 3-28a and b shows the field intensity inside a hollow 90° wedge, thickness 0.125 in., with walls 10 in. long; results are given for four incidence directions ϕ_i equal to 0°, 22.5°, 45°, and 67.5°. Note ϕ_i equal 0° gives axial incidence; ϕ_i equal 45° gives normal incidence on one slab and grazing incidence on the other. The value 67.5° gives reflections.

Because many graphs are necessary to represent the field behind a wedge, we pictorially displayed the data. Figures 3-29 and 3-30 show these plots of the scattered field E^S for the wedge with 0.125 in. thick walls. The data were quantized into 11 levels so the representation is rather coarse. Therefore we increased the number of levels to 22; see Figure 3-31 and 3-32.

3.1.8 HEMICYLINDER

Figure 3-33 shows the geometry. The hemicylinder had diameter 4.8 in. and thickness 0.125 in. The direction of the incident wave was specified by the angle ϕ. The hemicylinder was approximated by a set of small solid cylinders, radius a, on a hemicircle of radius R. See Figure 3-34. Computations were done for R equal 2.5 in. and a equal 0.071 in.; ρ the distance between hemicylinders was .125 in.

Figure 3-35 shows intensity $|E^T/E^I|^2$ for $\phi_i = 90°$ at two values of y. For comparison, the figure also shows values computed with a ray tracing method that approximates the radome as locally flat. The phase delay arg E^T/E^I is shown in Figure 3-36. Figures 3-37 and 3-38 show intensity and phase for $\phi_i = 45°$.

Because anisotropic gratings have been utilized to improve radomes, we applied the moment method to their analysis. Figure 3-39 shows the geometry. Transmittance is shown in Figure 3-40 for $\phi_i = 0°$.

3.2 PARALLEL POLARIZATION

3.2.1 SLAB: 0.125 IN. THICK, GRAZING INCIDENCE

Figure 3-41 $|E^T|$ inside a slab, thickness 0.125 in. length 4 in. for grazing incidence. Figure 3-42 shows $|E^T/E^I|^2$ outside the slab at five lines parallel to the slab.

3.2.2 SLAB: 0.235 in. THICK, GRAZING INCIDENCE

Figure 3-43 shows $|E^T|$ inside a slab, thickness 0.235 in., length 4 in. for grazing incidence. Results are shown for a single row of cylinders, N = 17, and for two rows N = 68. The external intensity $|E^T/E^I|^2$ is shown in Figure 3-44.

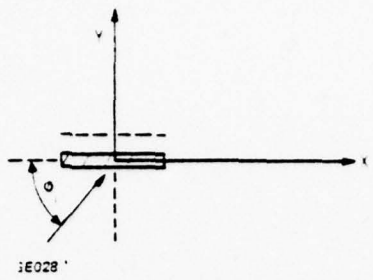

Figure 3-1. Co-ordinates for a Slab

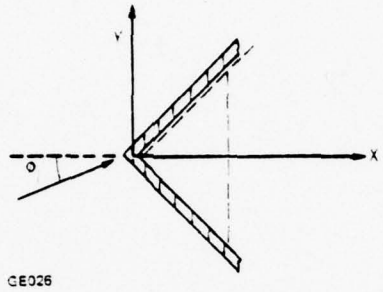

Figure 3-2. Co-ordinates for Wedge

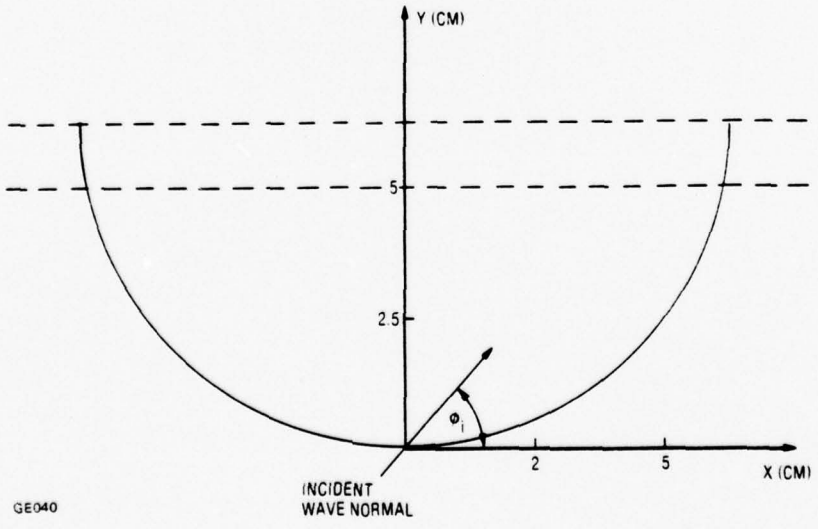

Figure 3-3. Geometry for Hemi-Cylinder and Incident Wave Directions

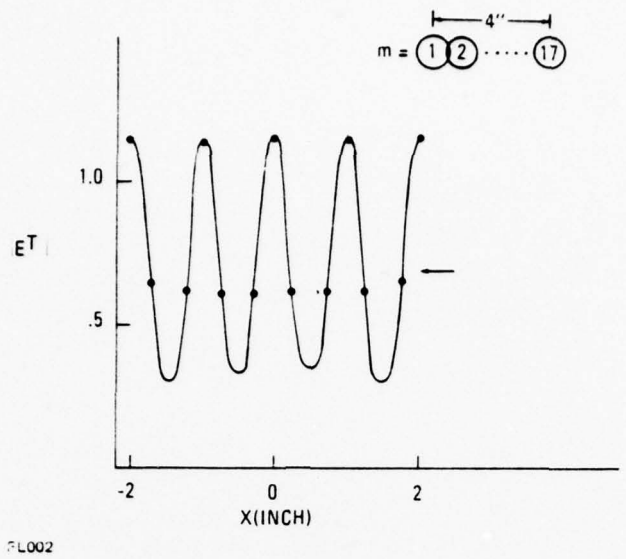

Figure 3-4. Internal Field Magnitude for 1/4 in. x 4 in. x 18 in. Slab, $\kappa = 2.6$, for Normal Incidence. Calculated for N = 17, a = 0.143 in., $\rho = 0.25$ in., at y = 0. The arrow shows the value predicted by flat sheet theory.

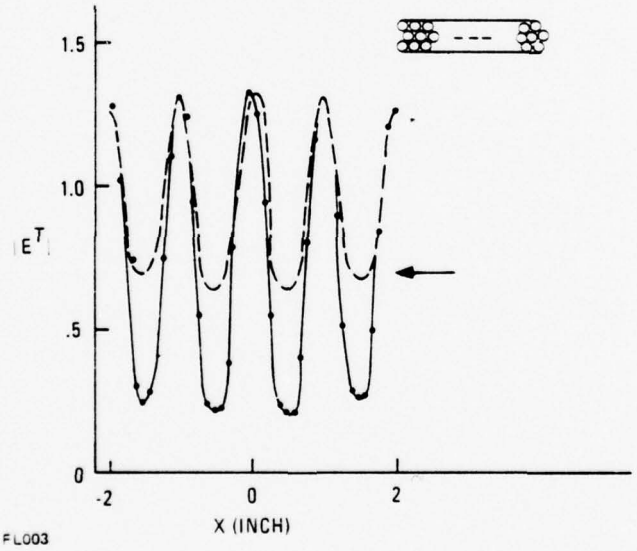

Figure 3-5. Internal Field Magnitude for 1/4 in. x 4 in. x 18 in. Slab, $\kappa = 2.6$, for Normal Incidence. Calculated for N = 120, a = 0.053 in., $\rho = 0.100$ in.; Hexagonal Arrangement of Cells for y = 0 (——); for y = ±0.08 in. (----). The arrow shows the value predicted by the theory of flat sheets at the central row of cylinders.

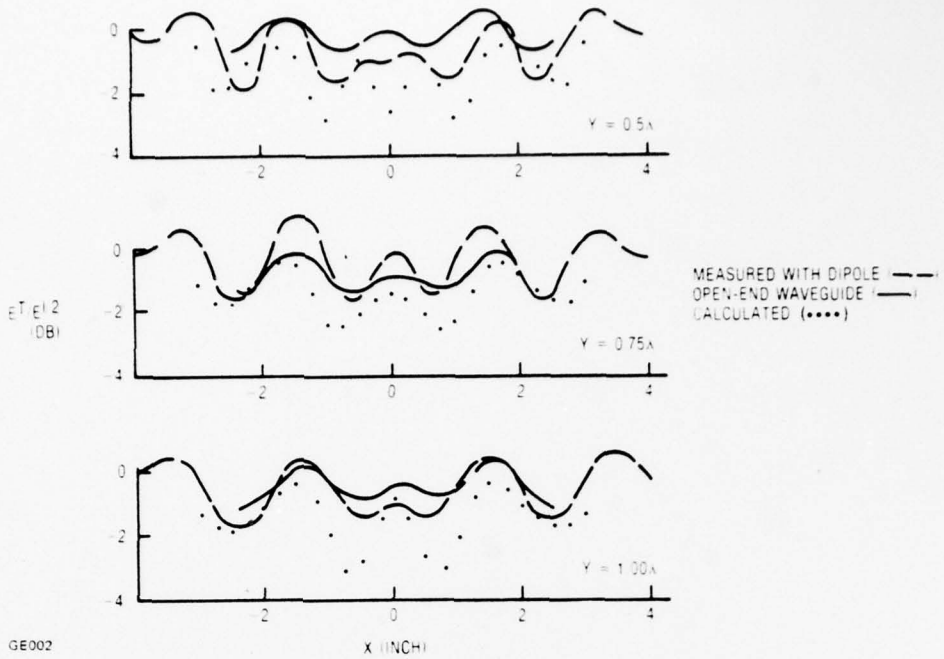

Figure 3-6. Power transmittance of 0.24 by 4.0 in. slab; $\kappa = 2.6$; $\phi_i = 0°$; Calculated: N = 17, a = 0.143 in., ρ = .250 in

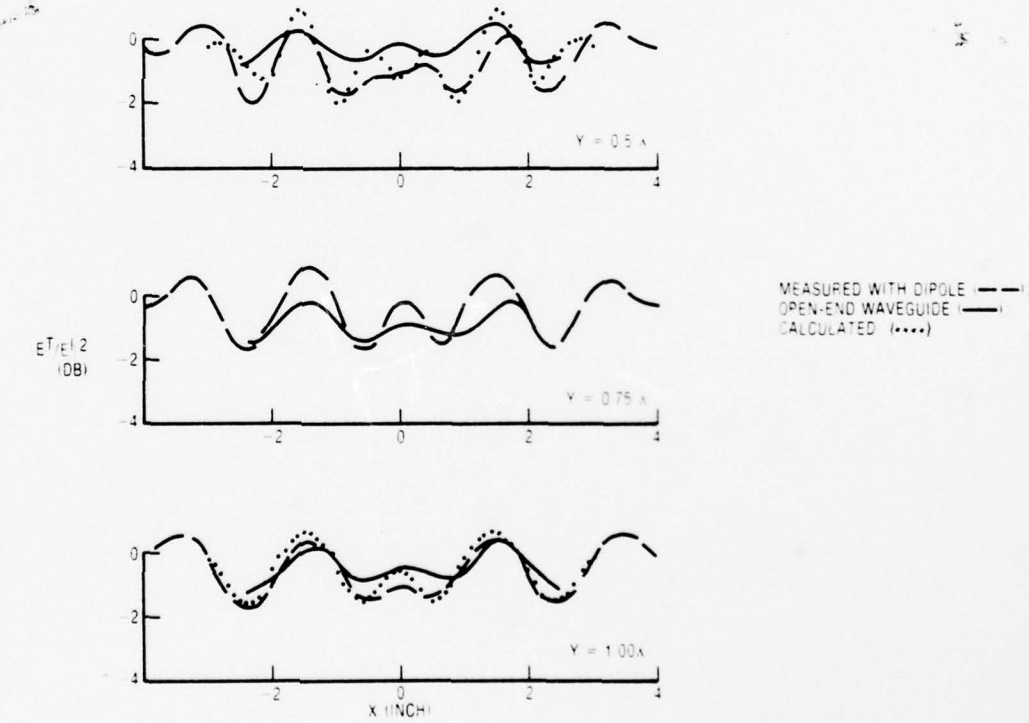

Figure 3-7. Power transmittance of slab in Figure 3-6 but calculated N = 120, a = 0.053 in., ρ = 0.10 in.

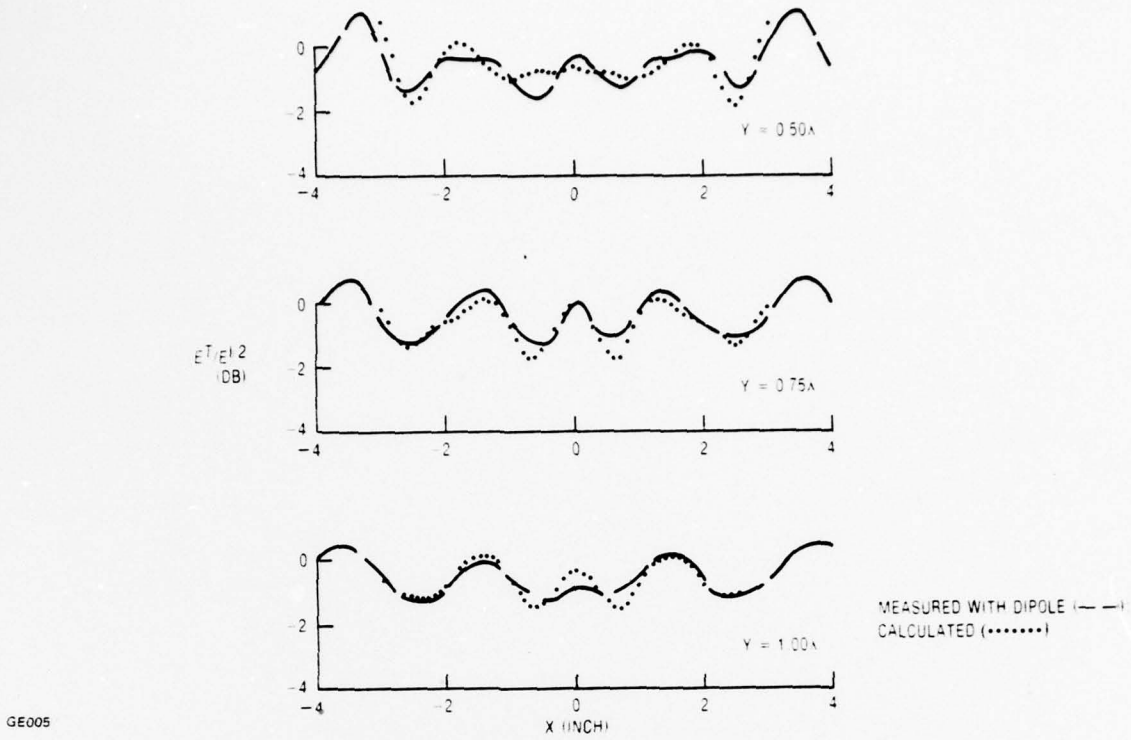

Figure 3-8. Power transmittance of 0.125 by 4.0 in. slab: $\kappa = 2.6$, $\phi_i = 90°$. N = 33, a = 0.0715 in., $\rho = 0.125$ in.

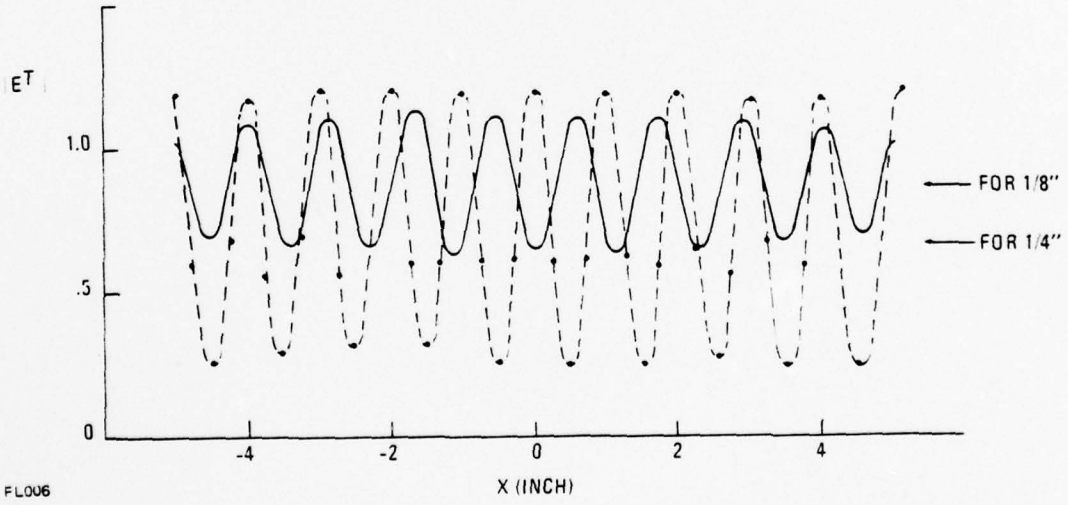

Figure 3-9. Total Field Amplitude in Dielectric Slab, $\kappa = 2.6$, Normal Incidence. Computed for N = 41, a = 0.143 in., $\rho = 0.25$ in. (for 1/4 in. thickness the dashed curve) and N = 81, a = 0.0715 in., $\rho = 0.125$ in. (for 1/8 in. thickness the solid curve). The arrows indicate the values predicted by flat sheet theory.

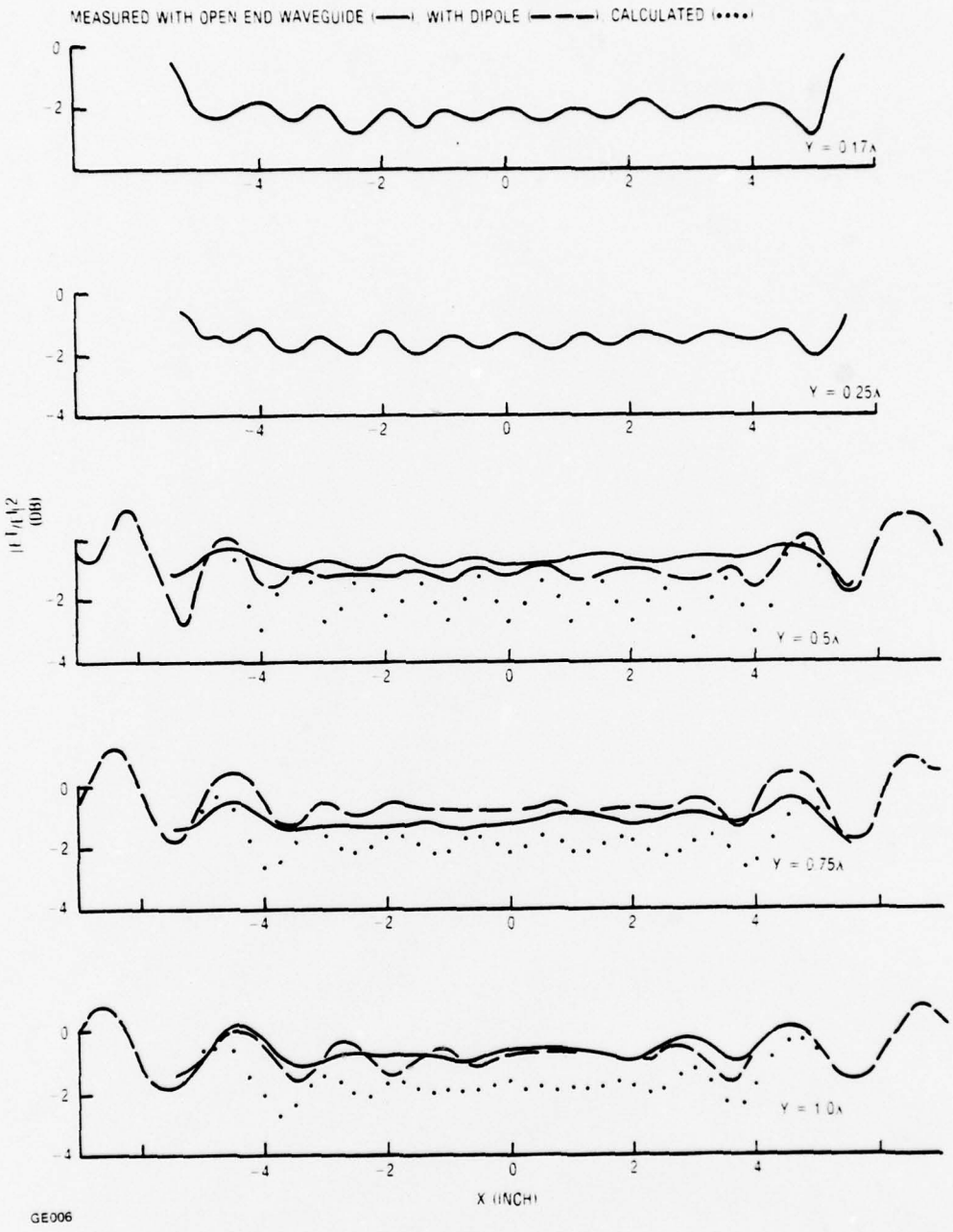

Figure 3-10. Power transmittance of 0.25 in. by 10 in. by 18 in. slab, $\kappa = 2.6$, N = 41; for normal incidence a = 0.143 in., $\rho = 0.25$ in.

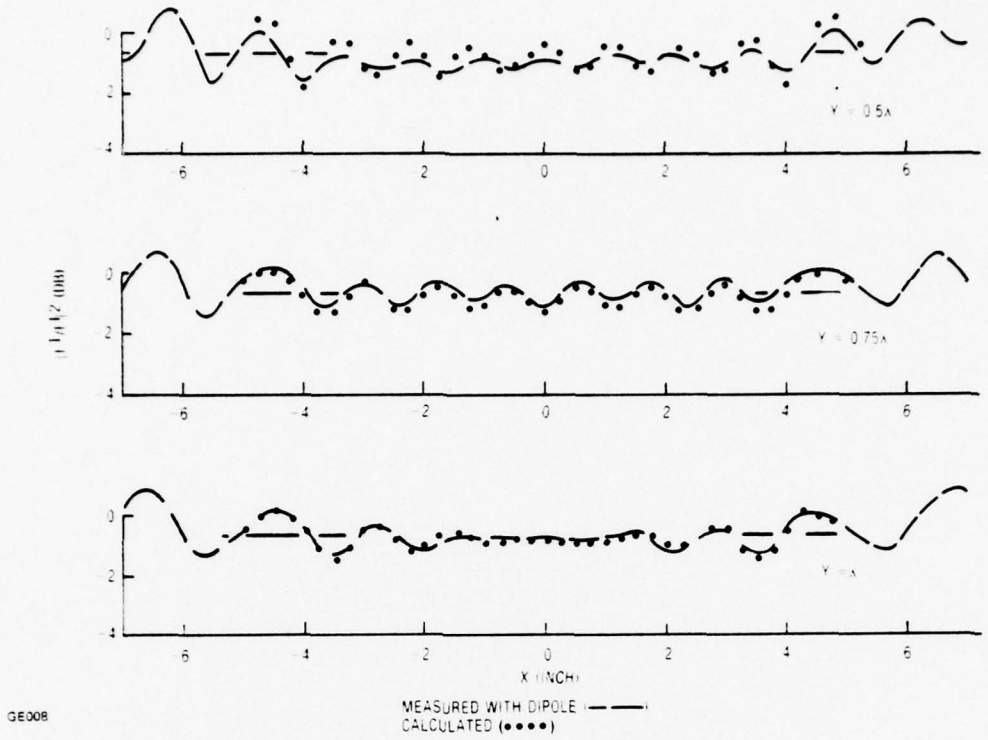

Figure 3-11. Power transmittance of 0.125 by 10 by 18 in. Plexiglas slab; Calculated: N = 81, a = .0715 in., ρ = .125 in. The broken heavy line is the value for an infinite slab.

Figure 3-12. Array of 11 cylinders to represent 4.38 in. wide slab 0.125 in. thick with 15 strips.

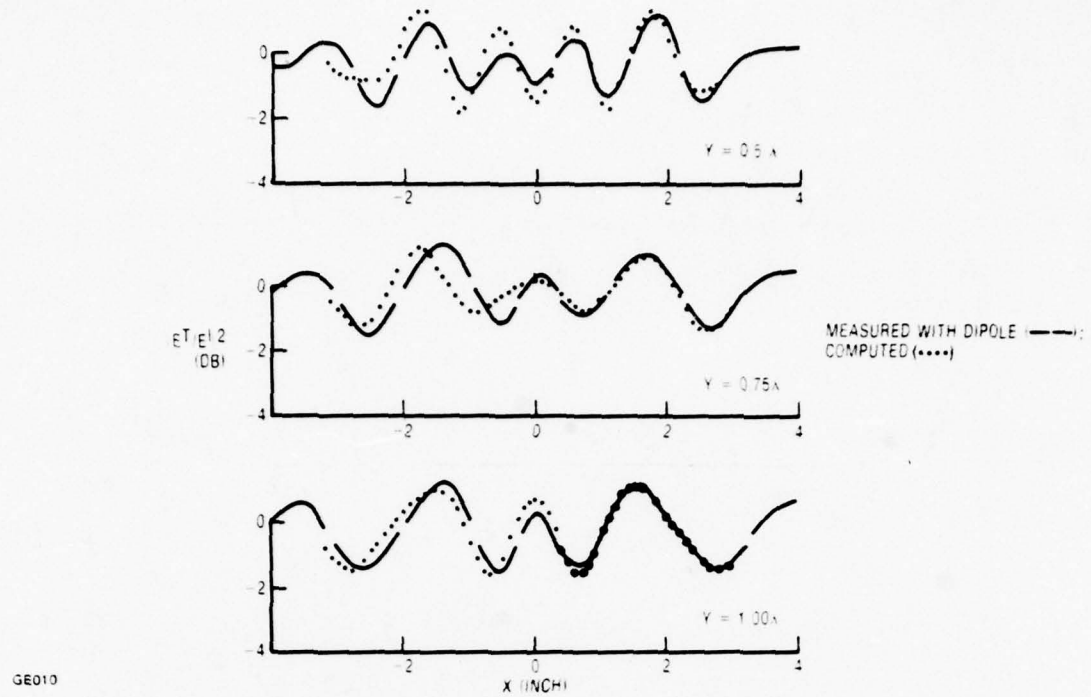

Figure 3-13. Power transmittance of 0.125 by 4.38 in. slab with 15 strips: Computed for N = 111, a = 0.074 in. and 0.034 in., ρ = 0.125 in. and 0.06 in.

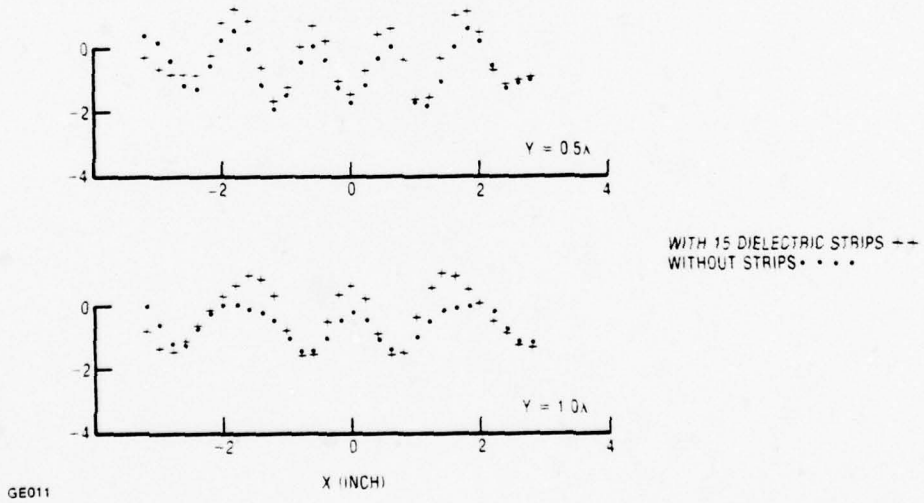

Figure 3-14. Power transmittance of 0.125 by 4.38 in. slabs: κ = 2.6, θ_i = 0°;
with 15 dielectric strips: N = 111; a = 0.071 in.; 0.034 in.
ρ = 0.125 in.; 0.060 in.
without strips: N = 36; a = 0.071 in.; ρ = 0.125 in.

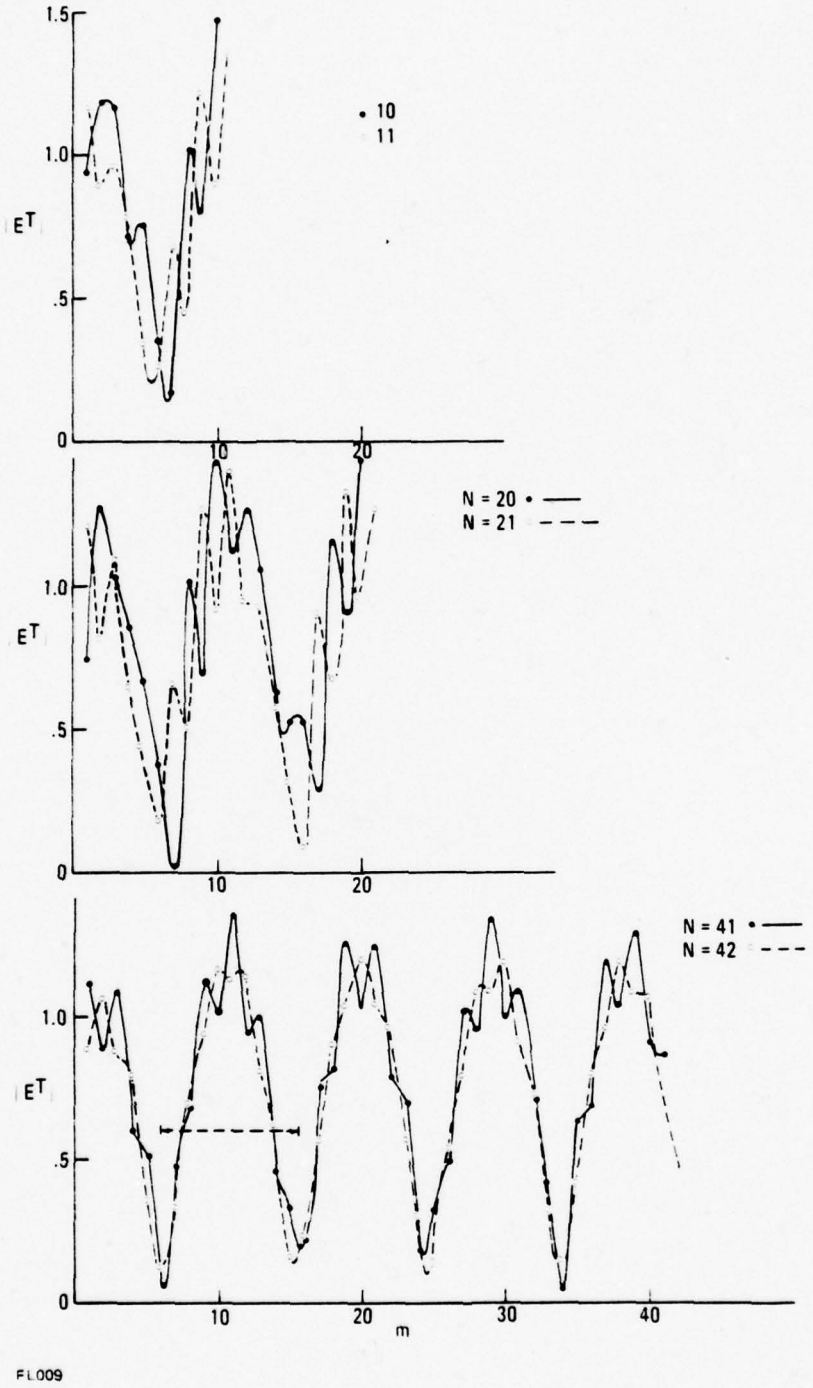

Figure 3-15. Total Field Magnitude Inside Dielectric Slabs for 45°, λ = 1.259 in. Computed for a = 0.143 in., ρ = 0.250 in. The arrows show theoretical fringe spacings for guided waves.

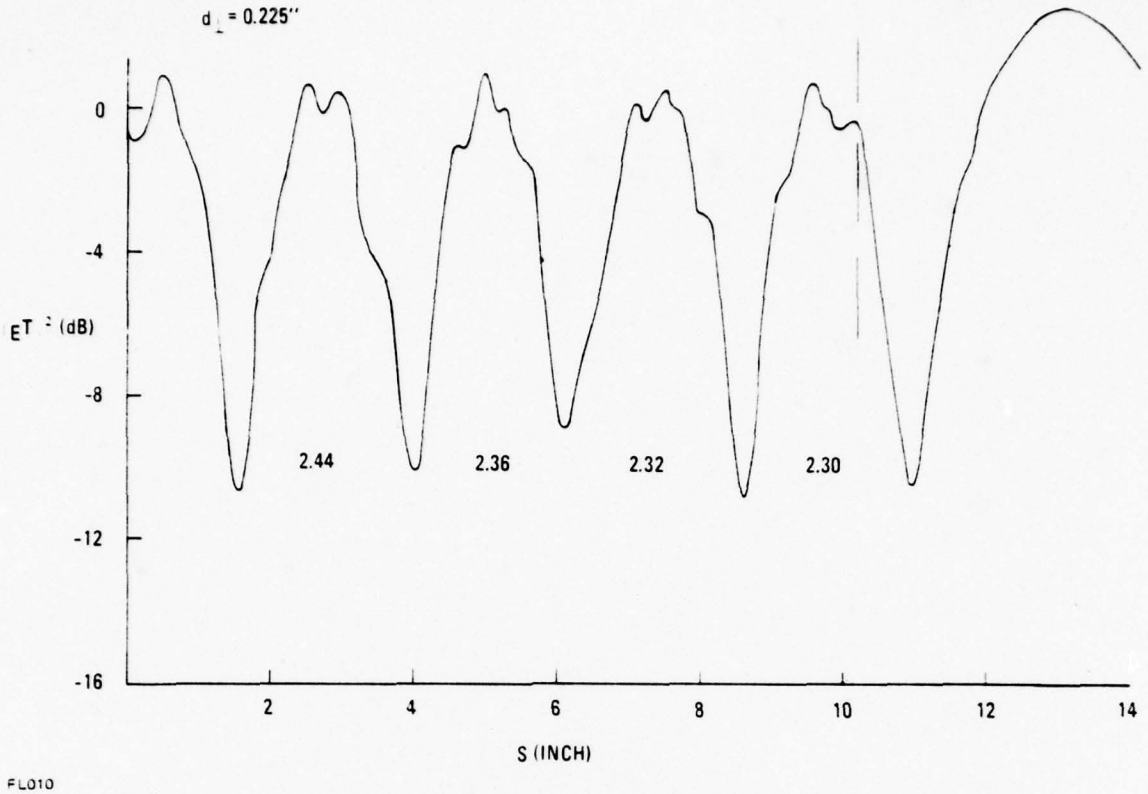

Figure 3-16. Intensity in Total Field at Distance 0.225 in. from Slab Midplane. Thickness 0.25 in., length 10 in. Computed for N = 41, a = 0.143 in., ρ = 0.25 in., λ = 1.259 in., κ = 2.6. The numbers between minima are spacings in inches.

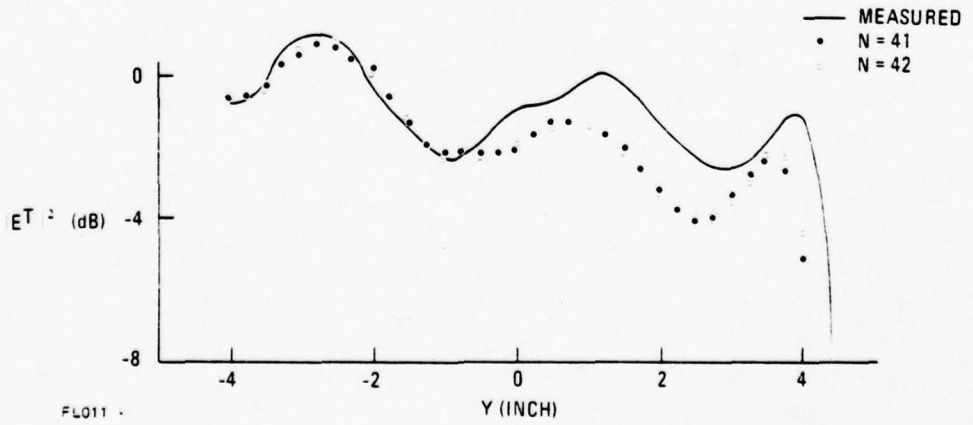

Figure 3-17. Intensity Behind Dielectric Slab, κ = 2.6, λ = 1.259 in. for 45° Incidence. Measured for 0.23 in. x 10 in. x 18 in. slab with dipole probe at x = 4.48 in. (——). Calculated for N = 41 (°); for N = 42 (o). ρ = 0.25 in., a = 0.143 in.

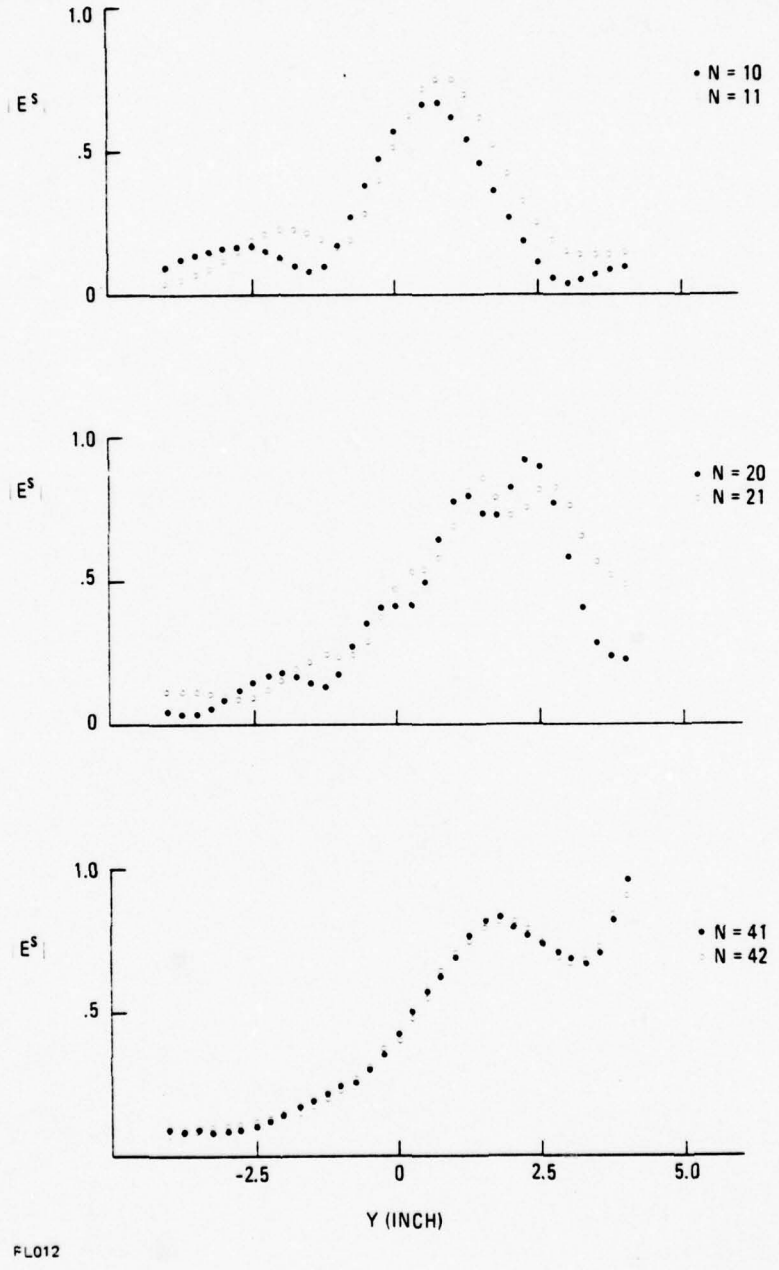

Figure 3-18. Scattered Field Magnitude Behind Slab (10 in. x 18 in. x 0.23 in., κ = 2.6) for 45° Incidence at x = 4.48 in.

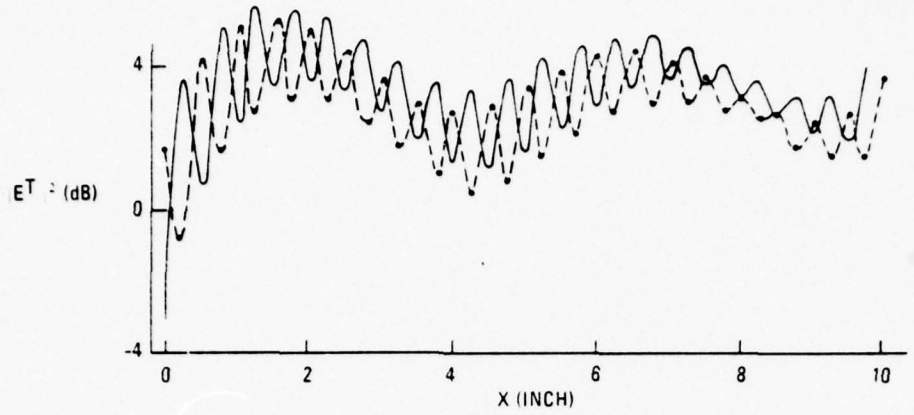

FL014

Figure 3-19. Total Field Intensity Inside Slab 1/4 in. Thick, 10 in. Long. N = 40 (—), N = 41 (---), a = 0.143 in., ρ = 0.25 in., κ = 2.6.

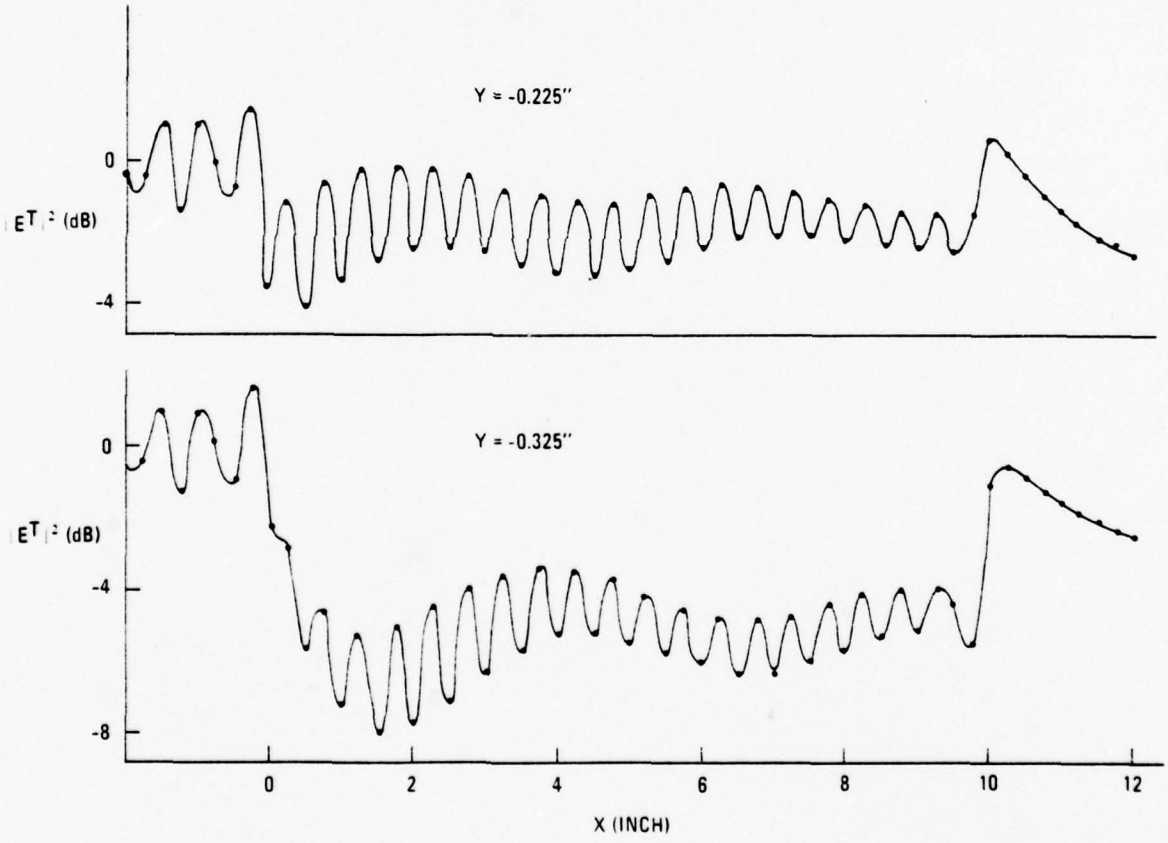

FL015

Figure 3-20. Intensity Near Dielectric Slab, κ = 2.6, 1/4 in. x 10 in. x 18 in., Calculated for N = 40, a = 0.143 in., ρ = 0.25 in., λ = 1.259 in.

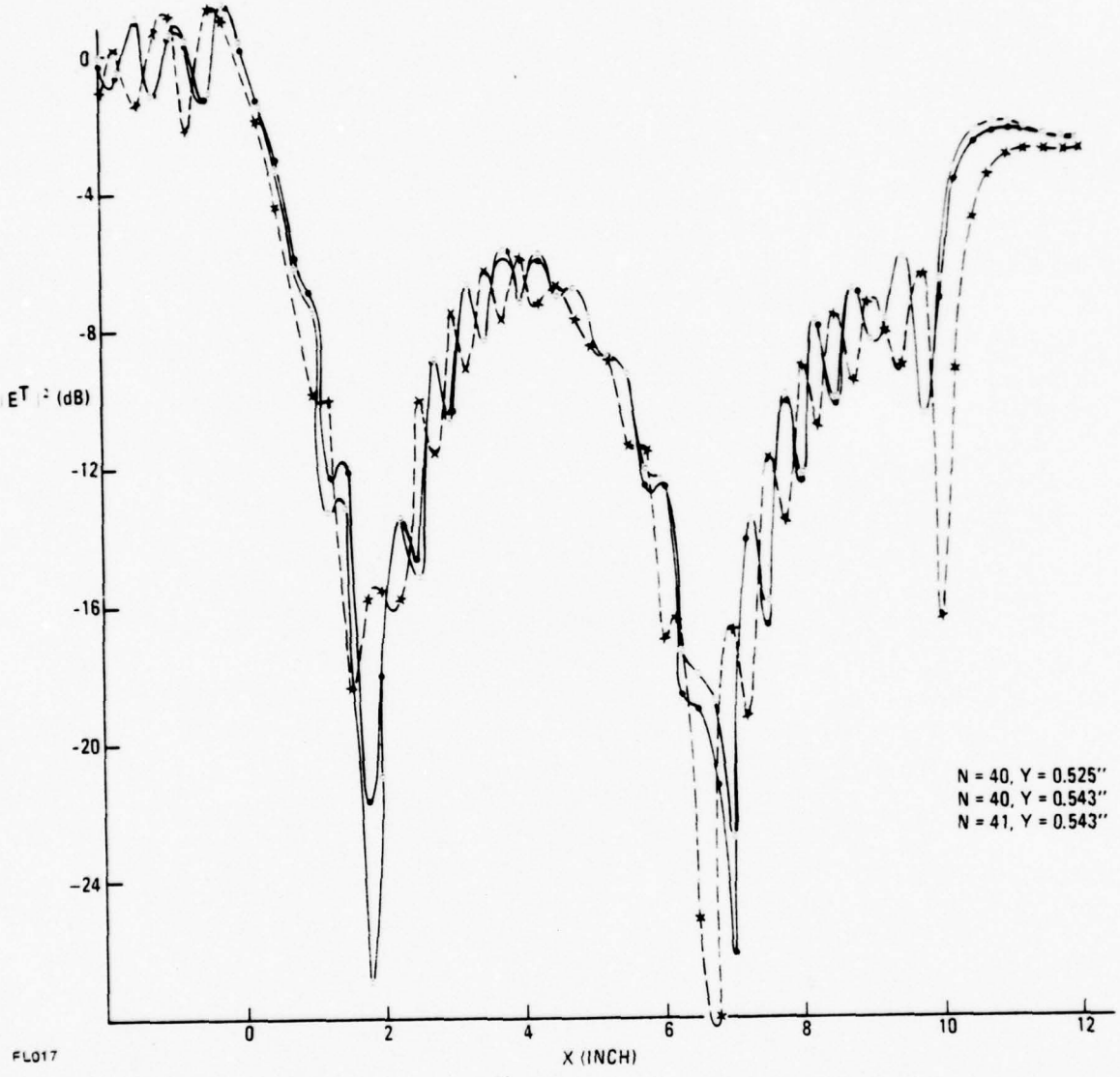

Figure 3-21. $|E^R|^2$ **Outside Dielectric Slab,** $\kappa = 2.6$ **for Grazing Incidence, With** $\lambda = 1.259$ **in.,** $\rho = 0.25$ **in. and** $a = 0.143$ **in.**

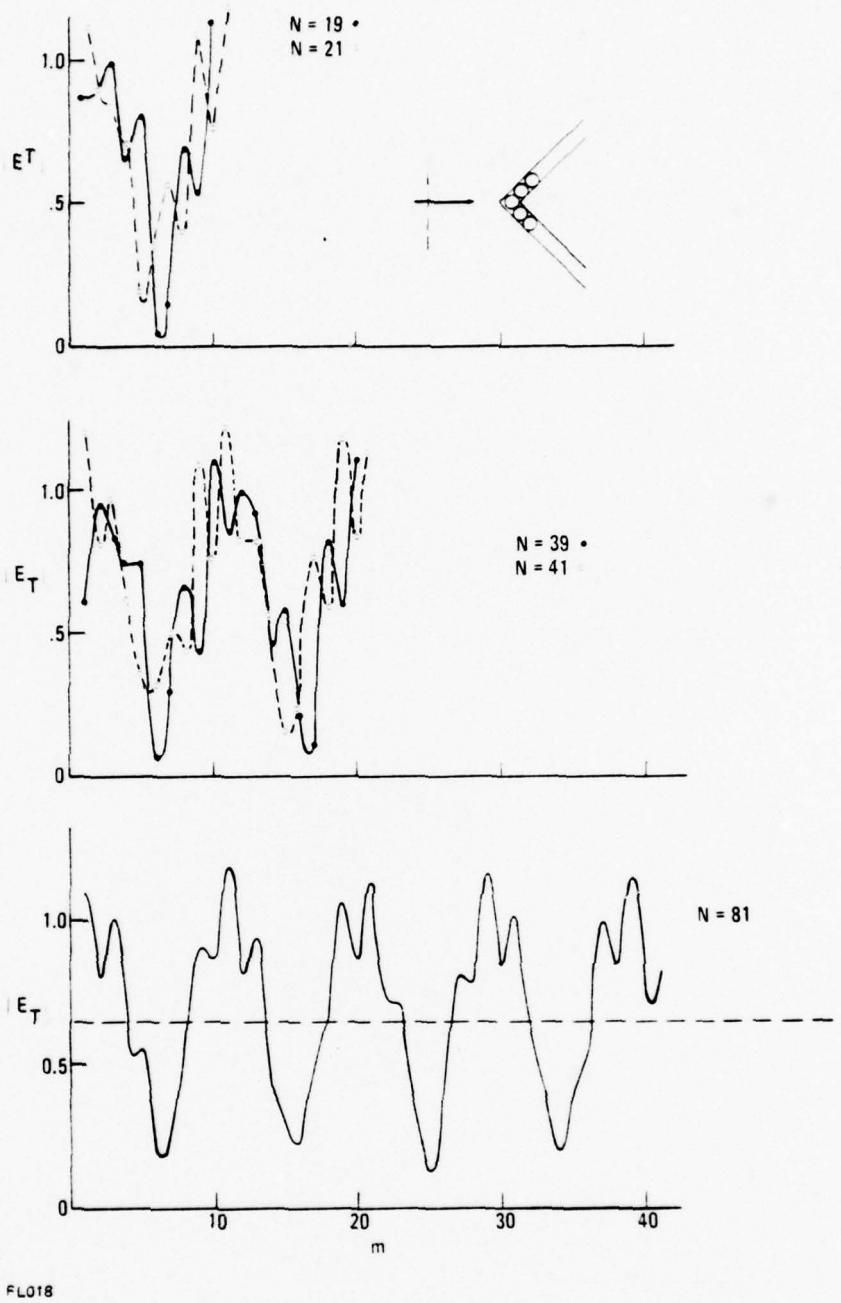

Figure 3-22. Total Field Amplitude Inside Walls of 90° Wedge, $\rho = 0.25$ in., a = 0.143 in., $\kappa = 2.6$ at $\lambda = 1.259$ in. for Axial Incidence. The horizontal dashed line gives the value for an infinitely broad slab.

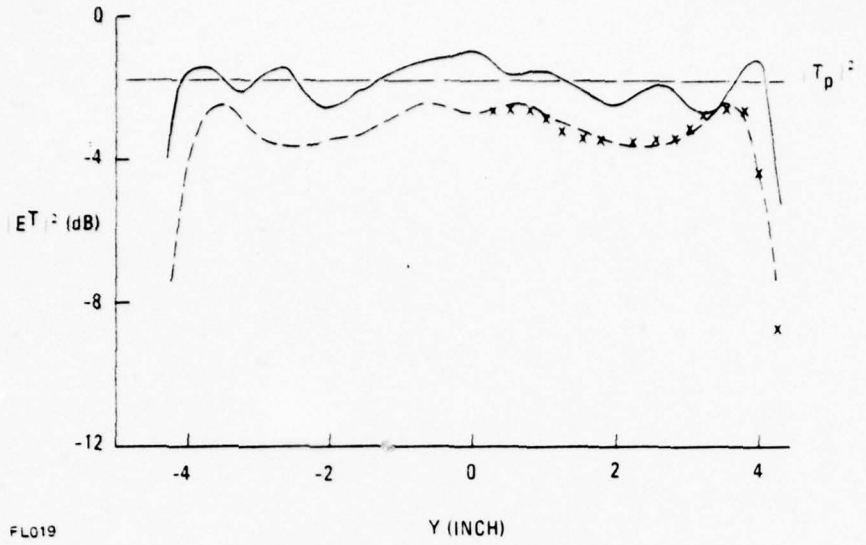

Figure 3-23. Intensity Behind Hollow Dielectric Wedge, $\kappa = 2.6$, With 10 in. x 18 in. Walls, Thicknesses 0.226 in. and 0.232 in. at $\lambda = 1.259$ in. Measured with dipole probe (—). Calculated at x = 4.48 in., for N = 81 (°), for N = 83 (x), a = 0.143 in., $\rho = 0.25$ in.

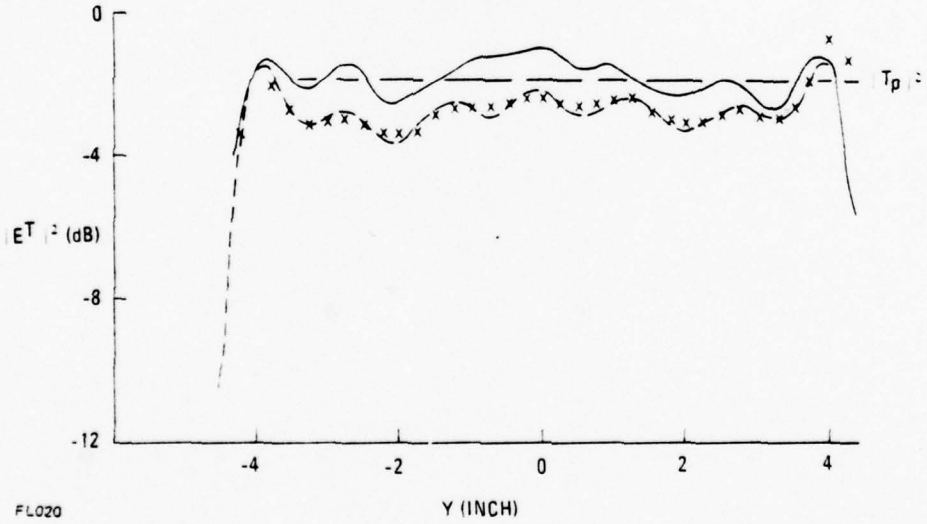

Figure 3-24. Intensity Behind Hollow Dielectric Wedge, $\kappa = 2.6$, With 18 in. x 18 in. Walls, Thicknesses 0.226 in. and 0.232 in. at $\lambda = 1.259$ in. Measured with dipole probe (—). Calculated at x = 4.48 in. (x), at x = 4.61 in. (°). $\rho = 0.25$ in., a = 0.136 in. for y < 0, a = 0.130 in. for y > 0. N = 81.

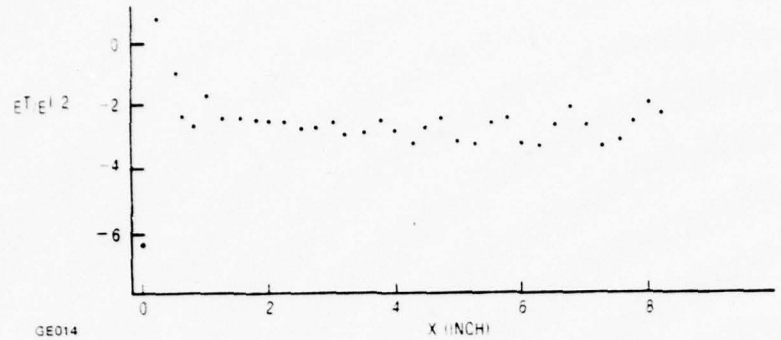

Figure 3-25. Power transmittance on symmetry plane of hollow wedge. Computed with a = 0.143 in.; ρ = 0.25 in.

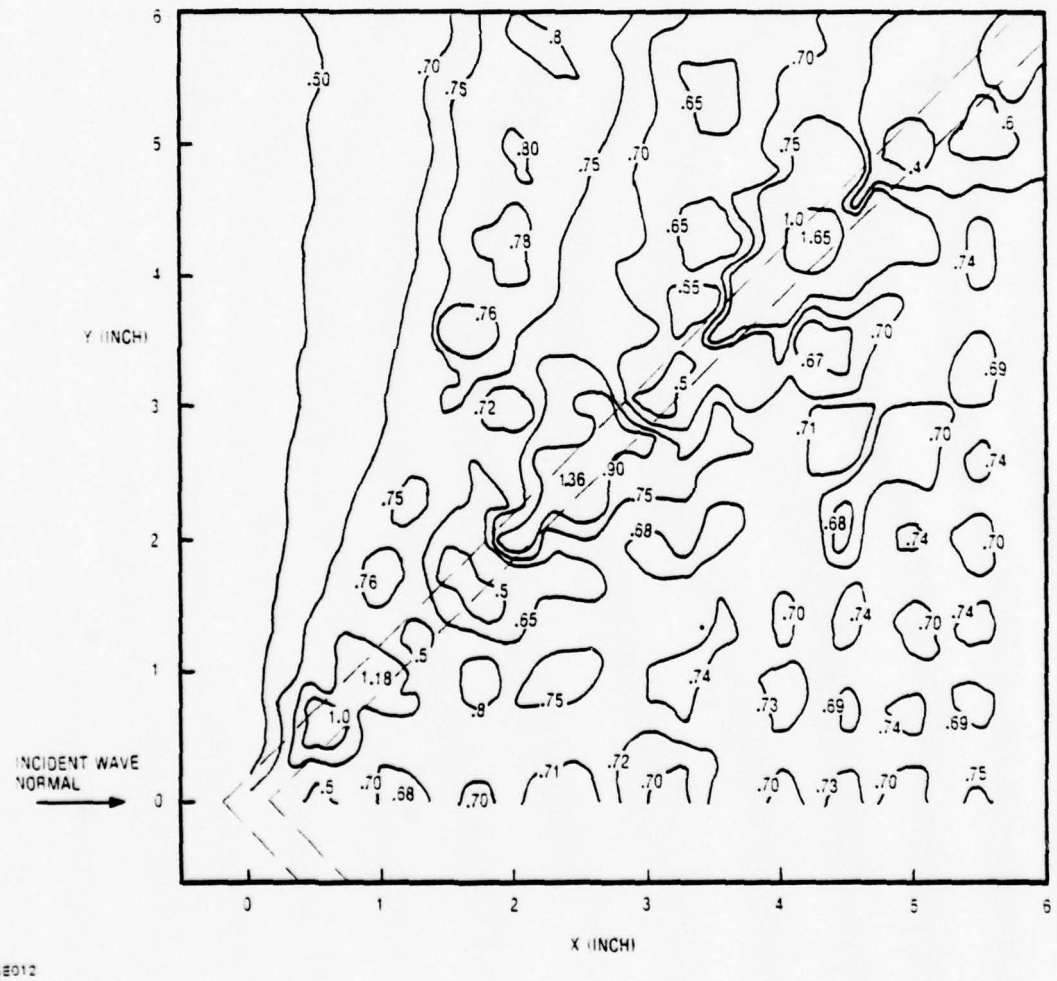

Figure 3-26. Scattered field magnitude near hollow wedge. Shown in 6 x 6 in. region near the vertex. Computed for a = 1.36, ρ = 0.25 in.

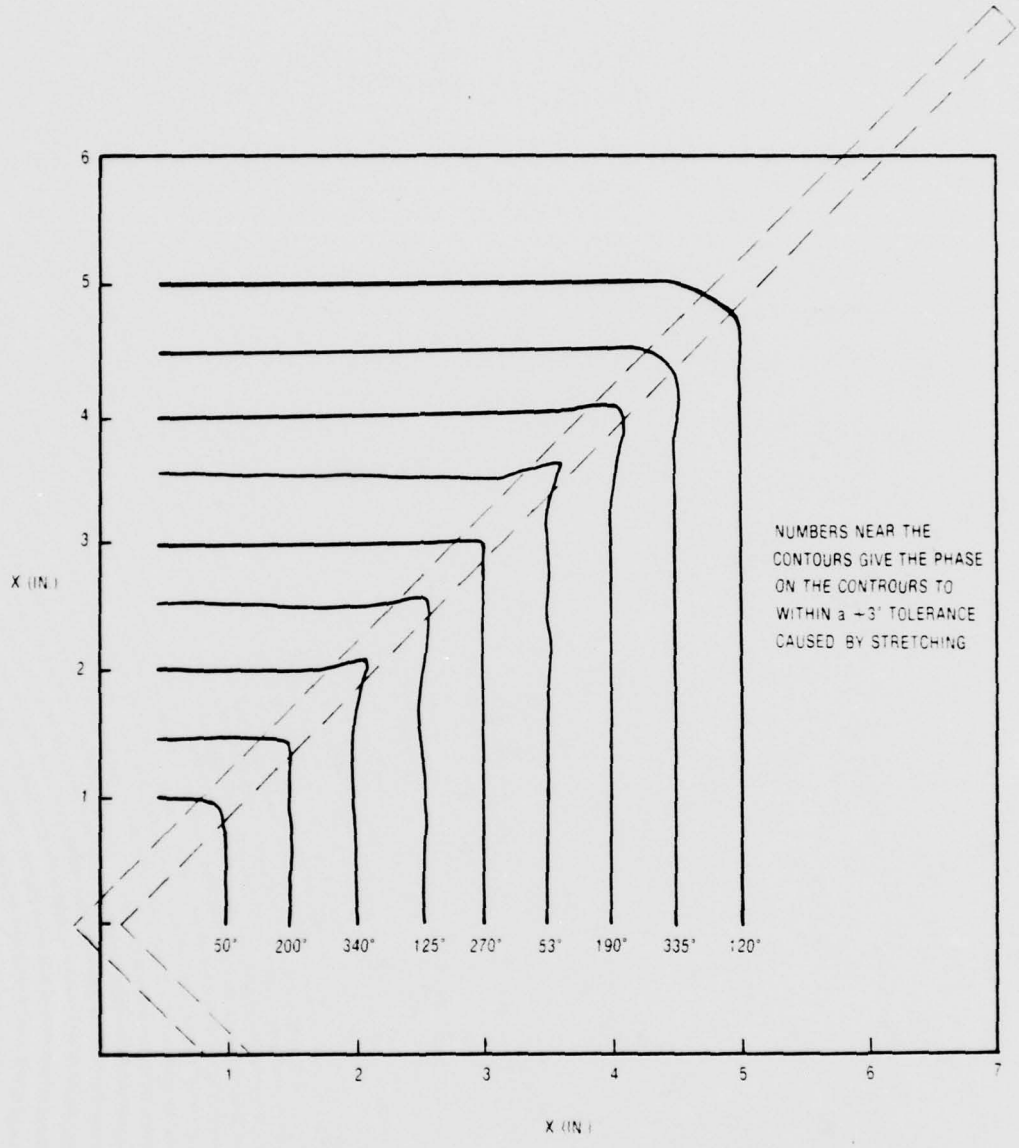

GE013

Figure 3-27. Equiphase contours of E^S for hollow wedge.

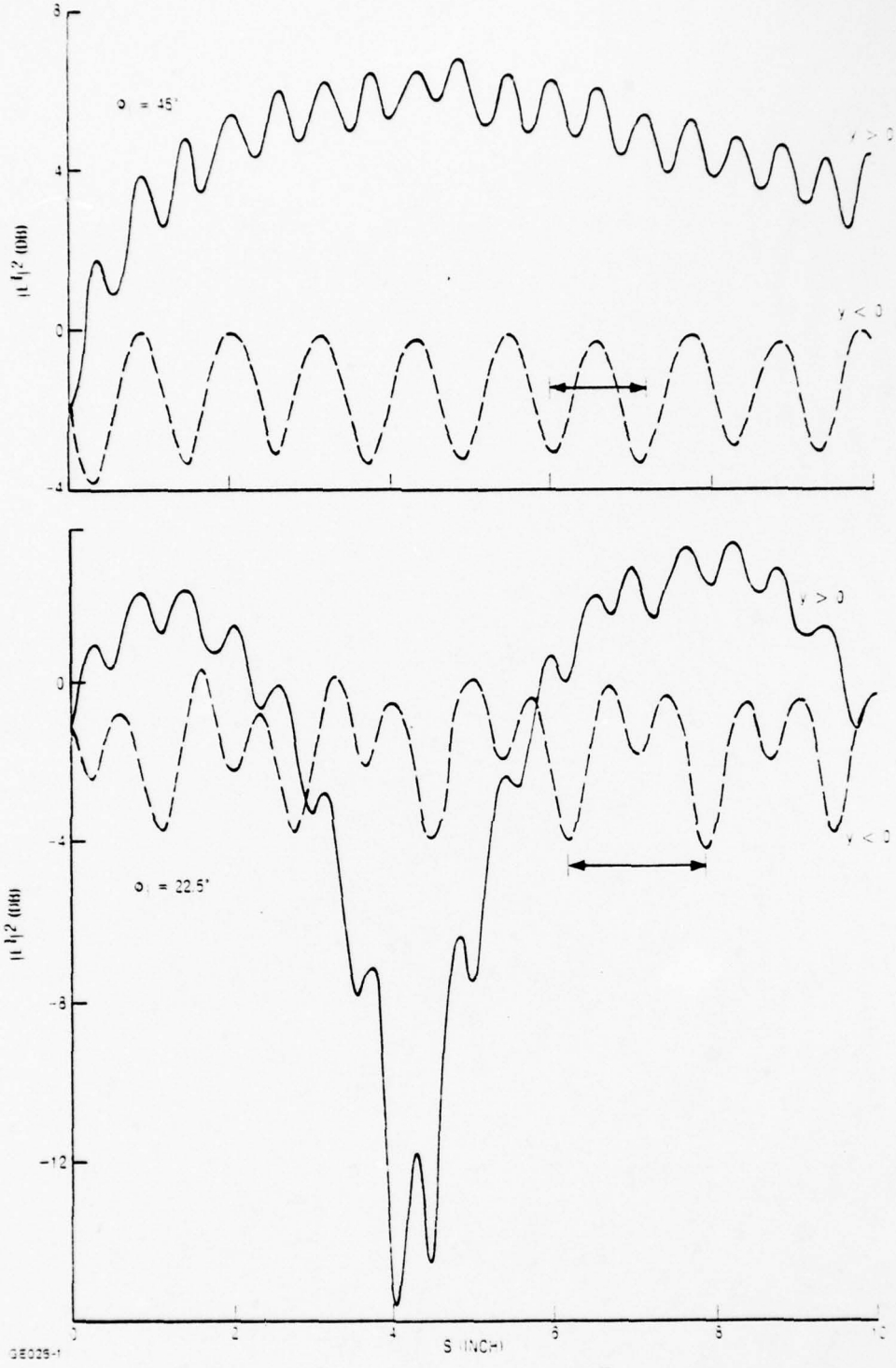

Figure 3-28a. Computed intensity of total field $|E^T|^2$ inside hollow 90° wedge with 1/8 in. walls. Dielectric constant 2.6, N = 161, λ = 1.259 in. The arrows show spacings of nulls predicted by Equation 3-7. See Figure 3-7 for definition of ϕ_i. (Sheet 1 of 2)

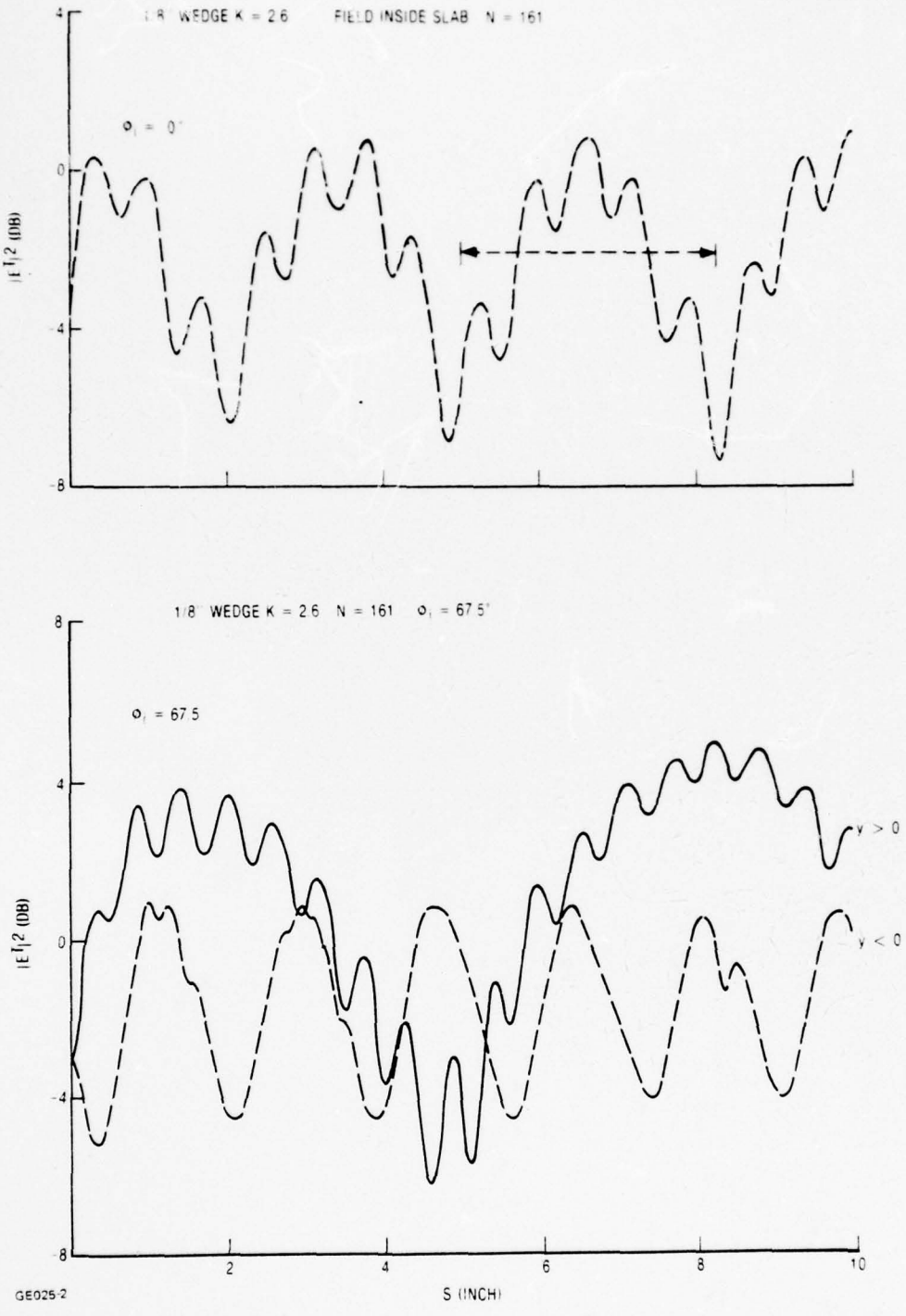

Figure 3-28b. Computed intensity of total field $|E^T|^2$ inside hollow 90° wedge with 1/8 in. walls. Dielectric constant 2.6, N = 161, λ = 1.259 in. The arrows show spacings of nulls predicted by Equation 3-7. See Figure 3-7 for definition of ϕ_i. (Sheet 2 of 2)

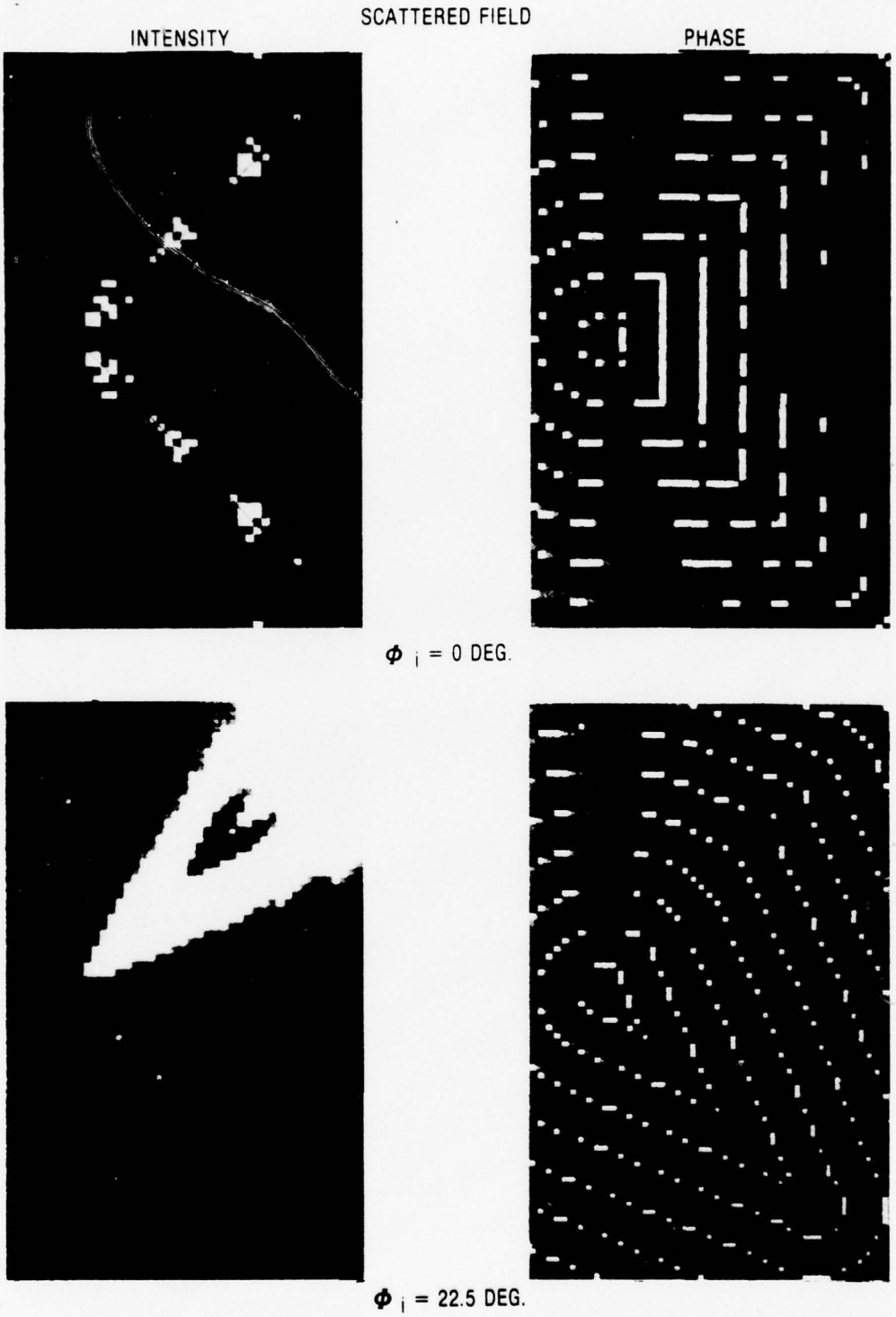

Figure 3-29. Intensity and phase near 90° dielectric wedge; sidewall lengths 10 in.; thickness 0.125 in.

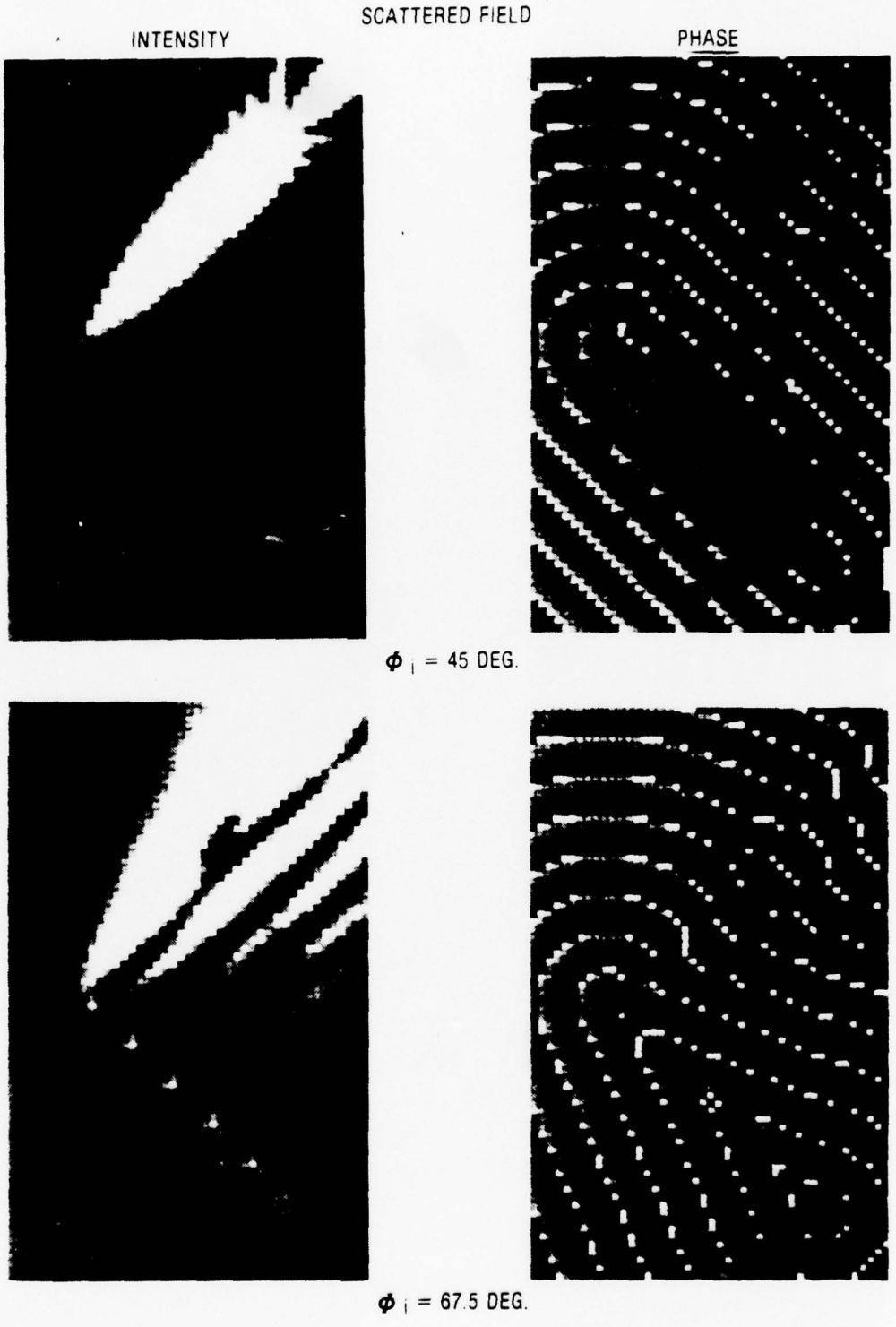

Figure 3-30. Intensity and phase near 90° dielectric wedge; sidewall lengths

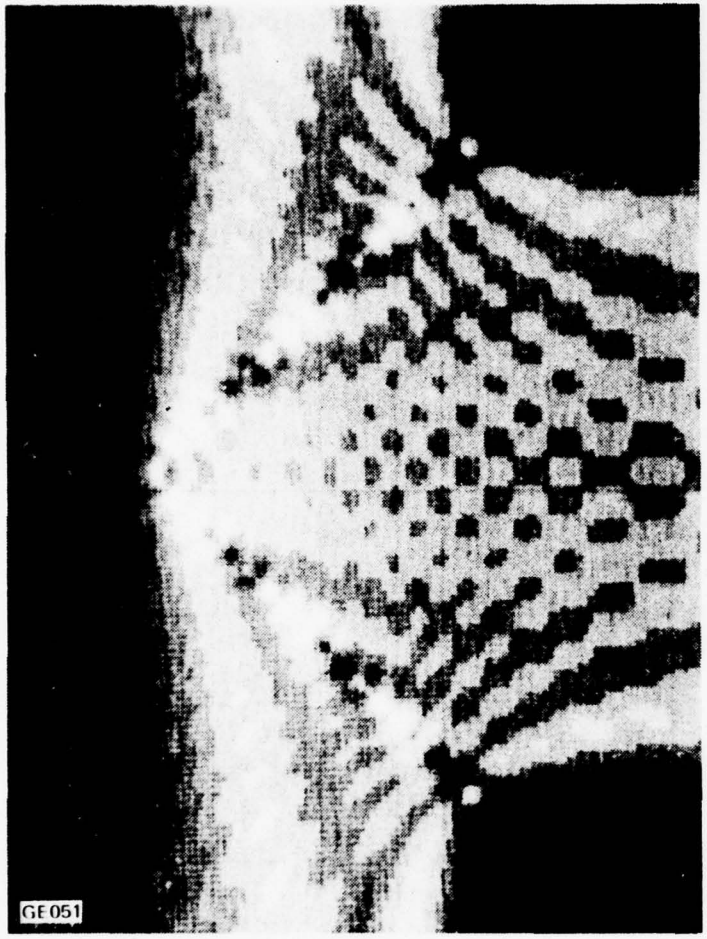

Figure 3-31. Intensity Near Hollow Wedge for 22 Grey Levels; $\phi_i = 0°$

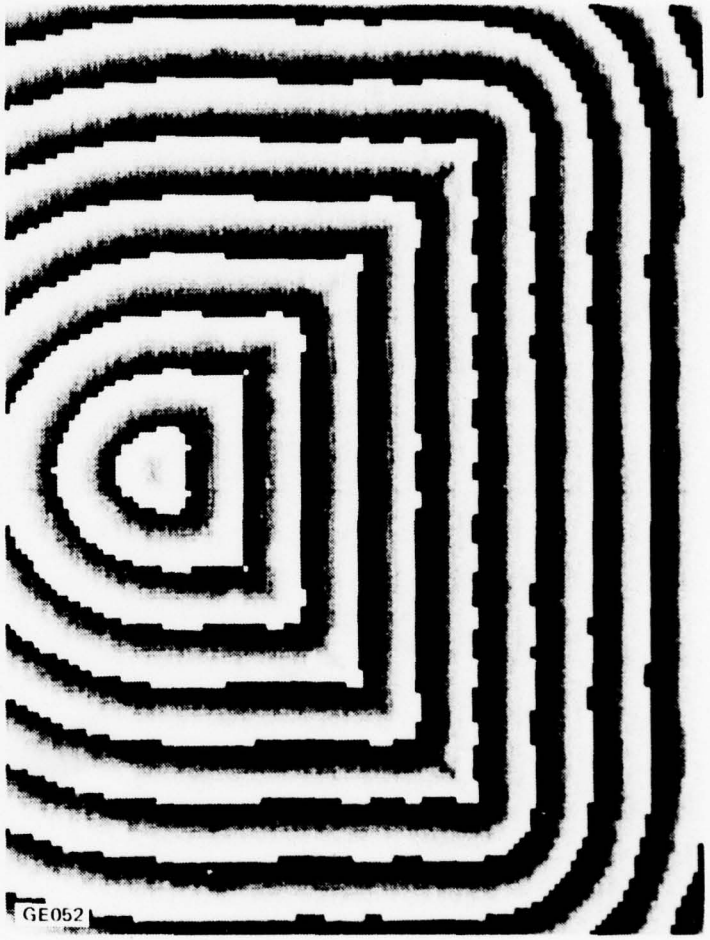

Figure 3-32. Phase Near Hollow Wedge for 22 Grey Levels; $\phi_i = 0°$

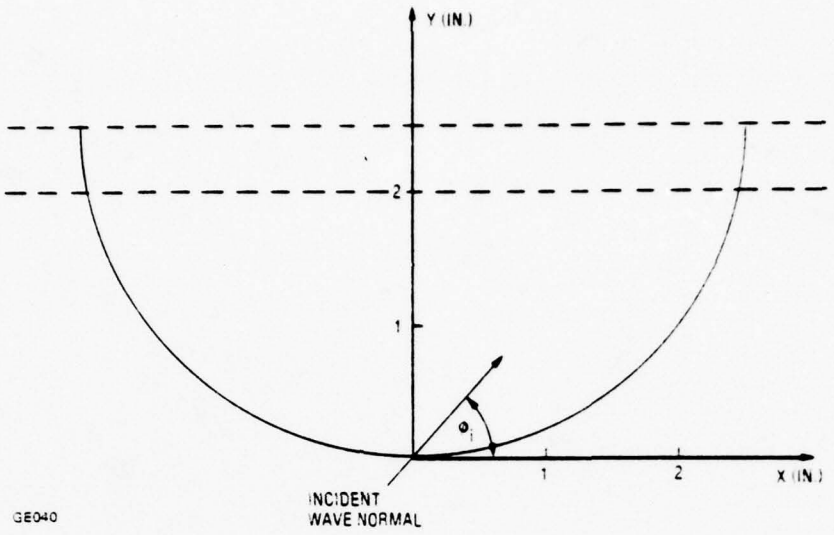

Figure 3-33. Geometry for Hemi-Cylinder and Incident Wave Directions

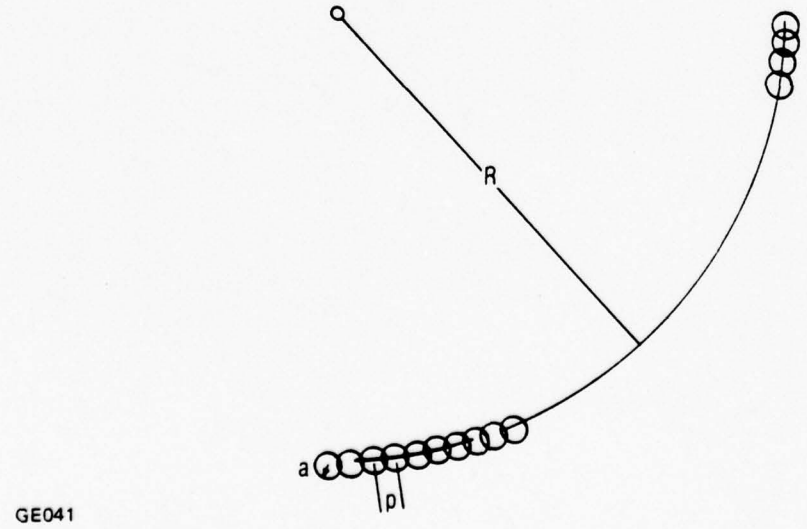

Figure 3-34. Approximating a Hollow Hemi-Cylinder with a Set of Solid Cylinders

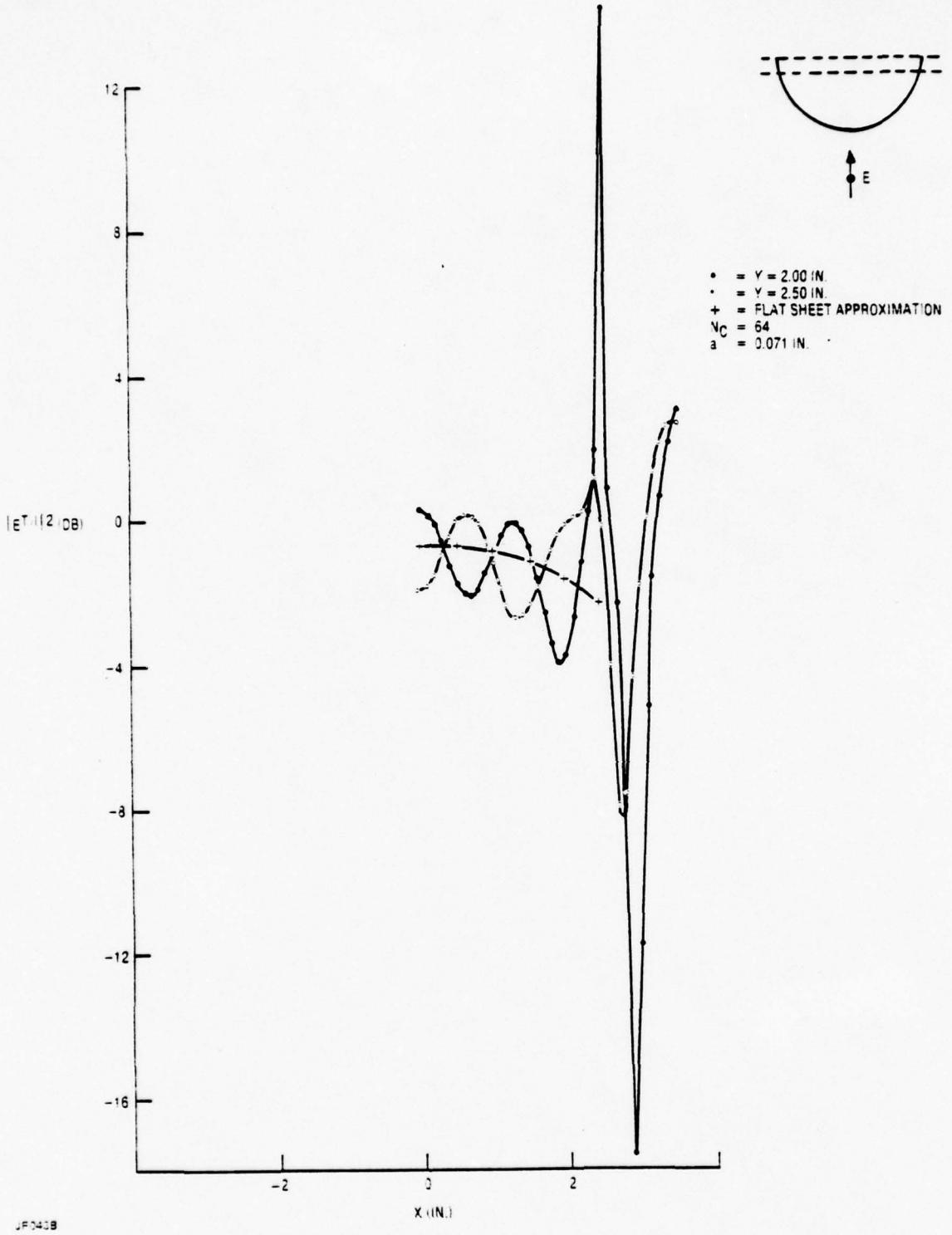

Figure 3-35. Power transmittance of dielectric hemi-cylinder for $\theta_i = 90°$. Inner diameter 4.87 in.; thickness 0.125 in.; wavelength 1.259 in. Moment method calculations. Data are symmetric about X = 0.

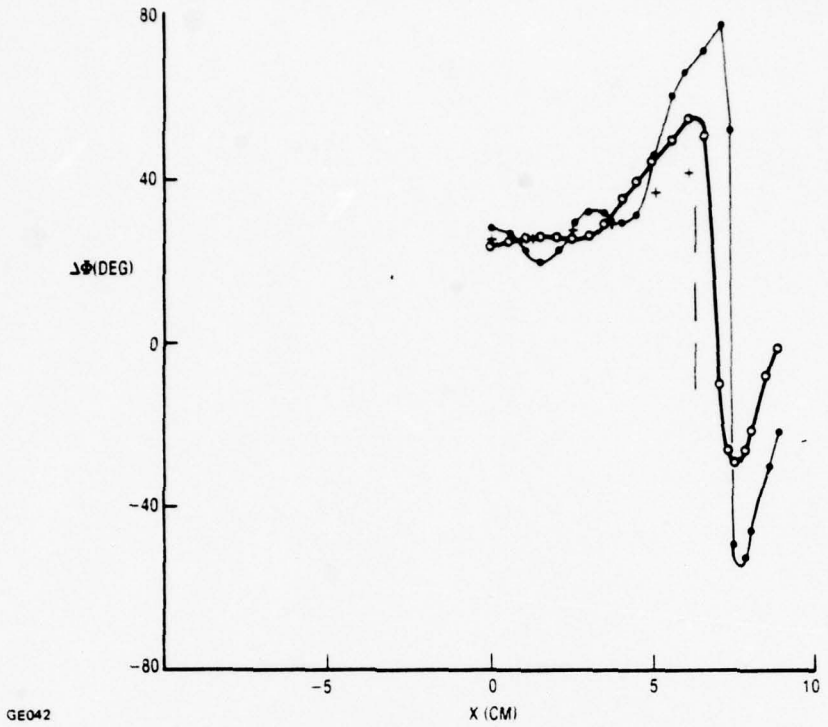

Figure 3-36. Phase delay corresponding to Figure 3-35.

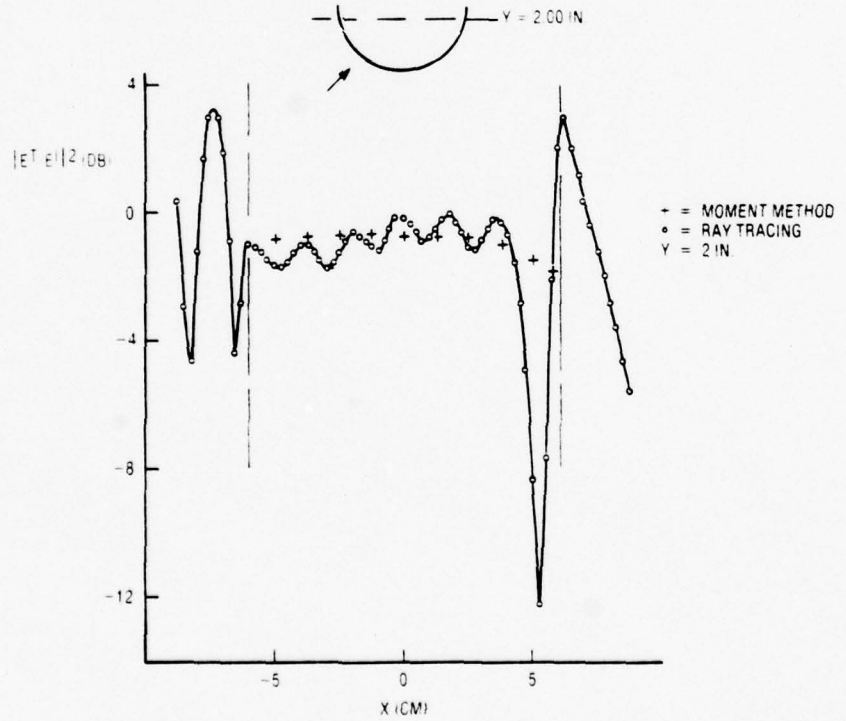

Figure 3-37. Power transmittance for the conditions of Figure 3-35, except with $\phi_i = 45°$. The dashed lines show the co-ordinates of the inner radome surface.

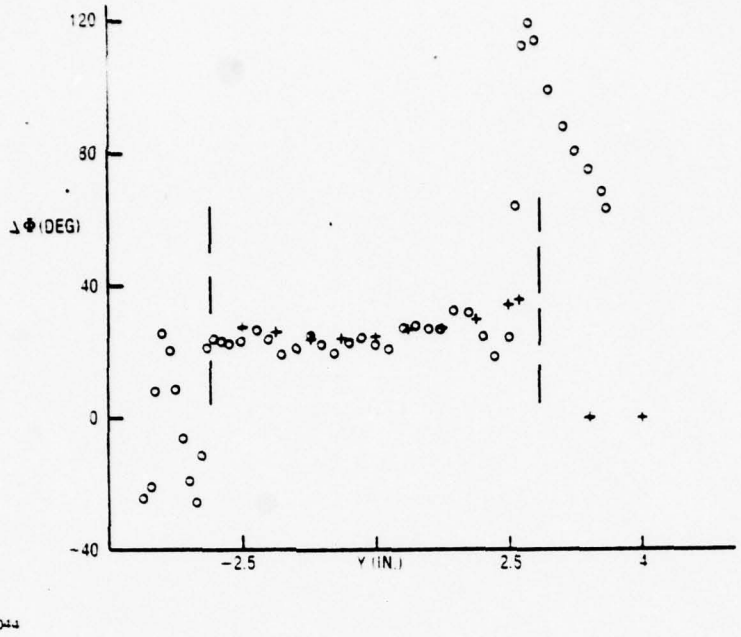

Figure 3-38. Phase for Figure 3-37.

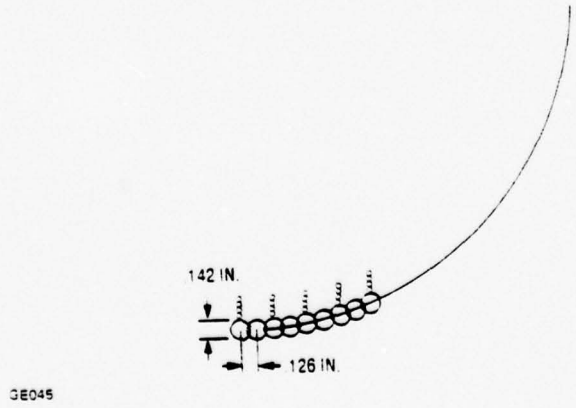

Figure 3-39. Approximating cylinders for a hollow hemi-cylinder with gratings.

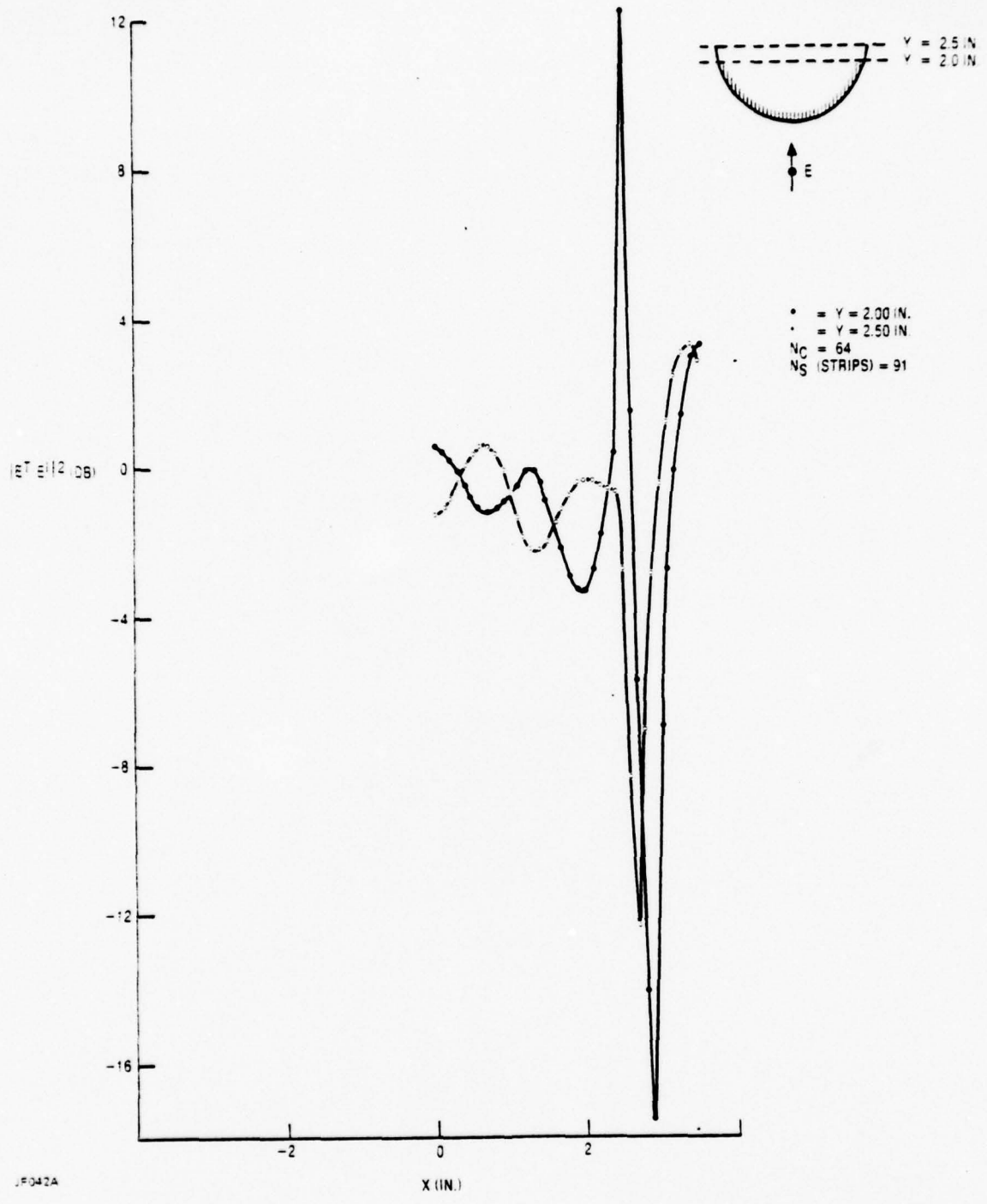

Figure 3-40. Power transmittance of hemi-cylinder with dielectric strips for $\phi_i = 90°$. Inner diameter of hemi-cylinder 12.38 cm; thickness 0.32 cm; wavelength 3.2 cm. Computed by moment method. Radii of approximating cylinders were 0.180 and 0.086 cm. Data are symmetric about X = 0.

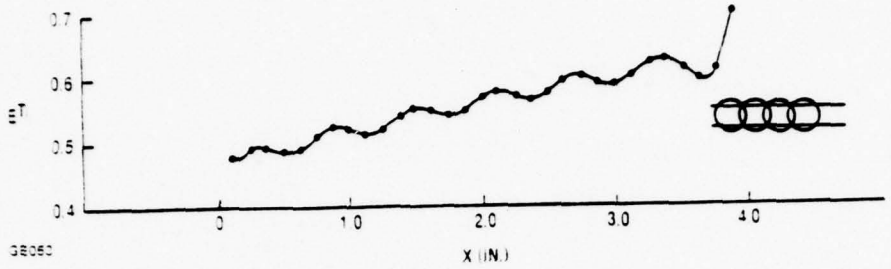

Figure 3-41. $|E^T|$ Inside Dielectric Slab. Thickness 0.126 in., at y = 0, for N = 32, a = 0.071 in., ρ = 0.126 in.

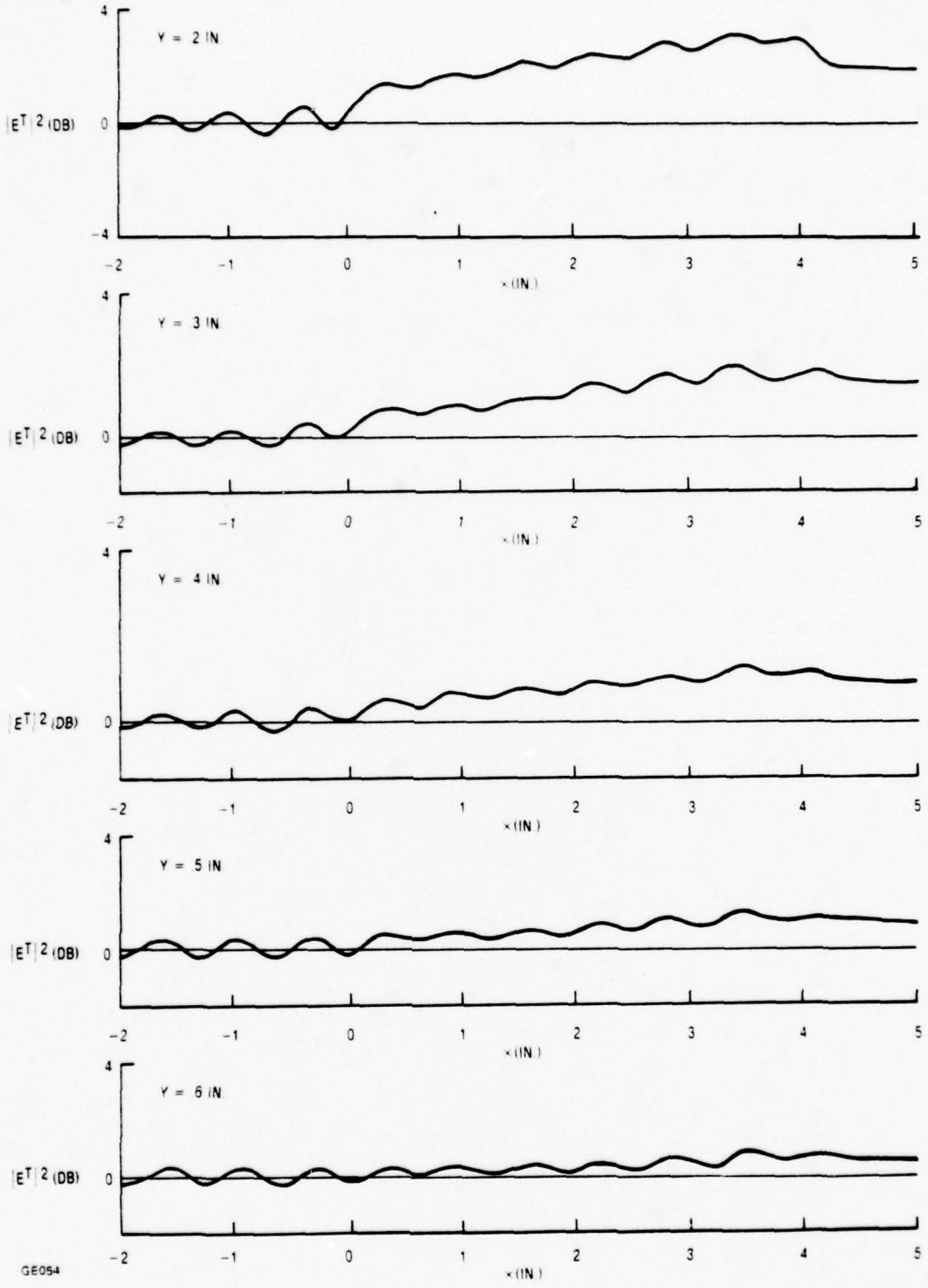

Figure 3-42. $|E^T/E^I|^2$ for .235 in. Slab. Parallel Polarization, 10.4 cm Long

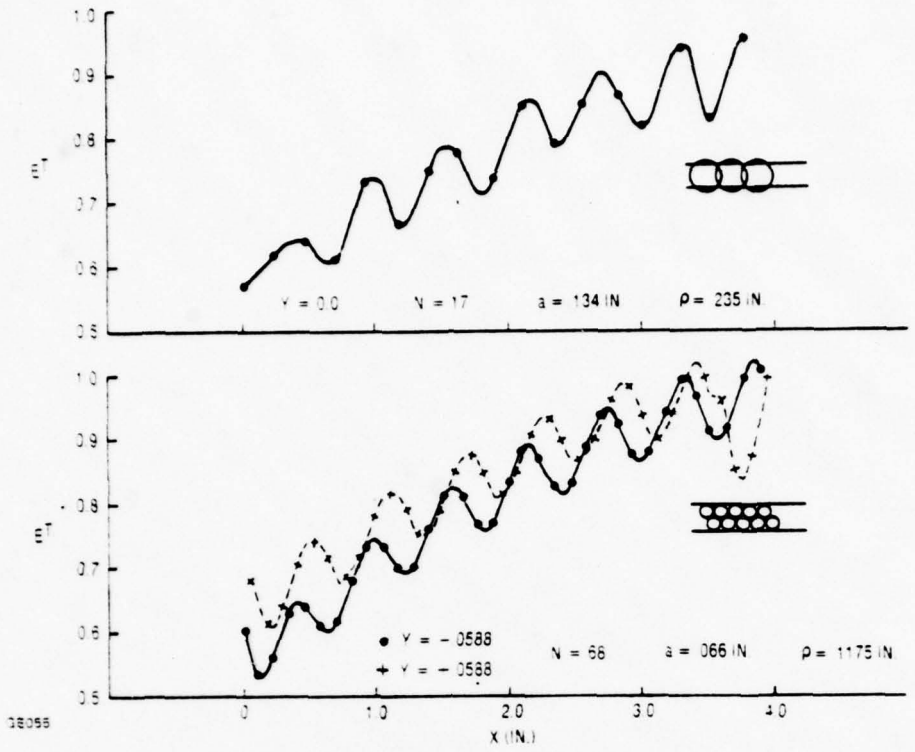

Figure 3-43. $|E^T|$ Inside Dielectric Slab, Thickness .235 in. for Grazing Incidence. Parallel Polarization

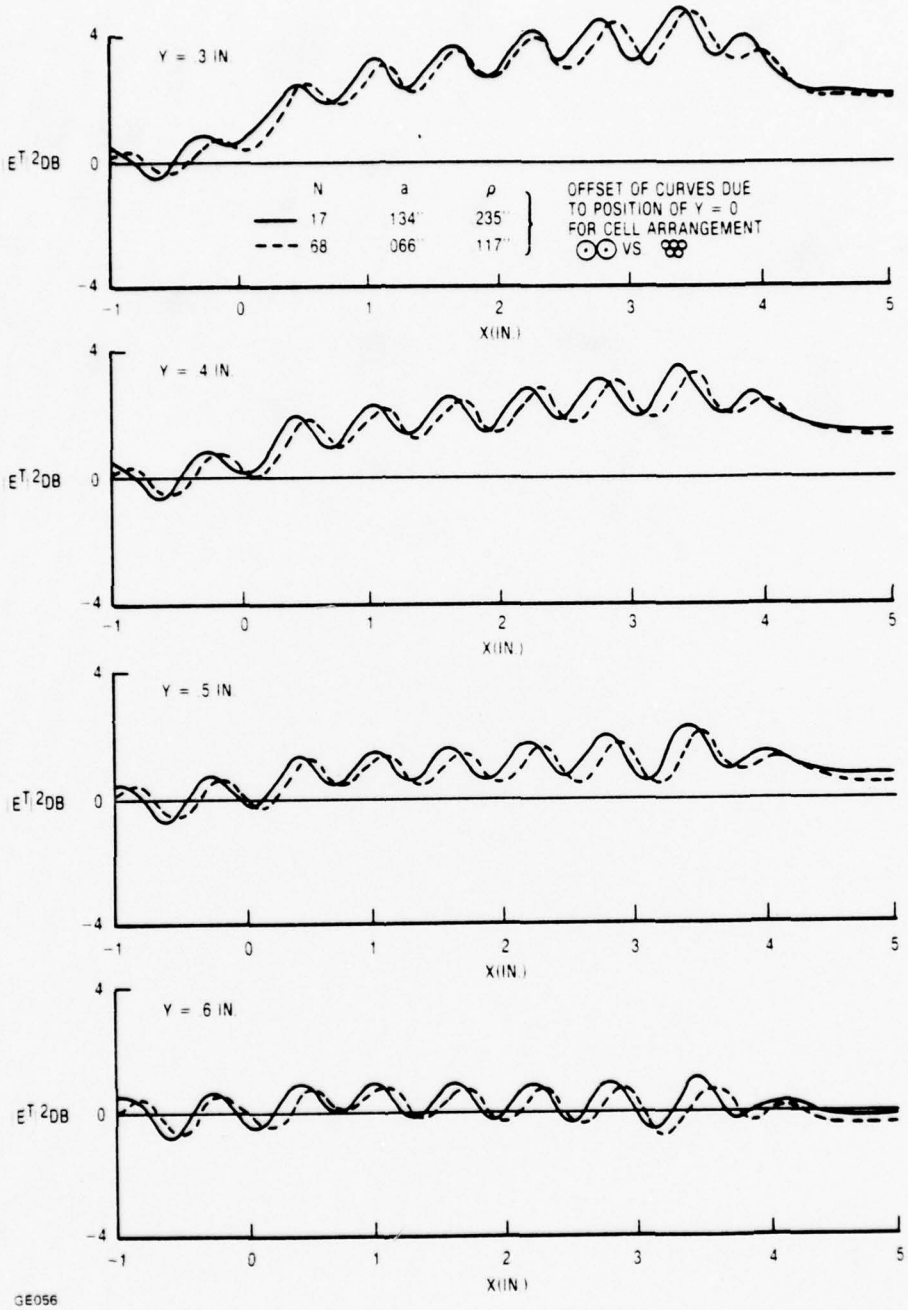

Figure 3-44. Computed Intensity Near Dielectric Slab for Grazing Incidence, Parallel Polarization

4. MEASUREMENT

4.1 APPARATUS AND PROCEDURE

The apparatus is sketched in Figure 4-1. It consisted of a signal generator, a network analyzer, and a probe positioner. The probe antenna was either a half-wave dipole or an open end waveguide. The transmitting antenna was 20' from the probe so the field was approximately that of a plane wave. Measurements were made by moving the probe on the paths shown in Figure 2-2, with the dielectric scatterer present and then after the scatterer was removed. The difference between measured values of intensity is the power transmittance, which is normalized to the free space value; similarly the difference in phase values is the argument of the complex-valued transmittance.

4.2 RESULTS FOR PERPENDICULAR POLARIZATION

4.2.1 SLAB: 4 IN WIDTH; NORMAL INCIDENCE

For the slab with thickness 0.24 in., measured values of $|E^T/E^I|^2$ are shown in Figures 3-6 and 3-7 for two, distinct probes. One was an open-end waveguide. The other was a half-wave dipole. The measured data depend on the probe, but the differences between the results decrease with distance from the slab. For either probe, the discrepancies between measured and computed results are smaller in Figure 3-7 than in Figure 3-6. This result is reasonable since N was larger for Figure 3-7 than for 3-6. In Figure 3-7 discrepancies are smaller for the dipole probe. Therefore the dipole seems to be preferable to the open-end waveguide.

Figure 3-8 shows $|E^T/E^I|^2$ measured with a dipole probe for a slab with thickness 0.125 in.

4.2.2 SLAB: 10 IN. WIDE, NORMAL INCIDENCE

Figure 3-10 shows $|E^T/E^I|^2$ shows measured values for a slab thickness 0.25 in. The dipole probe gives the variation of the computed curves, and discrepancies are smaller for the dipole than for the waveguide except in the center of the graphs for $Y = 0.75\lambda$.

Figure 3-11 shows $|E^T/E^I|^2$ of the thinner slab, 0.125 in. thick, for a dipole probe. Discrepancies are very small. The reason is that the small values of a gave accurate computations. In contrast for Figure 3-10 N was small, and a was too large for accurate computations. This approximation is further discussed in Section 5.

4.2.3 SLAB WITH DIELECTRIC STRIPS

Measured values of $|E^T/E^I|^2$ are shown in Figure 3-13. The discrepancies increase with increasing X. The discrepancies are small (less than 0.4 dB) for $x > 0$, but as much as 0.8 dB for $x < 0$. This asymmetry results because the computations were done with the strips at positions asymmetric about the slab center. In Figure 3-13 the strips near the fifteenth more nearly represent the experimental model than do those near the first, which is on the side $x < 0$.

4.2.4 SLAB, 45° INCIDENCE

Figure 3-17 shows measured values of intensity $|E^T/E^I|^2$ on a transverse path, which had a fixed x value in Figure 2-2b. The transition between the directly illuminated and shadowed regions is apparent. The discrepancies are large in the shadowed region because the cells were large; with a = 0.143 in. This case corresponds to that in Figure 3-10; only the incidence angle and probing paths differ.

4.2.5 SLAB, GRAZING INCIDENCE

For grazing incidence, Figure 2-2c, Figure 4-2 shows $|E^T/E^I|^2$ measured at three values of the spacing between the probe (a half-wave dipole) and the slab. The spacings were 0.1, 0.2, and 0.3 in. Figure 4-3 shows $|E^T/E^I|^2$ at spacing 0.4 in. Notice that spacing is less than the y co-ordinate by half the slab thickness. For example, spacing 0.4 in. corresponds to Y equal 0.525 in. Because of tolerances in slab thickness the value of y may be in error by as much as 0.01 in.

4.2.6 HOLLOW WEDGE, 0.23 IN. THICK, AXIAL INCIDENCE

Figure 3-23 (and 3-24) show $|E^T/E^I|^2$ for a hollow, 90° wedge formed of two orthogonal slabs. Wall thicknesses were 0.226" and 0.232".

4.3 RESULTS FOR PARALLEL POLARIZATION

The probe influences measurements for parallel polarization when it is near a slab because the field has a considerable evanescent constituent. That is, the guided wave amplitude decreases rapidly with increasing distance from the slab. Since the probe spans a finite width, it averages the field. Moreover, the response to the field depends on probe orientation for an unbalanced probe. For example, Figure 4-4 shows measured values of $|E^T|^2$ for two orientations of the dipole probe near a slab, thickness 0.125 in. The orientations are approximately symmetric, with the probe merely inverted, yet the data differ considerably. Figure 4-5 shows results for a slab 0.60 cm thick. The average of the $|E^T|^2$ values for the two orientations is shown in Figure 4-6.

The data in Figure 4-6a should be compared with those in Figure 3-42. The value of Y we expect is the sum of half the probe width (0.313 in.), half the slab thickness (0.063 in.), and probe clearance from the slab (0.040). The sum is 0.416 in. In Figure 3-42 the graphs 1.02 and 1.27 cm resemble the average of the measured data in Figure 4-6.

Figure 4-7 shows deep minima near a slab 0.432 in. thick.

Figure 4-1. Apparatus for Transmittance Measurements. NA represents a network analyzer, G a generator, T a transmitting antenna, and P a probe antenna

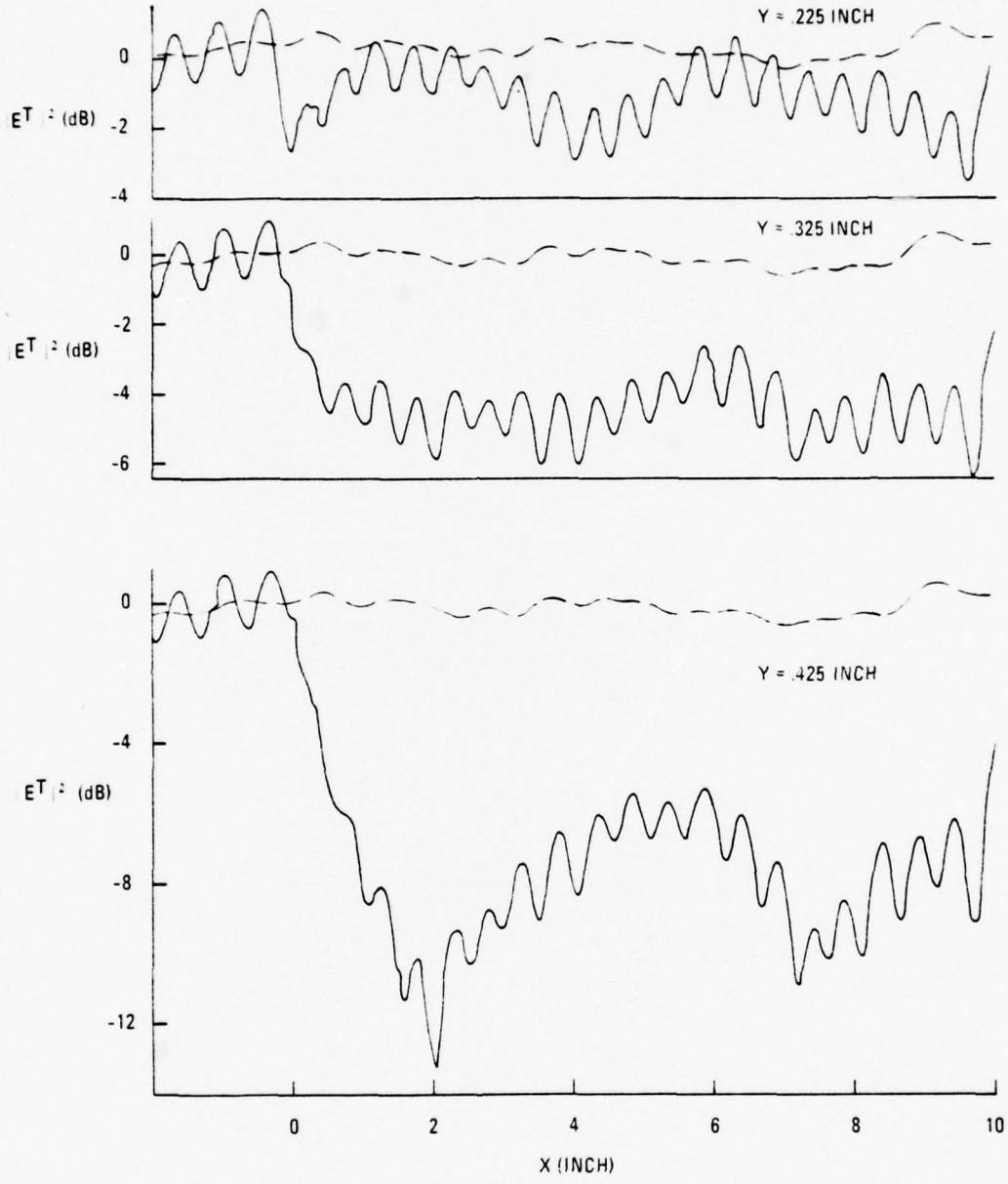

Figure 4-2. Intensity Near Slab for Grazing Incidence.
Dielectric constant 2.6; thickness 0.23 in.
The dashed line is the level without the slab.

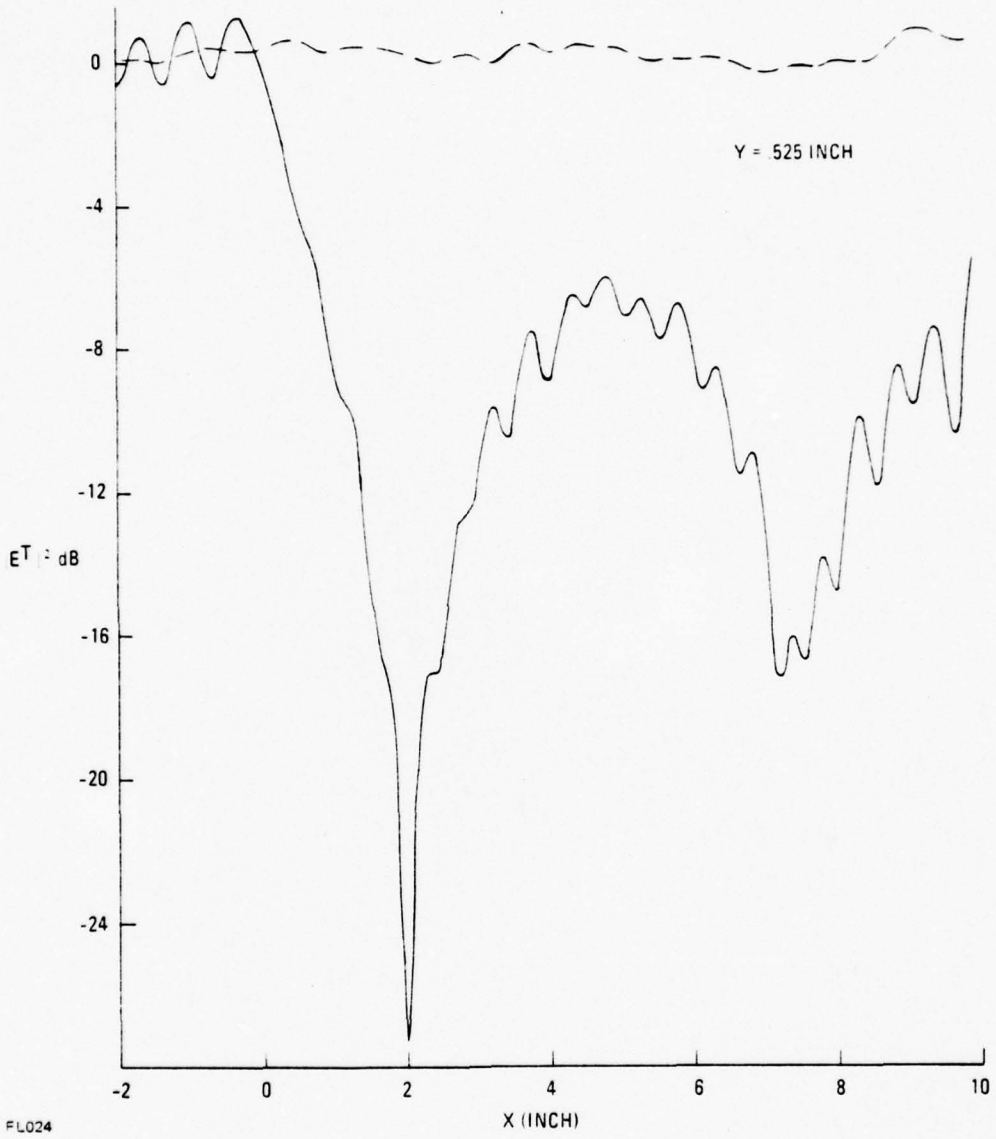

Figure 4-3. Measured Intensity Near Slab at Y = 0.525 in. The dashed curve is the level without slab thickness .23 in.

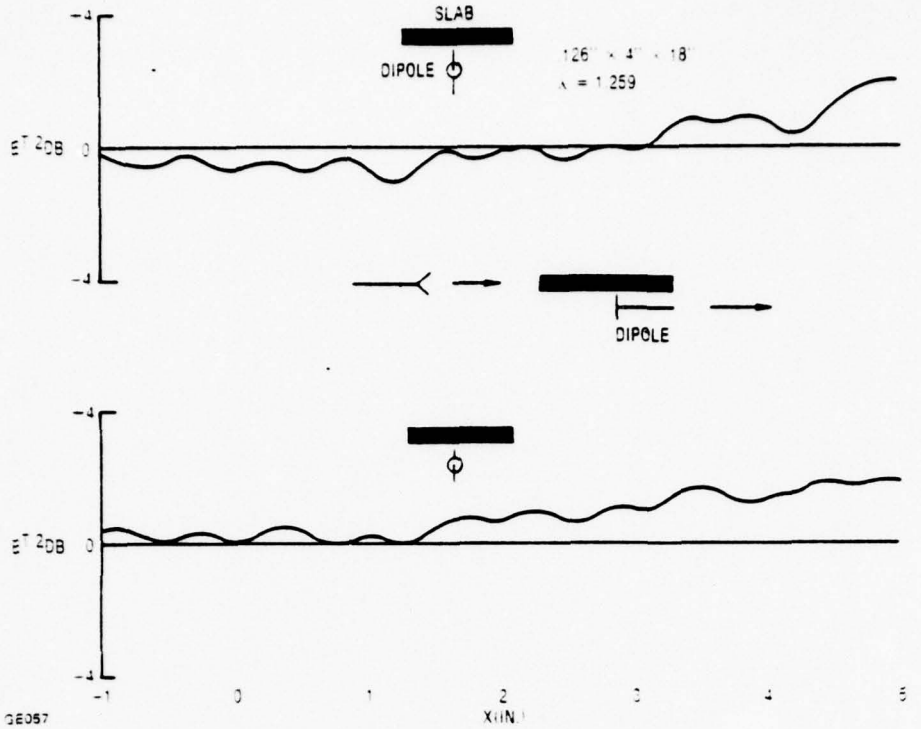

Figure 4-4. Measured Intensity Near Dielectric Slab for Grazing Incidence, Parallel Polarization

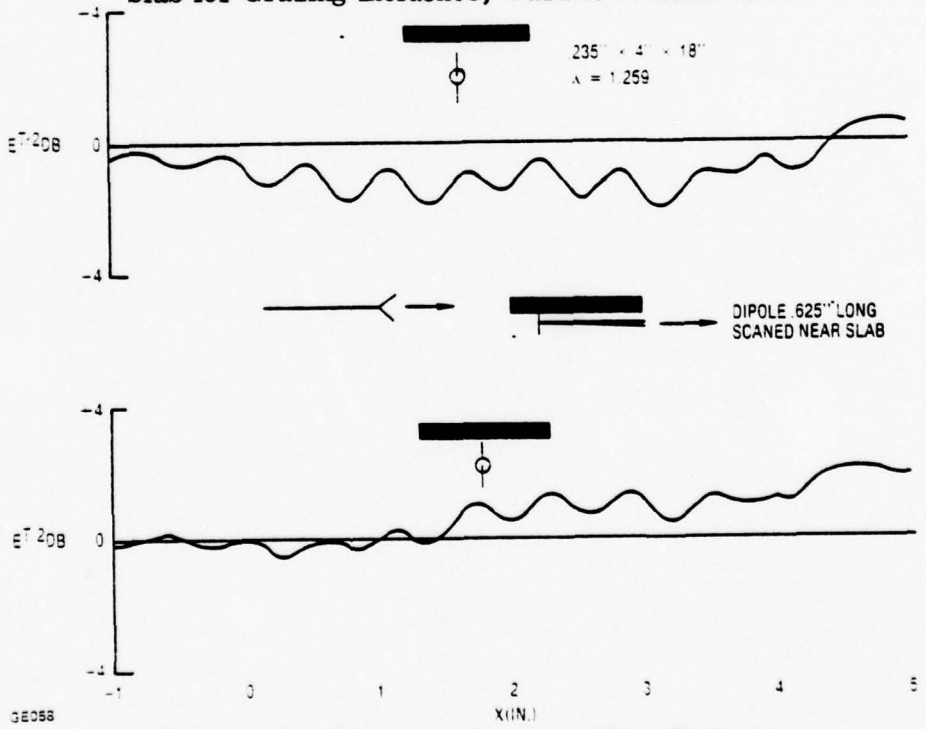

Figure 4-5. Measured Intensity Near Dielectric Slab for Grazing Incidence, Horizontal Polarization

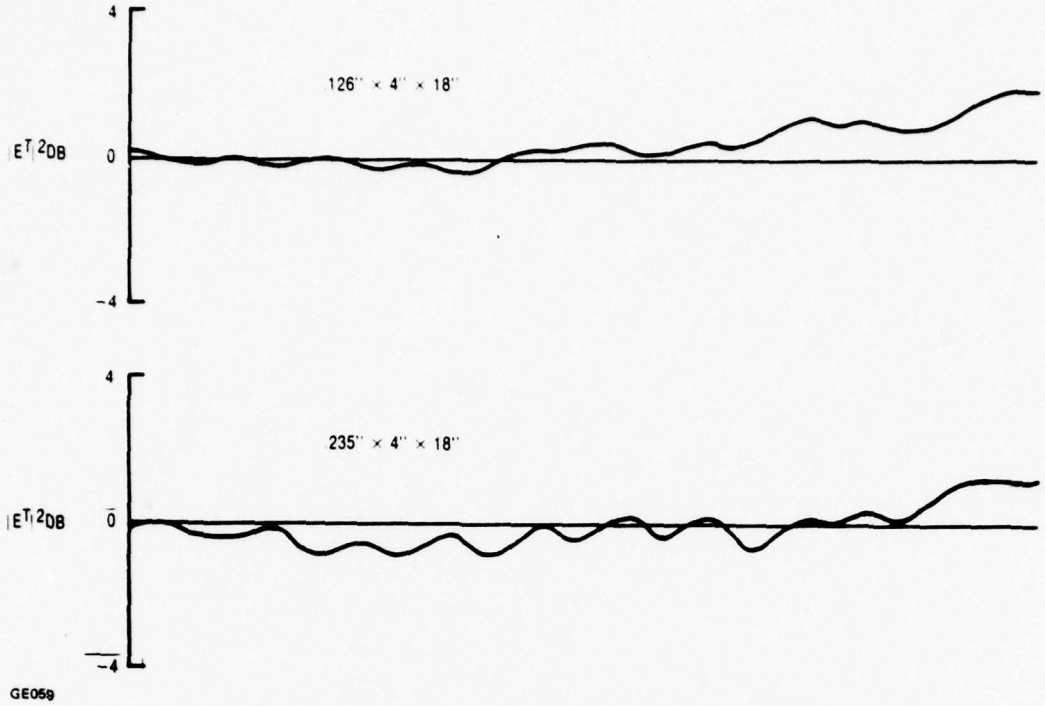

Figure 4-6. Averaged Measured $|E^T|^2$

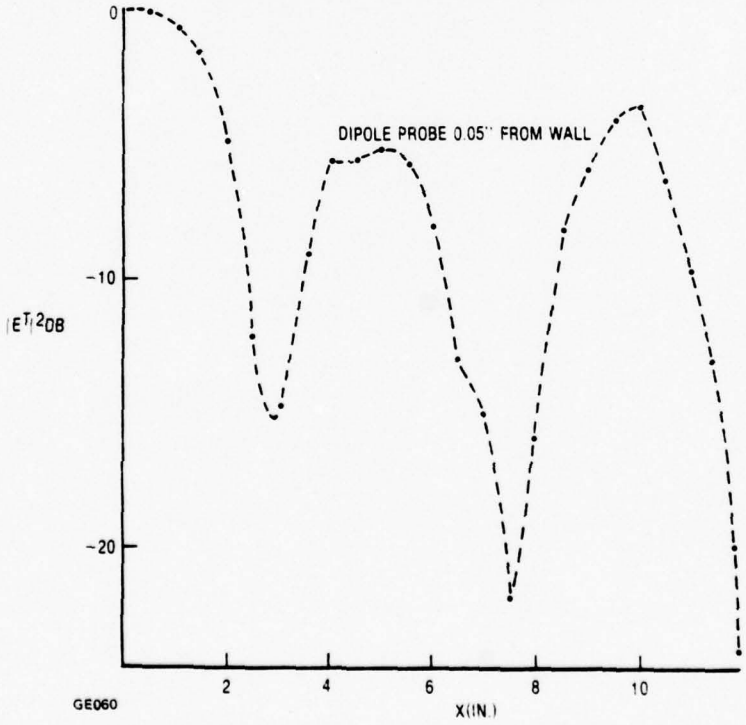

Figure 4-7. Measured Power Transmittance Near 0.432 in. Thick Dielectric Slab for Grazing Incidence, Polarization Parallel

5. DISCUSSION

5.1 PERPENDICULAR POLARIZATION

5.1.1 SLABS, NORMAL INCIDENCE; INTERNAL FIELDS AND AN ACCURACY CRITERION

The values of $|E^T|$ shown in Figures 3-4 and 3-5 oscillate as functions of X. The values on the slab-midplane vary about the value for an infinitely broad sheet. The exact, analytical value for the mid-plane is

$$E_\rho^T = t_{01}\,(1-r_{10}\exp kd')^{-1}(\exp ikd'/2) \qquad (11)$$

where t_{01} and r_{10} are Fresnel interface transmittance and reflectances, and d' is $d\sqrt{\kappa-\sin^2 i}$, where d is thickness, and i is incidence angle. The moment method results also depend on y, as expected.

In the following discussion, we use the term "discrepancy" for the difference between measured and computed values.

Figure 3-6 shows $|E^T/E^I|^2$ measured once with an open-end waveguide and once with a half-wave dipole. The shapes of the curves for the dipole more closely resemble the computed values than do those for the waveguide. Discrepancies are also smaller except near the center of the curve for $Y = 0.75\lambda$. The discrepancies are large for either antenna.

The large discrepancies in Figure 3-6 result because the cell size, 0.114λ, violates the assumption that the field be constant in each cell. For a smaller cell size, 0.042λ, Figure 3-7 shows smaller discrepancies. In this figure, discrepancies are larger for $Y = 0.5\lambda$ than for $Y = 1.0\lambda$; apparently, the probes disturb the field more when they are nearer the slab. Note too that discrepancies are smaller for the dipole probe. Therefore the dipole seems better for perpendicular polarization. Apparently it has better spatial resolution than the open-end waveguide.

Figure 3-8 shows small discrepancies for a thinner slab. In this case calculations were done with a equal 0.715 in. Again, discrepancies are larger for the probe nearer the slab.

Now we consider a quantitative accuracy criterion for cell radii. We plot the maximum discrepancy, in a graph of $|E^T/E^I|^2$ for each y as a function of optical path length ϕ_o corresponding to cell diameter; that is,

$$\phi_o = 360^\circ (2a\sqrt{\kappa}/\lambda) \qquad (12)$$

Consider the data measured with the dipole and shown in Figures 3-6, 3-7, and 3-8. The values of ϕ_o for the respective figures are 132°, 49°, and 66°. Figure 5-1 shows maximum discrepancies plotted as functions of ϕ_o for two distances between probe and slab mid-plane.

Figure 5-1 suggests that smaller ϕ_o correspond to smaller discrepancies. For the data points corresponding to the two smaller values of ϕ_o, and for which discrepancy magnitudes are relatively small, the data for Y = $\lambda/2$ seem more accurate than those for Y = λ . Apparently the probe affects the measuremements more when it is closer to the slab than it does at larger distances.

We conclude that maximum discrepancies of reasonable magnitude (approximately 10% in power) can be obtained with ϕ_o equal 66°. This value results with a = 0.042 λ for κ equal 2.6.

5.1.2 SLAB: 25.4 CM WIDTH, NORMAL INCIDENCE

For the thicker slab, Figure 3-10 shows that the dipole gives somewhat better agreement with the shape of the computed curve than does the waveguide. Discrepancies are large for either probe. For the thinner slab, discrepancies are small for the dipole probe; see Figure 3-11. The maximum discrepancies are plotted in Figure 5-2 as functions of ϕ_o. By comparing Figures 5-1 and 5-2, we see discrepancies are smaller for the broader slab. If we choose 0.6 dB as a criterion then for ϕ_o = 66°, this discrepancy can be achieved at Y = $\lambda/2$ for the broader slab; however, this value requires Y be greater, approximately λ.

5.1.3 GUIDED WAVES: AN INDEPENDENT MODEL; EXAMPLES FOR NORMAL INCIDENCE

The measured and computed graphs show oscillations. Examples are numerous. The internal field magnitudes in Figures 3-4 and 3-5 vary about the value for a sheet of infinite width. At normal incidence, Figure 3-11 shows small, but distinct oscillations, and Figures 3-16 and 3-21 show wide variations. These oscillations occur for both measured and computed values. Their explanation is interference of guided waves and plane waves that propagate into and through the slabs and wedges. This interpretation follows from the following model.

For notational simplicity let us start with external fields and consider a slab. Suppose the total field in the region shadowed by a slab consists of a plane wave and a slab-guided wave. The field is

$$E^T = Ae^{-vd} e^{ik_g s} + T_\perp e^{ik_o s \cos\alpha}, \tag{13}$$

where s is path length along the slab or $(X^2 + Y^2)^{1/2}$, k_o is $2\pi / \lambda_o$, with λ_o the free space wavelength, A is the guided wave amplitude and $T_\perp$ the complex-valued plane wave transmittance of a sheet with properties of the slab. The symbol d represents normal distance from the slab, k_g is the propagation constant of the slab, and v is the decay factor. The angle α is the angle between the plane of the slab and the incident wave normal. The solution of the boundary value problem for slab guided waves gives u and v.

From symmetry we assume the guided wave to have even variation about the midplane. To determine k_g and v we must solve

$$(ua/2) \tan(ua/2) = (va/2) \tag{14}$$

where a is slab thickness, and

$$u^2 = \kappa k_o^2 - k_g^2, \tag{15}$$

with the condition

$$u^2 + v^2 = k_o^2 (\kappa - 1) \tag{16}$$

To determine u and v, graph the left side of Equation 14 as a function of ua/2 and find the intersection with the circle of Equation 15, when written as $(ua/2)^2 + (va/2)^2 = k_o^2 a^2 (\kappa-1)/4$. For example, Figure 5-3 shows a graph for 2a = 0.125 in.; λ_o = 1.259 in., and $\kappa = 2.6$. We find ua/2 is 0.118π so k_g is

$$k_g = 1.73 \quad /\text{in.} \tag{17}$$

and

$$v = 0.72 \quad /\text{in.} \tag{18}$$

As a check on our model, we shall examine spacings of fringes as in Figure 3-16. The condition for minima spacings is that the two terms on the right side of Eqatuion 13 differ by 2π in distance s. Thus

$$\delta s = 2\pi/(k_g - k_o \cos\alpha) \tag{19}$$

To derive spacings inside the slab we must utilize the internal refracted and reflected waves. For the orientation in Figure 3-1, assume the field is

$$E^T = T_d e^{i(k_x x + k_y y)} + R_d e^{i(k_x x - k_y y)} + A e^{ik_g x} \tag{20}$$

where T_d and R_d are transmittance and reflectance for the internal waves (assumed plane), $k_x = \sqrt{\kappa} k_o \sin r$, $k_y = \sqrt{\kappa k_o} \cos r$, where r is the angle of refraction. Consider the midplane, so y is zero. Recall Snell's law, that $\sqrt{\kappa} \sin r = \sin i$, with i the incidence angle, and $i + \alpha = \pi/2$. Thus, Equation 20 gives

$$E^T = (T_d + R_d) e^{ik_o x \cos\alpha} + A e^{ik_g x} \tag{21}$$

Equation 21 has the form of Equation 13 so fringe spacings inside and outside are equal. This result is physically intuitive.

The model assumed for Equation 13 was one plane wave and one guided; but this model is too simple. For example, consider normal incidence on a slab, Figure 2-2a. The oscillations of E^T inside the slab can be explained by interference of guided waves and plane waves, but from symmetry we must assume two guided waves that travel in opposite directions. We also assume the internal field contains plane waves, which for normal incidence are

$$E_p = T_d e^{ik_o \sqrt{\kappa}\, y} + R_d e^{-ik_o \sqrt{\kappa}\, y}, \tag{22}$$

For simplicity let y = 0 so

$$E_p = T_d + R_d = S \tag{23}$$

Thus the internal field is

$$E^T = S + Ae^{ik_g x} + Be^{-ik_g x} , \tag{24}$$

and intensity is

$$|E^T|^2 = C + 2\,AB\cos\left[2k_g x + (\alpha-\beta)\right] + 2|AS|\cos\left[k_g x + (\alpha-\sigma)\right] + 2\,|BS|\cos\left[k_g x + (\sigma-\beta)\right] \tag{25}$$

where $C = |A|^2 + B^2 + |S|^2$, and α, β and σ contain phase of A, B and S.

From Equation 25 we obtain fringe spacings.

$$\Delta S = \pi/k_g , \tag{26}$$

and

$$\Delta S = 2\pi/k_g . \tag{27}$$

For the data in Figures 3-4 and 3-5, we have $k_g = 1.96\ \pi$/inch. Therefore ΔS from Equation 27 is 1.02 in. This value agrees closely with the 1.00 in. spacings computed by the moment method; see Figures 3-4 and 3-5. This spacing was determined by averaging the spacings in the graph. Note that Equation 27 results from the terms with S as a factor. Physically, this spacing corresponds to interference of plane and guided waves. The smaller spacing, Equation 26, arises from interference of oppositely directed waves. This smaller period is apparently absent. The reasons are that A and B are smaller than S, and that we have two terms with period $2\pi/k_g$ in Equation 27.

The mechanism for guided wave excitation may be the larger phase shift over the slab and negligible phase shift away from the slab. The wave is refracted into the slab near the ends; that is, the wavefront is bent into the slab near its ends.

For the broader slab we have more spacings than in Figure 3-4. Figure 3-9 shows spacings from moment method calculations to be 1.0 in. for the 1/4 in. thickness and 1.14 in. for the 1/8 in. thickness. From Equation 27 we have 1.02 in. as stated above for 1/4 in. thickness ($k_g = 1.96\ \pi$ /inch) and 1.18 in. for 1/8 in. thickness ($k_g = 1.70\ \pi$ /inch). The agreement between the moment method and Equation 27 is good.

Now consider external fields in Figures 3-10 and 3-11. It is clear that the moment method agrees with measurement for the thinner slab (Figure 3-11); for Figure 3-10 discrepancies are large because a was large.

Equation 27 also gives predictions that agree with measurement. For the 1/4 in. thickness, Equation 27 gives ΔS as 1.02 in.; the average spacing of 8 measured fringes in Figure 3-10 is 1.0 in. For the 1/8 in. thickness, Equation 27 gives ΔS as 1.18 in.; the average spacing of 7 measured fringes in Figure 3-11 is 1.14 in.

It is significant that fringe spacings depend on slab thickness. We can imagine a simple model in which the slab edges scattered free space type rays. In this case, no thickness dependence would exist. Moreover, the fringe spacing would be given by the intensity arising from an expression such as

$$E = Ae^{ik_o x} + Be^{-ik_o x} + Te^{ik_o y} \tag{28}$$

where for emphasis k_o is the free space propagation constant. From Equation 28 we obtain periods

$$\Delta S = \pi / k_o \tag{29}$$

and

$$\Delta S = 2\pi / k_o \tag{30}$$

From Equation 30 the spacing is λ or 1.259 in. This value exceeds the 1.14 in. value for 1/4 in. thickness and the 1.0 in. value for the 1/8 in. thickness.

We conclude edge diffracted rays are absent, but that guided waves exist and they might be considered to arise from refraction at the edges. We would call these guided rays in a geometric diffraction theory context. Guided waves also correspond to the rapid

decrease of the amplitude of the oscillations with distance in Figures 3-10 and 3-11; these slabs were relatively broad with widths 8 wavelengths. For the narrower slabs, the rapid oscillations of $|E^T/E^I|^2$ near the edges may suggest cylindrical waves from the edges, but we have not examined this possibility.

We emphasize that the model leading to Equation 13 is independent of the moment method yet it yields spacings that agree with those of the moment method. In addition, both the moment method results and Equation 13 yield results that agree with measured data. The evidence for guided waves is strong; we have identified a simple wave type, guided waves, in the numerical results from the moment method.

5.1.4 SLAB WITH DIELECTRIC STRIPS

The calculated values in Figure 3-14 show the strips increased transmittance averaged over the slab by approximately 1/3 dB. In Figure 3-13, discrepancies between measured and computed values are small for $X > 0$, but larger for negative X. These discrepancies arise because the experimental model differed from the computational. The strips locations for $X > 0$ agree for both models. In Figure 3-12 the configuration near the 15th strip is that of the experiment model; however, near the 1st the computational model differs from the experimental.

5.1.5 SLAB, 45 DEGREE INCIDENCE

The deep minima in Figure 3-15 can be explained by interference between guided waves and the internal plane waves. From Equation 19, with k_g equal $1.96\,\pi$/inch and α equal 45° we obtain $\Delta S = 2.39$ in. which agrees well with the 2.4 in. spacing in Figure 3-19. The shallower, more rapid oscillations apparently result from interference of the guided wave travelling in the positive X direction of Figure 3-1 and a smaller amplitude guided wave. The second term in Equation 25 represents such waves, and Equation 26 gives fringe spacing 0.51 in. This value agrees with the period of the rapid oscillations. Recall that cells are spaced by 0.25 in. and in Figure 3-15 the period corresponds to two cells. The out of phase behavior of the small oscillation produced by adding a cell also supports the interpretation of guided wave interference. The added phase on reflection is $2\,k_g\,\rho$ or $2(1.96\pi)/4 = 0.98\pi$. The phase is almost reversed by adding a cell.

Notice that the fringe pattern is established even for $N = 10$ which corresponds to slab length only 2 wavelengths.

The external field at distance 0.1 in. from the slab shows fringes with spacings closely approximating the 2.4 in. value predicted by Equation 19.

For the transverse path of Figure 2-2b, (Figure 3-17), the abrupt decrease for Y approximately 4 in. fits the notion of a guided wave.

5.1.6 FLAT SLAB, GRAZING INCIDENCE

Figure 3-19 shows that the computed internal field intensity exceeds the incident field intensity. The field magnitude $|E^T|$ reaches values almost twice that of $|E^I|$. Again we see the out-of-phase behavior produced by adding one cell. Figures 3-21 and 3-22 show that the field changes rapidly with perpendicular distance. By comparing Figures 3-20 and 3-21 with Figures 4-2 and 4-3 we see excellent agreement between measured results and those from the moment method. Notice in Figure 3-20 that the small rapid oscillations have period 0.5 in. in the region of the slab, 0 in. $\leq x \leq$ 10 in.; however, for $x > 0$ the period exceeds 0.6 in. Thus we have a free space reflected wave for $x < 0$ and interfering guided waves for $X > 0$.

5.1.7 HOLLOW WEDGE

The internal field, shown in Figure 3-22, for thickness 0.25 in. at axial incidence has oscillations like those of the slab, Figure 3-15. Again, we have interference between guided and free space plane waves. In Figure 3-22, the amplitude oscillates between 0.1 and 1.1, about the value 0.6 for the internal plane waves. Therefore, the guided wave amplitude is estimated at 0.5. This estimate also applies for the slab at 45° incidence; see Figure 3-15.

Figures 3-23 and 3-24 show that distinct thicknesses for the two walls of the wedge introduce small fluctuations into the field on the transverse plane. These fluctuations appear in the measured data.

The intensity $|E^T/E^I|^2$ on the symmetry plane, Figure 3-25, is influenced by waves that are scattered by the edges of the wedge. The edges at the far ends of the walls project to x = 7.1 in. in the co-ordinate system of Figure 2-2d, and a third edge is at the vertex. Assume three rays as in Figure 5-4. Let the fields of these three rays be a sum of three plane waves

$$E_e = T_p e^{ik_o x} + ae^{i(k_x x + k_y y)} + ae^{i(k_x x - k_y y)} \tag{31}$$

where k_x is $k_o \cos\phi$, k_y is $k_o \sin\phi$, and a is amplitude. On the plane Y = 0,

$$E_e = T_p e^{ik_o x} + 2ae^{ik_x x} \tag{32}$$

The intensity is

$$|E_e|^2 = |T_p|^2 + a^2 + 4|aT_p| \cos\left[(k-k_x)\, x + \tau - \alpha\right] \tag{33}$$

where τ is the phase of T_p and α that of a. From Equation 33 the period of $|E_e|^2$ is

$$(\delta x)_e = (1 - \cos\phi)^{-1} \tag{34}$$

which is plotted in Figure 5-5. For $\phi = 90°$, $(x)_e$ is λ. In Figure 3-25 the spacings for 5 in. $\leq x \leq$ 8 in. are approximately λ. Furthermore, fringe spacings increase with x, this trend is predicted by Equation 34, as shown in Figure 5-5. The variation for $x < 4$ in. are small suggesting the edge diffracted waves vary with position.

The field structure behind a wedge is evidently complicated, for it includes guided waves, edge-diffracted waves, and waves propagated through the walls. Figure 3-27 suggests that the field is approximately a plane wave because the equiphase surfaces are relatively flat. However, Figure 3-26 shows substantial intensity variation especially near the wedge walls.

Equation 19 predicts the fringe spacings for the hollow wedge with 0.125 in. thick walls. Table 5-1 summarizes the data. For the wedge, we have two values of incidence angle for each ϕ_i because we have two slabs forming the wedge; of course, for $\phi_i = 0°$, the two values of α are equal, 45°.

Table 5-1

Fringe Spacings From Equation 7 for $k_g = 1.73\,\pi$/inch, 2a = 0.125, k = 2.6, A = 1.259

ϕ_i (deg)	α upper slab (deg)	α lower slab (deg)	δ_s upper slab (inch)	δ_s lower slab (inch)
22.5	22.5	67.5	7.407	1.784
45	0	90	14.29	1.156
67.5	22.5	67.5	7.407	1.784
0	45	45	3.30	3.30

Figures 3-28a and b have these spacings superimposed on the moment method calculations of $|E^T|^2$. We observe agreement is excellent. We also see the rapid oscillations predicted by Equation 24.

To study the exponential decrease of guided waves we computed $|E^S|$. Figure 5-6 shows E^S on two lines, which intersect the x axis at 4 in. and at 5 in. The coordinate Y_A is parallel to the incident wavefront. In this case, $\phi_i = 45°$. The graphs show large values for Y_A greater than 2 in. or 3 in.; that is, near the upper wall of the wedge. The figure also shows Ae^{-vd}, where A is the value from the moment method calculation just outside the wall. The exponential decrease agrees fairly well with the moment method results. The approximately constant values of $|E^S|$ for Y less than approximately 2 in. arise mainly because of the lower half of the wedge.

Although the scattered field E^S is theoretically interesting, the total field E^T is directly observable and of interest for radomes. Therefore, we show $|E^T|^2$ for the scattered field of Figure 5-6 in Figure 5-7 and the phase or arg E^T in Figure 5-8. In Figures 5-7 and 5-8 the dashed lines show the values for an infinitely broad sheet. Near the upper slab, the moment method results differ very much from those for the flat sheet. Away from the upper slab and behind the slab illuminated at normal incidence, the moment method results oscillate about the flat sheet results. The oscillations imply the existence of a field distinct from that for a flat sheet. In such a description, we would exclude the guided wave as a constituent combining with the wave propagated through the lower slab because the exponential decay is strong. Instead, we might expect scattering from the tip or the far ends of the wedge. Of course the guided waves may be scattered by the edges or ends of the dielectric structure.

We obtain a comprehensive view of the field near the slab, from the displays of E^S by a computer-driven, oscilloscope plotter. Photographs of $|E^S|^2$ and the phase of E^S are shown in Figures 3-29 and 3-30. These figures show the highly excited guided waves for grazing or nearly grazing incidence, and the relatively large values of δs for such incidence. The figures show the smaller value of δs for $\phi i = 45°$. The less visible fringes apparently occur because of interference between waves from the vertex and slab ends with the plane wave through the slabs. The wave processes producing the weaker fringes may be significant for boresight error with an aperture antenna because many of these antennas measure fields through two balanced halves of the antenna. Small asymmetries can unbalance the antenna.

5.1.8 HOLLOW WEDGE: BORESIGHT ERROR

Although few radomes have the shape of a wedge, it is useful to estimate the boresight error of this idealized shape. The method is to determine the tilt of the wavefront, as described in Appendix A. To compute tilt, we fit a least squares line to phase delay data like that in Figure 5-8. In particular, we choose a line parallel to the incident wavefront for $\phi_i = 0$, 22.5°, 45°, and 67.5°; this line intersects the symmetry axis at x = 4 in. The line represents the position of an antenna aperture. For each angle we sample the phase at a set of points spaced by $\lambda_o/2$ and fit a least squares line to these

phase values. To estimate effects of aperture size we use nine points to represent a four λ_o wide aperture and seven points to represent a three λ_o wide aperture. Typical results for $\phi_i = 22.5°$ are tilt of $9.2°/\lambda_o$ or 1.5° boresight error, for the $4\lambda_o$ aperture.

Boresight error is summarized in Figure 5-9. The graphs have the shape of typical boresight error curves with a maximum at angles such that the projection of the aperture begins to clear the tip of the radome. The boresight error is larger for the larger aperture. This result is reasonable when we recall the abrupt change in phase near the wall; see Figure 5-8. A smaller aperture misses much of the phase delay increase. Figure 5-9 also shows boresight error when the phase is computed by flat sheet theory. In Figure 5-8, these values are the straight, horizontal line with zero tilt so boresight error is zero for $\phi_i = 45°$.

The boresight error magnitudes for the phase delays computed by the moment method are larger than those based on flat sheet theory. The error is more convergent for the moment method, where convergent means that the normal to the tilted phase line shifts toward the radome tip, away from the antenna normal. This sense of shift is reasonable because the guided wave is slow, increasing the phase delay near the wall. This effect is observed in axially-symmetric radomes, as we show in the next section.

5.1.9 AXIALLY-SYMMETRIC, THIN SHELL

The moment method results computed for the wedge resemble those observed in axially symmetric shells. For example, Figure 5-10 shows power transmittance $|T|^2$ measured in the region bounded by an axially-symmetric shell with thickness $0.029\lambda_o$, dielectric constant 3.2, length $12.8\lambda_o$, and base diameter $6.7\lambda_o$. Gimbal angle was 10°. $|T|^2$ is shown for both horizontal and vertical polarization, and for the probe scanned over paths at three distances from the tip. The data for vertical polarization show $|T|^2$ exceeding 0 dB for y less than zero; this is the side nearer the radome wall as sketched in Figure 5-11. The transmittance greater than 0 dB near the wall suggests guided waves.

Boresight error of the axially-symmetric shell was measured with an aperture antenna, diameter $4.46\lambda_o$; see Figure 5-12. The error was computed with a surface integration method in which the integration extends over the first Fresnel zone of the incident wavefront at the radome tip. This method has given accurate results for half-wave radomes, but for the thin wall radome discrepancies are large. The measured curves are more convergent than the calculated, where convergent means that the radome tilts the tracking null toward the radome axis, away from the boresight axis without radome. In terms of wavefronts, convergent implies greater phase delay along the lower wall for the situation of Figure 5-11. This result agrees qualitatively with the effect expected of a guided wave, which is a slow wave. This increased phase delay is evident for a wedge as in Figure 5-8 for $Y_A > 0$.

Figure 5-12 shows phase measured in the thin axially symmetric shell. It also shows data computed with the surface integration method. The data are given on two lines. One the horizontal diameter; the other 0.5 in. above. The discrepancies are large for either polarization although the same surface integration method has given accurate results when applied to a half-wave radome of the same size and shape. For horizontal polarization, the tilts of the measured and computed equiphase surfaces differ appreciably in Figure 5-13.* The large difference in tilts seems to explain the large discrepancies for the E-plane boresight error in Figure 5-12. The measured phase delays are generally larger than the computer-especially near the wall. This behavior suggests guided waves.

5.1.10 HALF WAVE, AXIALLY SYMMETRIC RADOME

The intensity variations in Figure 3-25 resemble variations that were observed in an axially symmetric radome. This radome was a half-wave thick, highly streamlined, and small, with base diameter $5.2\lambda_o$ and length $10.3\lambda_o$.

The measured intensity in the radome-bounded region is shown in Figure 5-14 for axial incidence. The measurements were made with an open-end waveguide probe in an interferometer setup which had a vertical propagation path. The radome was supported by three thin, wooden dowels in order to reduce scattering by supports.

The intensity variations for the smaller values of x have period between $0.6\lambda_o$ and $0.8\lambda_o$. This value compares reasonably with $(\delta x)_e = 0.6\lambda_o$ for $\phi = 130°$.

The intensity near the tip exceeds the incident value and varies with a period approximately a wavelength. It seems plausible that the high intensity results because guided waves are excited. The guided wave interpretation is supported by the spacings of minima near the tip. The spacing for an assumed, slab-guided wave is

$$(\delta x)_g = 2\pi/[k_g (\cos\theta)^{-1} - k_o] \qquad (35)$$

where θ is the angle between the slab and the free space wave direction. We obtain $(\delta x)_g = 1.1$ in. which compares well with the 1.2 in. ±0.1 in. spacings in Figure 5-13.

5.1.11 HEMICYLINDER

Figure 3-35 shows that the moment method values for $|E^T|^2$ vary about the results by approximating the radome as locally flat.

---

*These graphs have been reversed from those in Figure 5-10 because the gimbal angle for measurement is the negative of that for computation.

By comparing Figures 3-35 and 3-40, we see that the addition of anisotripic gratings increases power transmittance by 0.6 dB on the average over the diameter.

The large variations near the wall suggest guided waves.

5.2 PARALLEL POLARIZATION

The moment method results agree well with measured data, but the measurements with the dipole probe are averaged values (over the probe length). The accuracy of fields measurements seems rather low, but the measured data verify the moment method calculations. The lack of accuracy is in the position of the measurement when the probe is near the wall. The computed field decreases rapidly with distance from the wall; the probe averages this evanescent field. The computed field is defined mathematically at a point.

Figure 4-7 shows deep minima exist near a slab for parallel polarization, just as they do for perpendicular. However, the two polarizations require distinct thickness for equal fringe spacings.

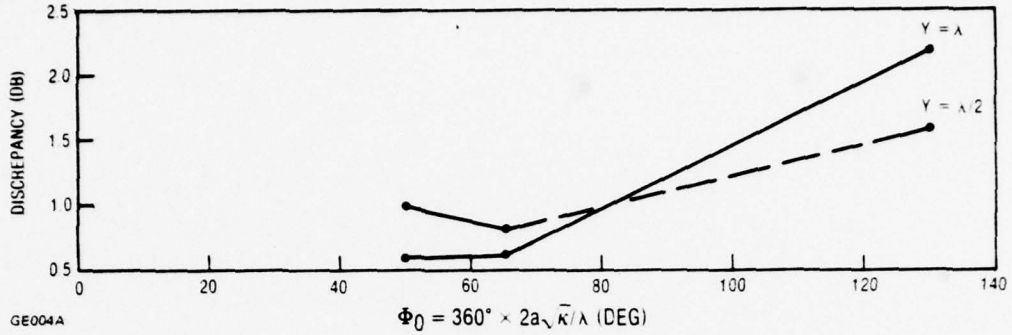

Figure 5-1. Maximum discrepancies for 4 in. wide slab from data in Figures 3-6, 3-7 and 3-8

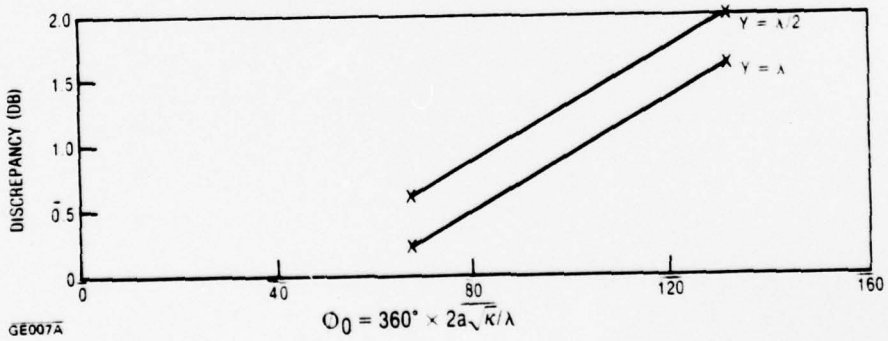

Figure 5-2. Maximum discrepancies for 10 in. wide slab from data in Figures 3-10 and 3-11.

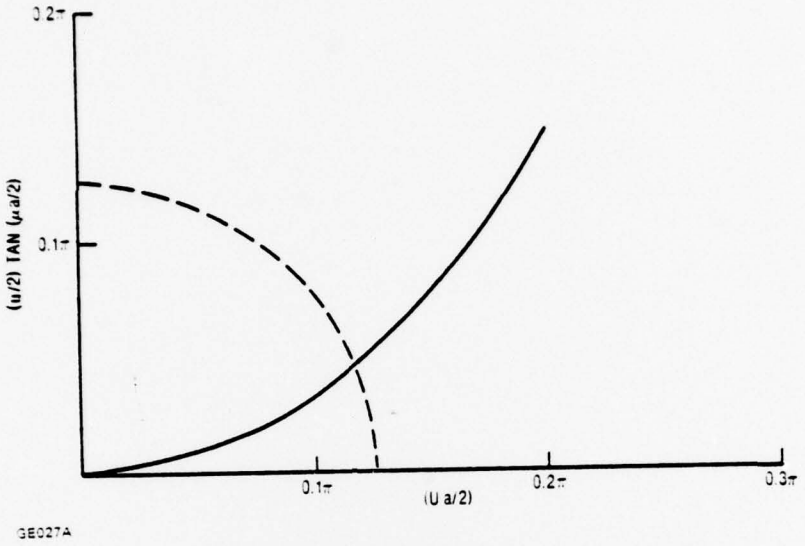

Figure 5-3. Solution of Equations 14 and 16 for 2a = 0.125 in., λ_o = 1.259 in., and k = 2.6

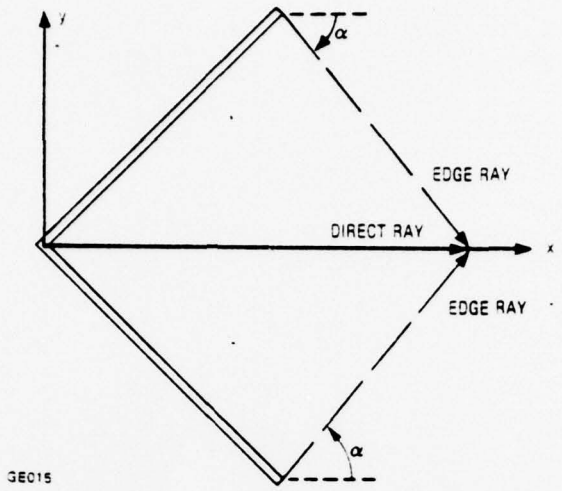

Figure 5-4. Hollow wedge; direct rays and edge diffracted rays shown for a point on symmetry plane

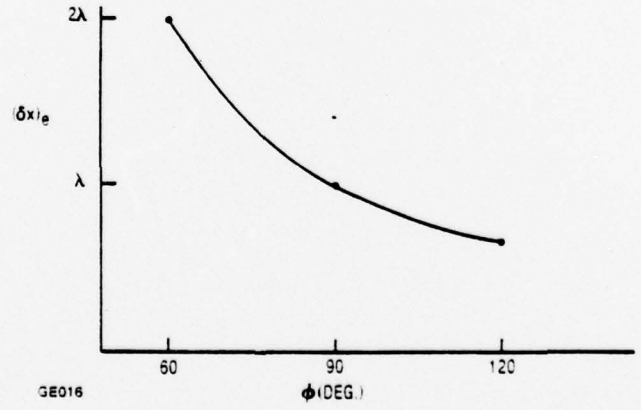

Figure 5-5. Spacings from Equation 34

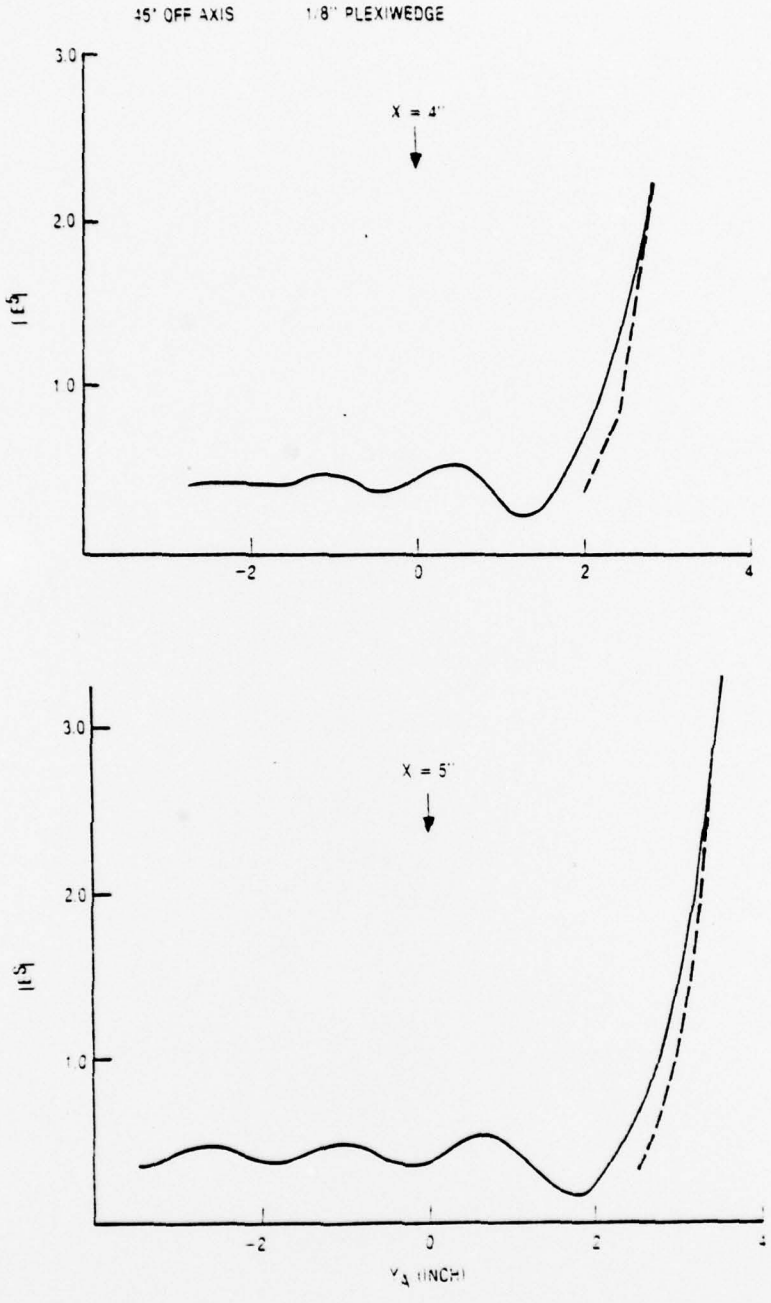

Figure 5-6. Computed values of scattered field magnitude for 90° hollow wedge thickness 0.125 in., λ_o = 1.259 in., N = 161, ϕ_i = 45°. The co-ordinate Y_A is on a line 45° to the Y axis; it is parallel to the incident wavefront for the upper graph Y_A = 0 occurs at x = 4 in.; for the lower x = 5 in. From moment method: (-); with exp(-vd): (--).

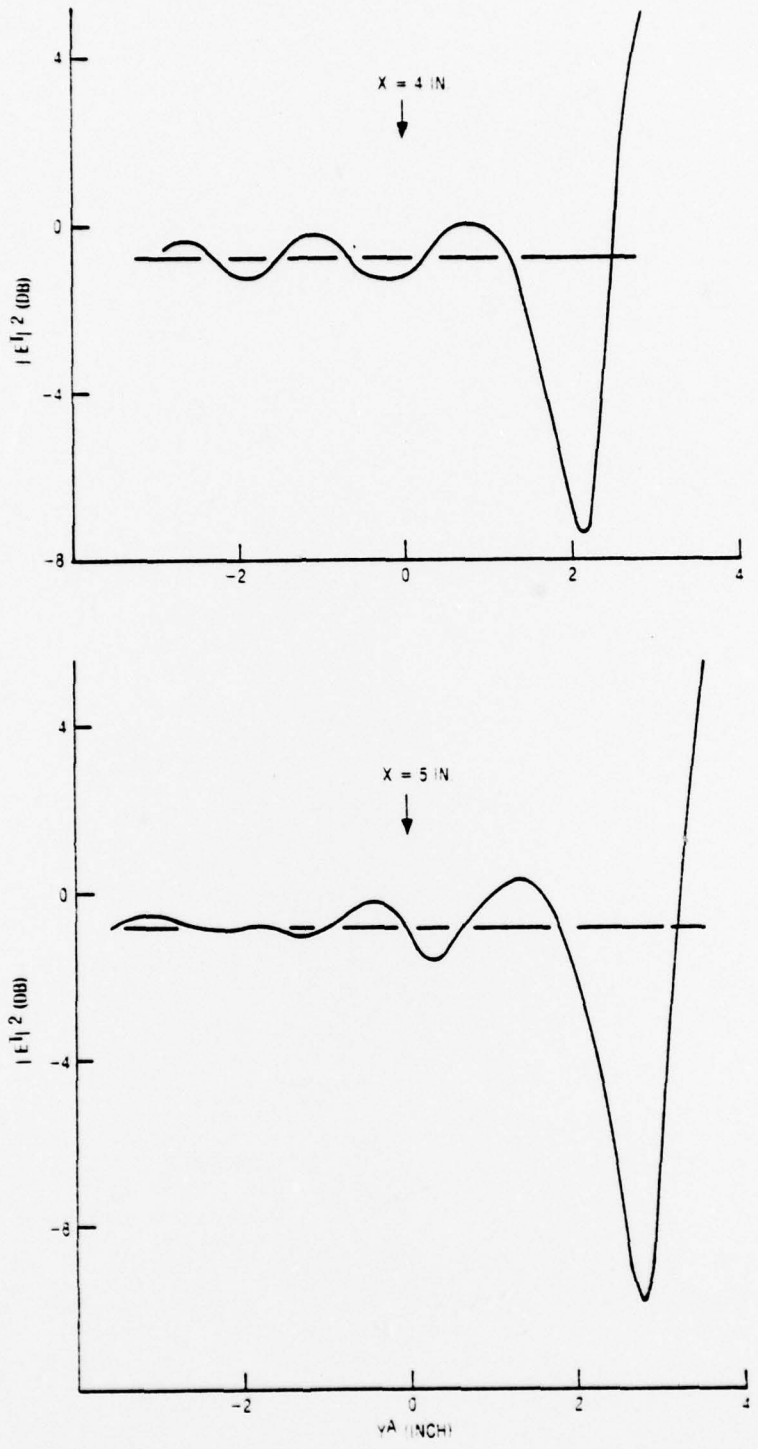

Figure 5-7. Intensity of total field for conditions of Figure 5-6. The dashed lines show the value for a flat sheet of infinite breadth.

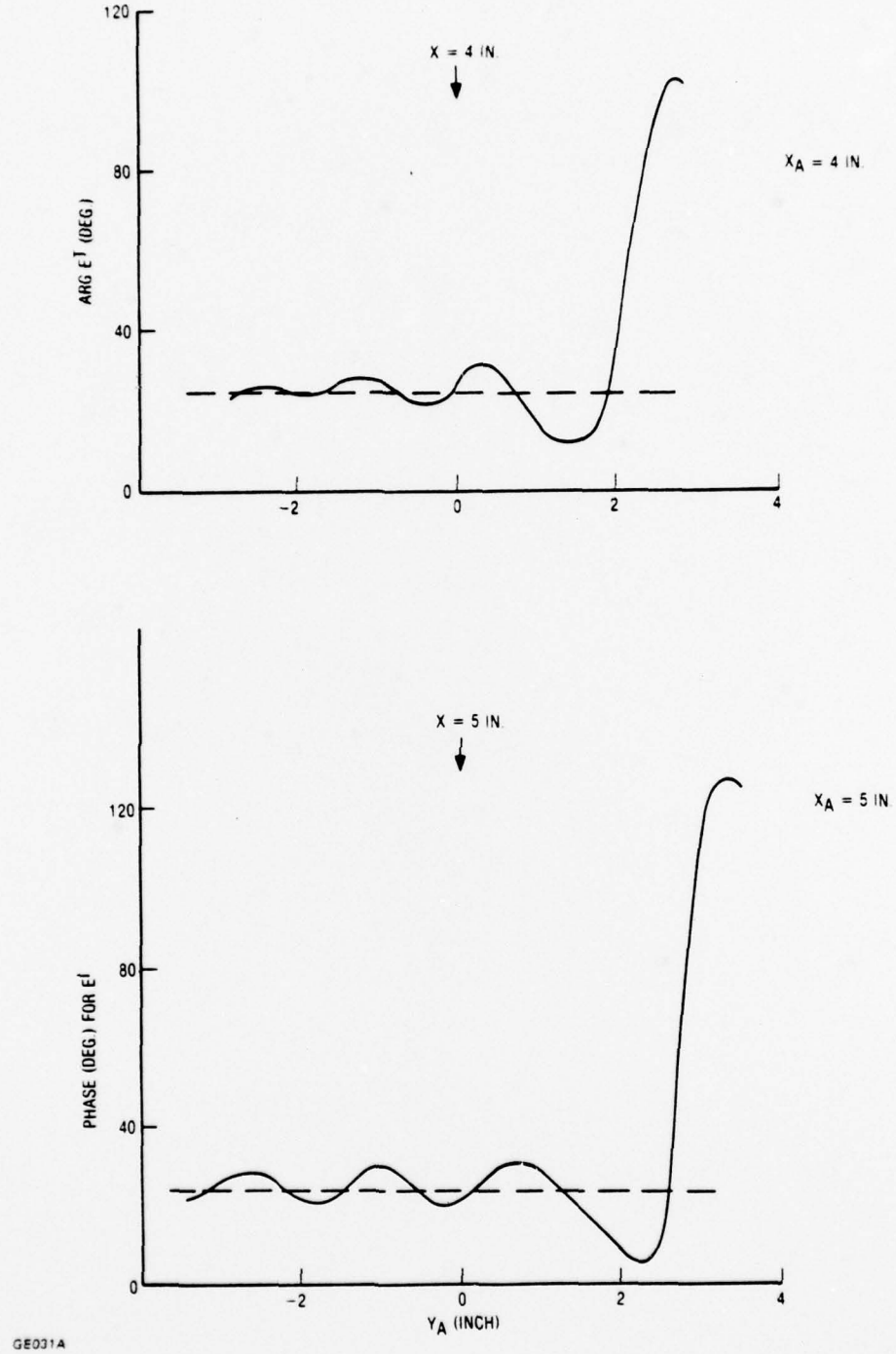

Figure 5-8. Phase for Figure 5-7

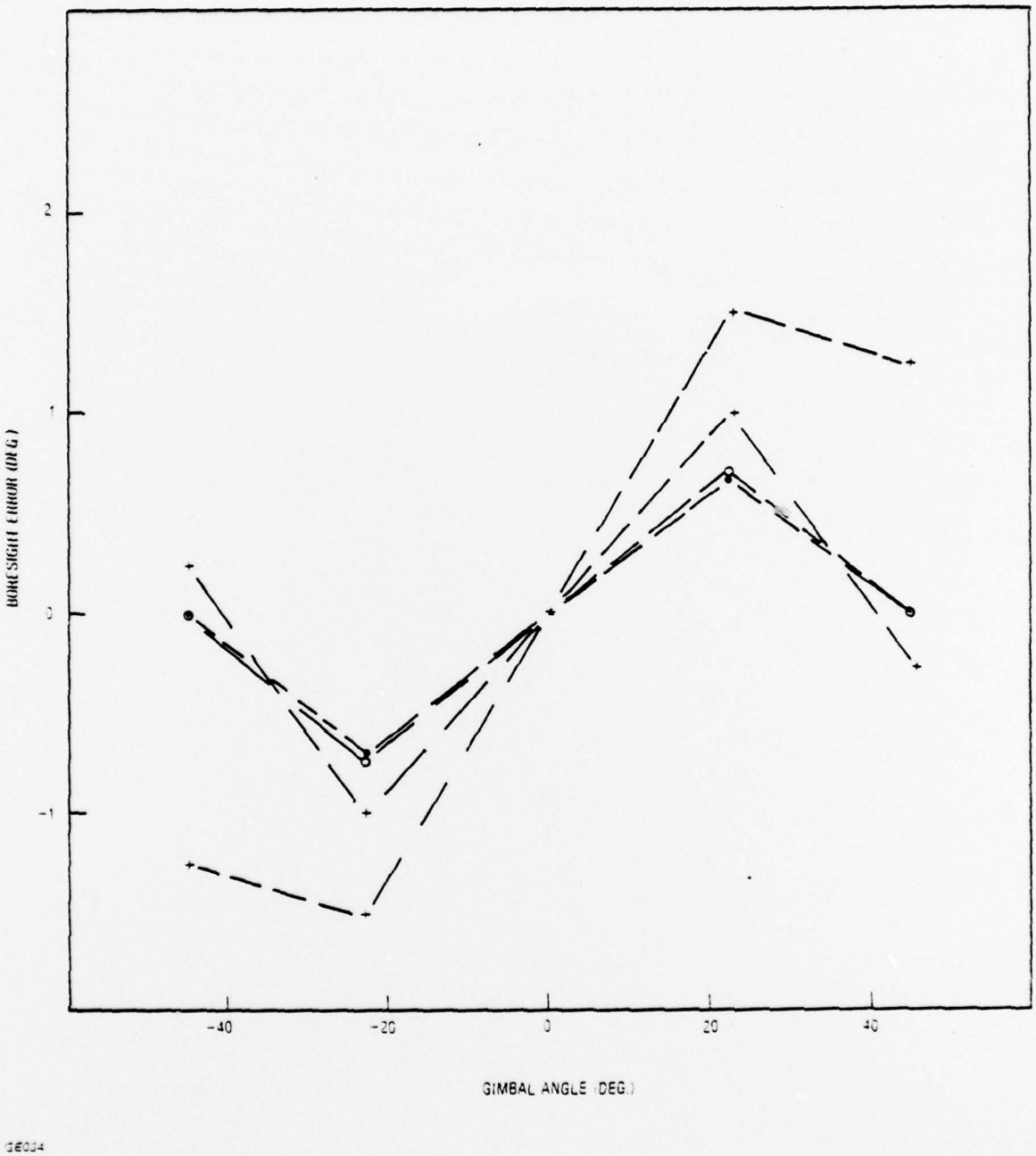

Figure 5-9. Calculated wavefront tilt for 1/8 in. thick wedge. From moment method. 4λ aperture, (+) 3λ aperture (x); from flat sheet phase delay: 4λ aperture (0); 3λ aperture (·).

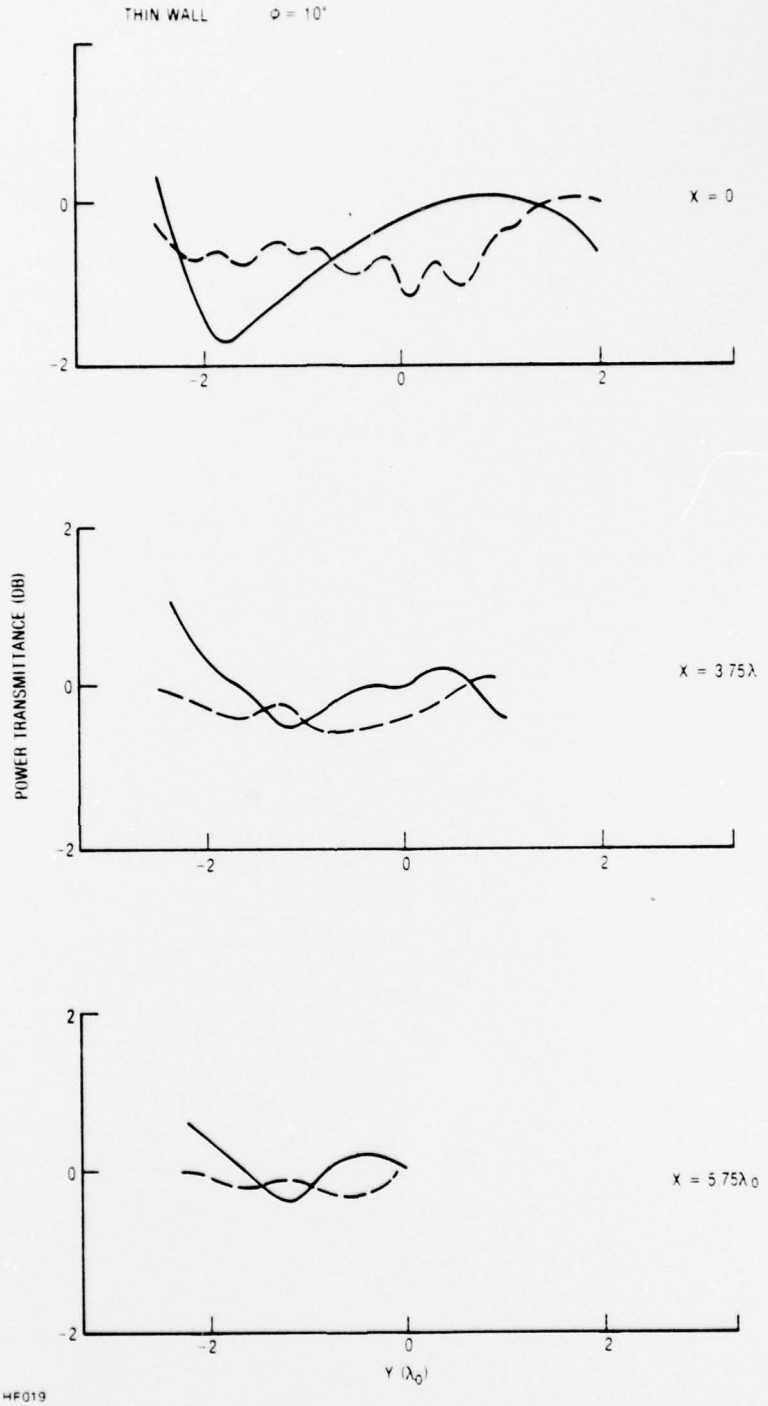

Figure 5-10. Power transmittance of thin-wall, quartz/polyimide, axially symmetric shell for 10° gimbal angle, open-end waveguide probe, in aperture plane. Vertical polarization (—); horizontal (--).

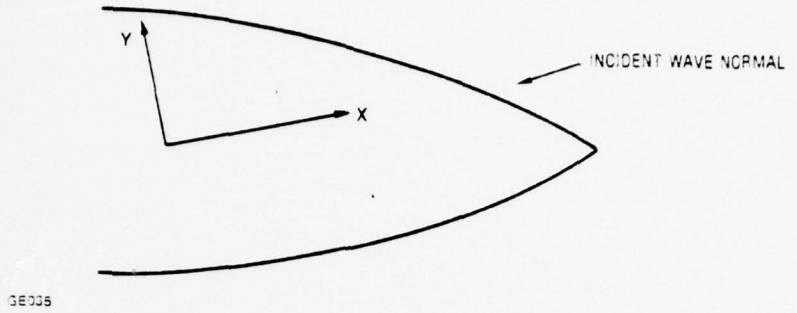

Figure 5-11. Co-ordinate system for probing inside axially symmetric shell

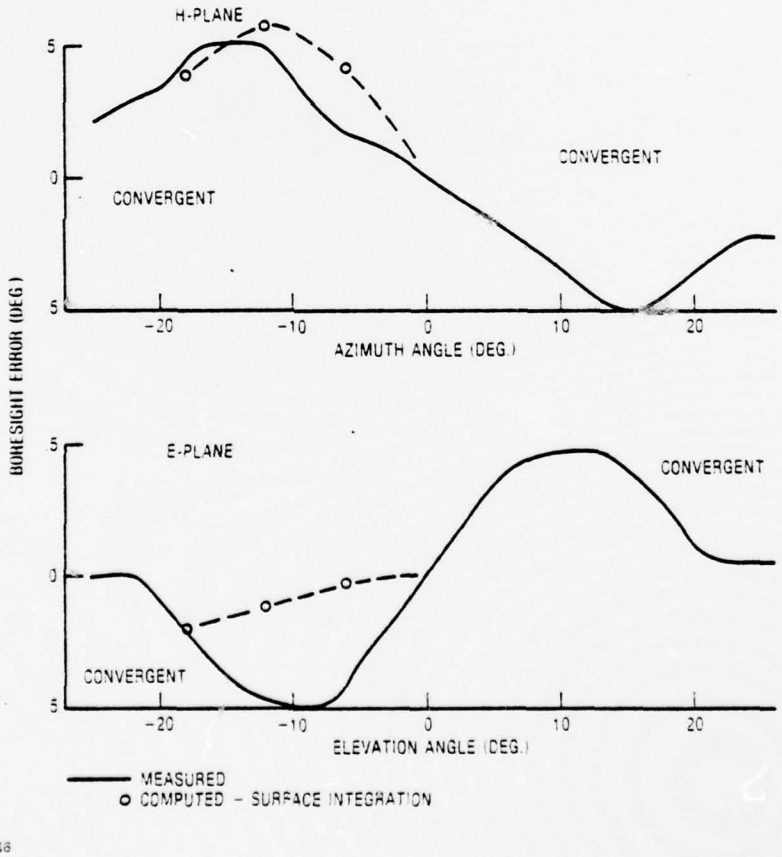

Figure 5-12. Measured and computed boresight error

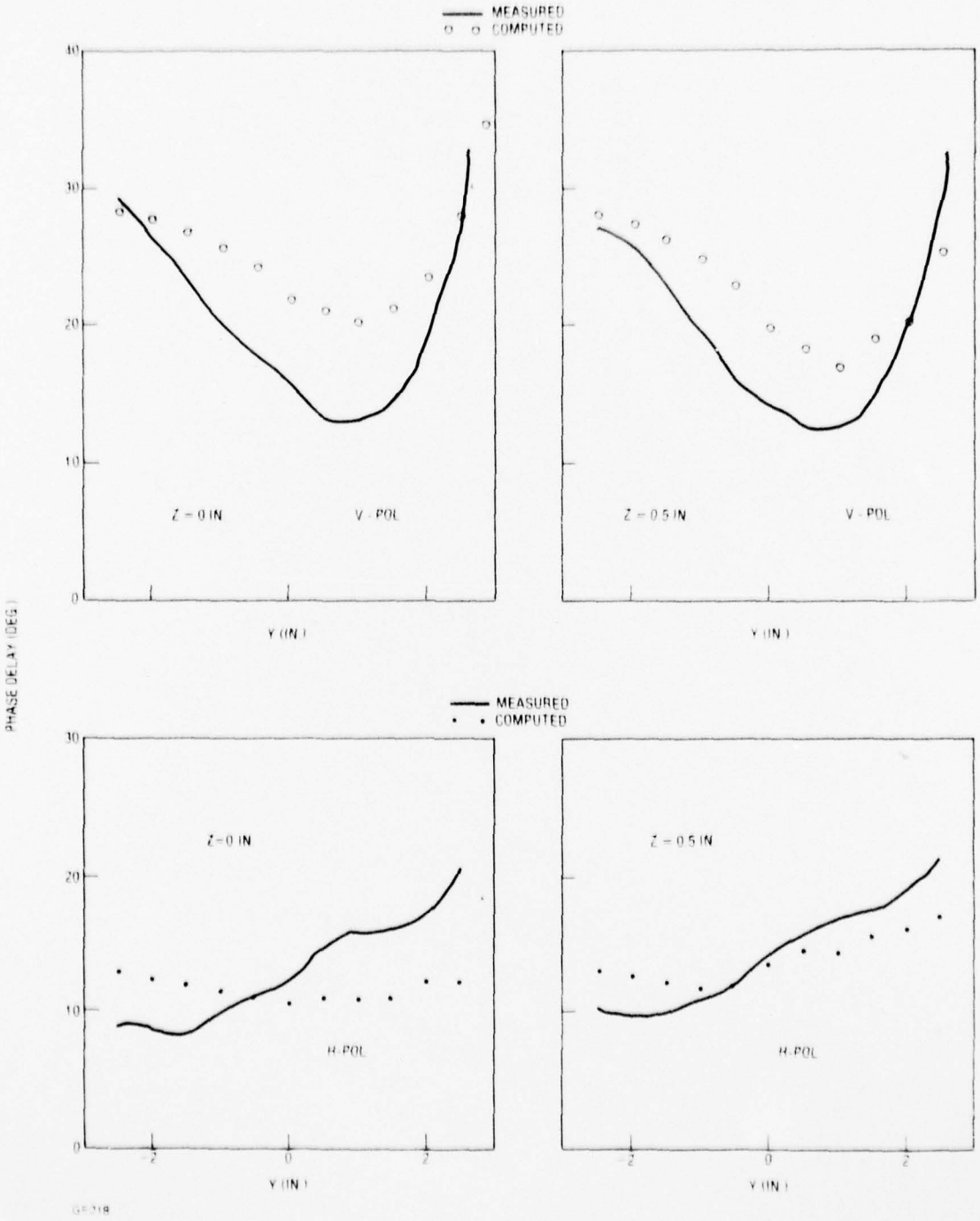

Figure 5-13. Phase delay in streamlined radome; thickness 0.029λ; $\kappa = 3.4$; 10° angle between incident wave normal and radome axis, both in horizontal plane.

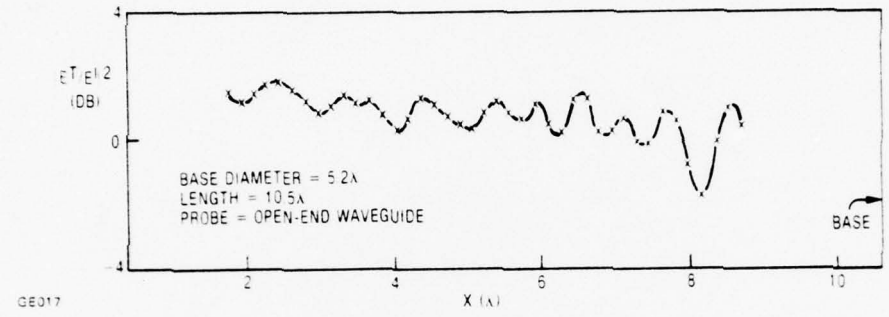

Figure 5-14. Power transmittance of ogival radome; inner surface of tip at x = 0. Dielectric constant 5.5, thickness 0.222λ; with 0.026λ thick coating of dielectric constant 3.0

6. REFERENCES

1. R. A. Hayward, E. L. Rope, G. Tricoles, "Radome Boresight Error and its Relation to Wavefront Distortion," Proceedings of 13th Symposium on Electromagnetic Windows, 1976, Georgia Institute of Technology.

2. G. Tricoles, "Radiation Patterns of a Microwave Antenna Enclosed by a Hollow Dielectric Wedge," Jour. Opt. Soc. Am., Vol. 53, pp. 545-557 (1963).

3. J. H. Richmond, "Scattering by Dielectric Cylinders of Arbitrary Cross Section Shape," IEEE Trans., Vol. AP-13, pp. 334-341 (1965).

4. J. H. Richmond, "TE Wave Scattering by a Dielectric Cylinder of Arbitrary Cross Section Shape," IEEE Trans., Vol. AP-14, pp. 460-464 (1966).

APPENDIX A

WAVEFRONT TILT AND BORESIGHT ERROR

This appendix shows that radome boresight error is related to the tilt of the wavefront in the radome-bounded region.

For reception, the received complex amplitude of a rectangular component is

$$E^R = \iint F\ T\ E^I\ dA \quad , \tag{A-1}$$

where F is the aperture distribution, E^I is the amplitude of an incident plane wave amplitude, T is the complex-valued transmittance. The integration extends over the region such that F has appreciable magnitude, and T depends on the angle of arrival of the incident plane wave as well as position inside the radome.

To simplify the notation let us consider a symmetric situation. Assume an axially-symmetric radome with its axis horizontal and the antenna normal rotated in the horizontal plane as in Figure A-1. Establish a rectangular co-ordinate system, co-ordinates x, y, z, attached to the antenna, and let the antenna be in the x = 0 plane. Let the incident wave normal be in the x-y plane. To maintain symmetry about z = 0, consider the field polarized horizontally or vertically. The incident wave is exp $ik_y y$ where k_y is $(2\pi/\lambda_o)\ \sin(\delta\beta)$, with $\delta\beta$ the off axis angle of the wave. Let the aperture distribution be uniform in its finite domain. Let T be exp $i\Delta\Phi$, where $\Delta\Phi$ is phase delay so the amplitude variation is ignored. Introduce a phase taper through exp $i\alpha y$ to describe conical scanning. From Equation A-1 we have

$$E^R = \iint \exp i\,[\Delta\Phi + (k_y + \alpha)\ y]\ dA \quad . \tag{A-2}$$

Now approximate $\Delta\Phi$ with a polynomial so $\Delta\Phi$ is $p(y, z) + r(y, z)$ with p the polynomial and r a remainder. If we collect k_y into the linear term of the polynomial we have

$$\Phi = \Delta\Phi + k_y y$$

$$= a + (b' + k_y)\ y + cy^2 + dy^3 + ez^2 y + fz^2 \tag{A-3}$$

if we expand to the third degree. Note that odd powers of z are absent because of the assumed vertical symmetry. By combining Equations A-2 and A-3 we have

$$E^R = \iint \exp i(\Phi + \alpha y + r)\ dA \quad . \tag{A-4}$$

For conical scanning systems the boresight condition is

$$|E^R(\alpha)|^2 = |E^R(-\alpha)|^2 \quad . \tag{A-5}$$

Thus adjustment of k_y gives equal power in two lobes. A different condition holds for monopulse type antennas. This adjustment reduces phase variation so we can expand the exponential in Φ. Similarly α is usually small so its exponential can be expanded. The remainder term also can be expanded if it is small. After some algebra we obtain from the condition

$$\delta|E|^2 = |E^R(\alpha)|^2 - |E^R(-\alpha)|^2 = 0 \tag{A-6}$$

that k_y at boresight is

$$k_{yo} = -b' - \frac{1}{6}(e + 3d)\,R^2 \quad . \tag{A-7}$$

Boresight error is the angle $\delta\beta$ such that k_{yo} is $(2\pi/\lambda_o)\sin(\delta\beta)_o$, or for small angles $(2\pi/\lambda_o)(\delta\beta)_o$. Thus boresight error

$$(\delta\beta)_o = -\left[b' + \frac{1}{6}(e + 3d)\,R^2\right]/(2\pi/\lambda_o) \quad . \tag{A-8}$$

From Equation A-8, for small higher order terms, in e and d, boresight error is approximately

$$(\delta\beta)_o = -b'/(2\pi/\lambda_o) \quad . \tag{A-9}$$

Thus boresight error is approximately proportional to the linear phase tilt, where tilt means the magnitude of the expansion coefficient b' in the polynomial fitted to $\Delta\Phi$. In practice we fit a least square surface to $\Delta\Phi$. Note that, although many approximations were made, none restrict $\Delta\Phi$ from realistic values.

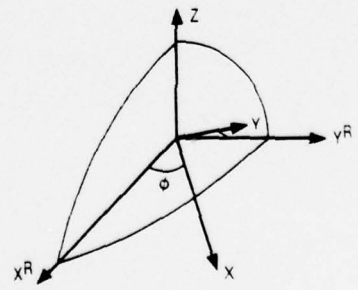

GE037

Figure A-1. Co-ordinate system